**Materials Science And Technology**
**Department-University Of Crete**

**Institute Of Electronic Structure And**
**Laser-Foundation For Research And Technology**



# Master Thesis

---

*Ultrashort Laser Wave Packet Sculpting For Optimized Materials Engineering*

---

**By**

**Apostolos Kyriakakis**

**Supervisor: Prof. Stelios Tzortzakis**


**Heraklion, June 2023**

*Master Thesis: Ultrashort Laser Wave Packet Sculpting For Optimized Materials Engineering*

**AUTHOR**


***Apostolos Kyriakakis, MSc Candidate***

Study Program: MSc Materials Science And Technology.

Department: Materials Science And Technology Department.

University: University of Crete.

Track: Materials Science & Optical Lithography/Laser Printing.


**EXAMINATION COMMITTEE**

***Prof. Stelios Tzortzakis***

Department-University: Materials Science And Technology Department, University of Crete.

Research: Head Of Ultrashort Nonlinear Laser Interactions and Sources Research Group (UNIS Group), IESL-FORTH, Greece.

***Dr. Maria Farsari***

Institute: IESL-FORTH, Greece.

Research Track: Research Director-Head Of Nonlinear Lithography Group.

***Prof. Maria Kafesaki***

Department-University: Materials Science And Technology Department, University of Crete.

Research Track: Associated Researcher Of Photonic-, Phononic- And Meta-Materials (PPM) Group, IESL-FORTH, Greece.

# Table Of Contents

# *Acknowledgments*

Towards the completion of this master thesis, I would like to express my gratitude to so many people without whom I could not undertake this journey. So, I consider it as both a pleasure and a duty to acknowledge their participation in this research.

First and foremost, I am deeply grateful to prof. Stelios Tzortzakis for giving me the opportunity to be part of his UNIS research group (Ultrashort Nonlinear laser Interactions and Sources Research Group), even since my undergraduate studies, and carefully monitoring my progress during my MSc program. His valuable guidance, insightful comments and encouragement helped me to enrich my knowledge but, also, inspired me to continue pursuing my goals.

Next, I would like to extend my gratitude to Dr. Maria Manousidaki. This thesis would not have been possible without her endless patience, knowledge-sharing, and willingness to help me face any difficulty that came across my path. She offered me a great amount of assistance at every stage of this research project and her opinion was really influential in conducting a well-rounded research project.

Moreover, I would like to offer my special thanks to Dr. Maria Farsari and prof. Maria Kafesaki not only for accepting to be part of this thesis committee but, also, for evaluating the scientific background of this research project.

Additionally, special thanks should, also, go to Dr. Argyro Klini for her guidance and practical help in crucial parts of this thesis, Dr. George Kenanakis for conducting a major part of the catalysis measurements required in this thesis, and Ms. Aleka Manousaki for the SEM images.

Furthermore, I wish to thank all the additional members of the UNIS group, Mr. Michalis Loulakis, Dr. Anastasios Koulouklidis, Ms. Christina Daskalaki, Dr. Ioannis Liontos, Mr. Panagiotis Konstantakis, Mr. Constantinos Kerantzopoulos and Ms. Angeliki Sifaki, for all the help and fun moments that we shared. I would, also, be remiss in not thanking Mr. Konstantinos Misdanitis, since a significant part of this project was supported by the experimental data obtained in his BSc thesis, Dr. Anna Tasolamprou for the theoretical design of the meta-atoms and Ms. Frantzeska Gkointa for the contact angle measurements.

Last but equally important, I want to thank my family and friends for their support, encouragement and being by my side in times of challenge. Their contribution was priceless and I will, forever, be grateful to them.

# *Abstract*

Direct Laser Writing (DLW) is a well-established additive manufacturing technique that offers great resolution and precision. In the quest though of high throughput processing, DLW falls short due to the time-consuming point-by-point writing.

To address this issue, a Holographic Multi-Foci 3D Printing technique is studied in this thesis. The time-optimized laser beam shaping is then used in two applications. The first application is the fabrication of 3D periodic structures with high micro-featured porosity, coated with ZnO Nanorods (NRs). Our time-efficient printing method enables the accelerated fabrication of complex structures through parallel processing and offers the ability to scale up the structure dimensions for practical applications, such as photocatalytic degradation of toxic substances. In the frame of this MSc thesis, we also investigated the relation between the reaction rate and the porosity of the structures by studying the photodegradation rate of organic pollutants over time, under UV light irradiation, in samples with different porosity. In the second application we explored the detection of harmful substances, such as pesticides, in extremely small concentrations (ppb). We developed 2D meta-surfaces through the parallel processing (Multi-Foci Parallel Ablation) on thin layers of gold. These materials have E/M response in the THz frequency region, which is ideal for the detection of pollutants and other chemical residues.

# *Part I*

# *Theoretical Background Knowledge*

# 1. Direct Laser Writing Via Multi-Photon Polymerization

## 1.1 Direct Laser Writing (DLW)

Direct Laser Writing (DLW) is an attractive printing technique based on ultra-localized Multi-Photon Photopolymerization (MPP). It allows the construction of three-dimensional (3D) structures (*fig. 1.1.1*) with sub-100 nm resolution for a wide variety of applications, such as micro-optics, photonics, chiral, micro-fluidics, biomedicine, etc [1],[2].

In general, photopolymerization through DLW can be achieved by non-linear photon absorption only within the focal volume pixel (Voxel) of a transparent photosensitive material. For this purpose, an ultra-fast laser (fs laser) is tightly focused inside the volume of the photosensitive material inducing both the absorption of two or more photons and the local polymerization of the material. Then, by selective point-by-point exposure of the material to the laser radiation, assisted by a computer designed 3D model pathway, one has the ability to create arbitrary 3D structures of high spatial resolution.

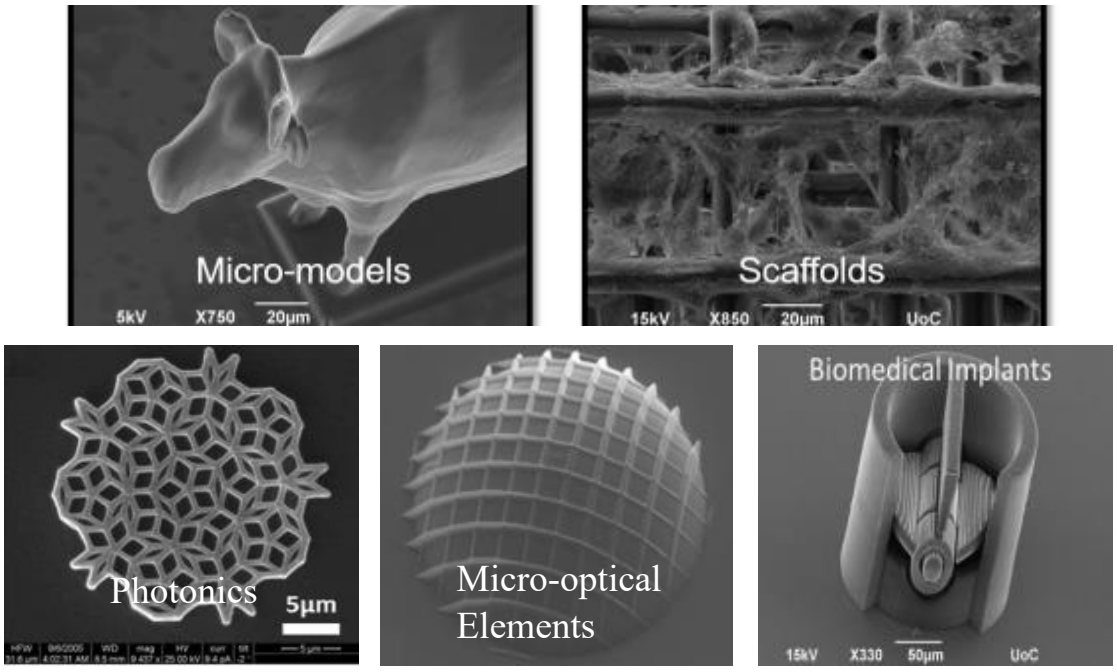


***Figure 1.1.1:*** 3D Structures Fabricated By MPP-DLW Technique [3], [4]

In order to write the 3D structure into the photopolymer using the focused laser beam, one needs to move either the beam focus or the sample, i.e., change the position of the focal volume pixel (Voxel) in three dimensions. The former can be done with galvanometric scanners, while the latter with high-resolution XYZ stages.

Galvo scanners exhibit an additional feature in comparison with the XYZ stages. They can create the desired structure in a layer-by-layer photopolymerization format by 'slicing' the 3D computer designed file. Each slice is exported as a single file, projected at the photosensitive

material and after the writing of the first slice is completed, the sample moves on the Z-axis using a high-resolution translation system in order to write the next slice. This process continues until all the files are written. Except from the Z-axis movement stage, XY-axes movement stages are also required, to allow large-scale movements. On the other hand, a XYZ stages movement writing system does not require the slicing of the designed 3D model since the stages can move in all directions and selectively polymerize each point of the material until the 3D model is completed.

Usually, the photosensitive material is placed on top of a cover glass that can be moved in all three dimensions (X, Y, Z) through a high precision positioning stages system. When the fabrication of the polymer structure ends, the glass with the photosensitive material is rinsed in an appropriate solvent that removes the non-polymerized material and leaves intact the 3D polymeric structure (*fig. 1.1.2*) [2],[5].

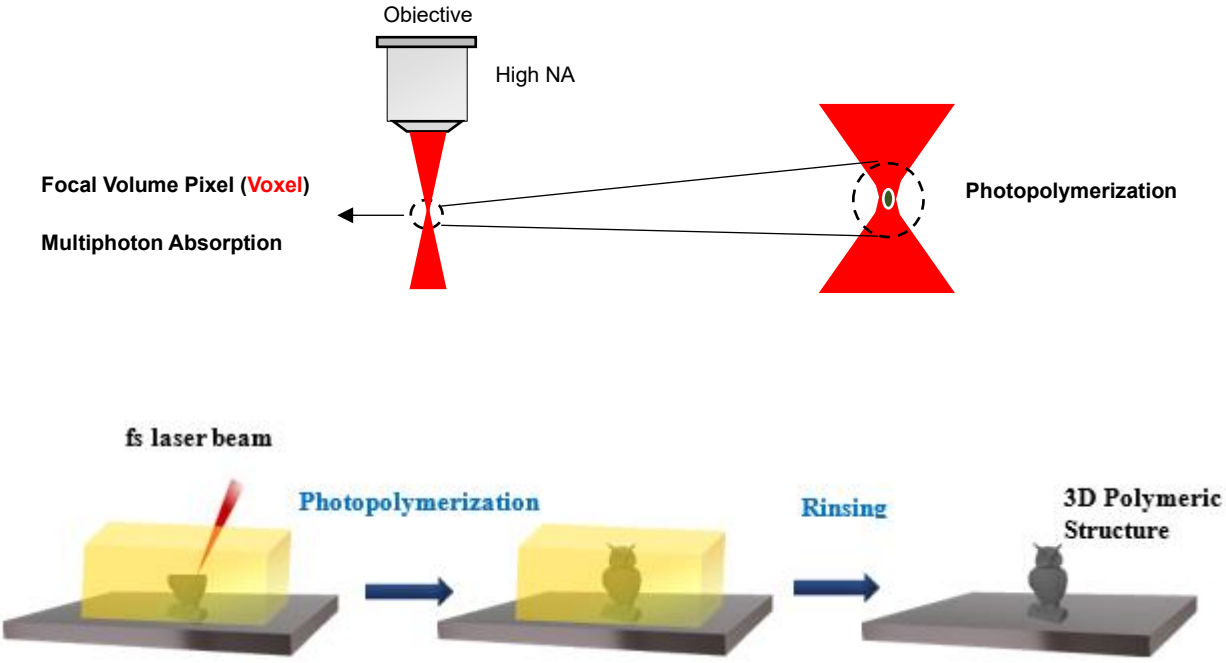


***Figure 1.1.2:*** Typical Direct Laser Writing Procedure

## 1.2 Photoexcitation

Photoexcitation is a process that takes place by the absorption of photons inside the volume of the polymerizable material. The electrons inside the material are firstly transferred into the conduction band and then can be promoted to excited states. A necessary condition for this to happen is the electrons to gain enough energy. If the material has large band gap, visible spectrum photons are not enough to immediately ionize the electrons. However, this is possible through the two-photon absorption (2PA) or multi-photon absorption (MPA) and leads the chemical bonds to break and form free radicals or charged atoms, cations (+) or anions (-). More precisely, during ionization non-linear processes (*fig.1.2.1*) occur such as multi-photon ionization (MPI), avalanche ionization (AI) and tunnel ionization (TI).

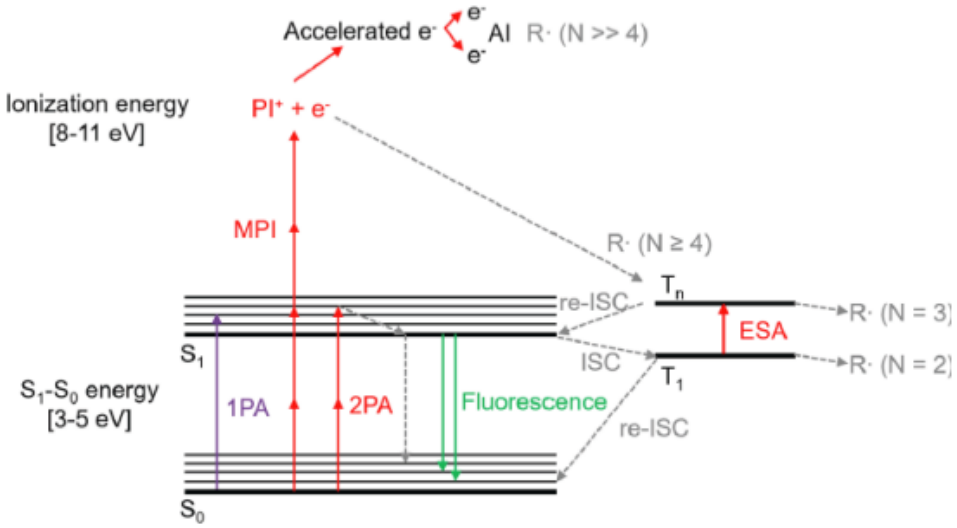


***Figure 1.2.1:*** Typical Photoexcitation Diagram Simulated For Polydimethylsiloxane (PDMS) [6]

In multi-photon ionization more than one photon is absorbed and the electron is excited from the ground state $S_0$ into the conduction band. In this case, the laser produces a strong field with high frequency and the number of photons must be enough so that the given energy is larger than the band gap. If the simultaneous photons absorption is more than the one needed for the above transition, the electron can be excited to higher energy levels and even gain enough energy to be ionized out of the valence shell (ionization energy). This non-linear process is called multi-photon ionization (MPI) and can occur simultaneously with possible MPA and 1PA, competing each other. Avalanche ionization involves free-carrier absorption followed by impact ionization. When an electron, that already exist in the conduction band of the material, absorbs sequentially several photons will move to higher energy levels in the conduction band. This transition needs to be accompanied by both energy and momentum conservation. In order to achieve that, the electron must transfer momentum by absorbing or emitting a phonon or by scattering off an impurity. After the sequential absorption of n photons, where n is the smallest number that satisfies the relation

$$n\hbar v \geq Eg$$

$\hbar$ is Planck's constant divided by $2\pi$ and v the light frequency, the energy of the electron is larger than the band gap energy. Thus, the electron can ionize another one, near the valence band, through collision resulting in the production of two new electrons. Each of these electrons will gain free-carrier energy and potentially ionize more and more electrons in the valence band, an avalanche-like process. For strong laser fields but low laser frequency TI prevails over MPI. In TI, the electric field of the laser suppresses the Coulomb well that binds a valence electron to its parent atom. If the electric field is very strong, the Coulomb well can be suppressed enough that the bound electron tunnels through the short barrier and becomes free. At this point, it is worth noting that in MPI and AI the excitation rate is dependent by laser intensity I but this relation does not apply in TI [6],[7].

## 1.3 Two-Photon Absorption

An important non-linear excitation method, which belongs to the category of multi-photon absorption, is the two-photon absorption (TPA). As mentioned in the beginning of part (1.2), TPA refers to the absorption of two photons into the polymerizable material that leads to the transition of an electron from a low to a higher energy level. There are two different mechanisms of two-photon absorption which are sequential TPA and simultaneous TPA (*fig.1.3.1*) [6],[8],[9].

When sequential TPA occurs, the absorbing species are excited to a real intermediate state. This intermediate state emerges by the absorption of a photon, and after its creation, a second photon with the same energy as the ground state is absorbed leading the population of the intermediate state to further excitation to a higher energy level. Considering that the intermediate energy state exists it is obvious that the material absorbs at this specific wavelength since the photon energy ħv includes the wavelength λ through the relation $v=2\pi/\lambda$. Sequential TPA may be considered as two sequential 1PA.

Simultaneous TPA is the TPA process where the electron absorbs two photons simultaneously in one excitation event to transcend the energy gap. This phenomenon has no real intermediate state but a virtual one as a result of the interaction of the absorbing species with the first photon. The second photon can be absorbed only if arrives before the decay of the virtual state, meaning within the virtual state lifetime. In order for this to become possible, higher intensities are required, that are usually provided by a femtosecond (fs) laser, since Heisenberg's uncertainty principle predicts that the lifetime's order of magnitude is a few femtoseconds.


***Figure 1.3.1:*** Schematic Illustration Of a) One- and Two- Photon Absorption b) Sequential And Simultaneous TPA

The most common lasers for TPA method are Ti: Sapphire femtosecond pulse lasers because they produce very short pulses, approximately 100 fs or less. In addition, they are useful for TPA as their central wavelength is around 800 nm, i.e., close to half-wavelength of polymerization for many UV-photocurable resins but also twice the wavelength of polymerization of many photopolymers. This allows easy control of the polymerization threshold energy [9].

## 1.4 Photopolymerization Mechanism

The formation of polymer chains and the building of solid structures through photopolymerization can be realized by two main mechanisms, cross-linking and polymerization. The former is mainly focused on the creation of cross-links with chemical bonds while the other refers to the creation of polymers (or macro-molecules) from monomers (or molecules) via a chain reaction procedure. In general, the polymerization process is described as below

$$M \xrightarrow{+M} M_1 \xrightarrow{+M} M_2 \xrightarrow{+M} \dots \xrightarrow{+M} M_{n-1} \xrightarrow{+M} M_n$$

where M is the monomer or oligomer, $M_n$ the polymer chain and n the number of monomers. Realistically, photosensitive materials contain several types of elements but the most important one is the photoinitiator [10].

After photoexcitation, the chemical bonds of the photoinitiator break to form electrically unstable atoms, molecules, or ions, meaning free radicals or cations ($K^+$)/ anions ($A^-$). This activity is called photolysis or photodissociation and is expressed with the following equation [6]

$$PI \xrightarrow{\hbar v} PI^* \rightarrow R^*$$

where PI the photo-initiator, $PI^*$ the excited state of the photoinitiator and $R^*$ the free radical. Instead of free radicals, the photoexcitation event can, also, lead to the production of cations ($K^+$)/ anions ($A^-$). Based on that, polymerization is divided in radical and ionic polymerization.

PI concentration is one of the most important parameters because it has a great impact at the rate of photopolymerization due to the production of free radicals or cations. In reality, mainly in 1PA, the photopolymerization rate increases with the increase of PI concentration but only until it reaches a maximum optimum concentration where it starts to decrease. Moreover, 2PA in materials responds proportional to the squared optical density ($I^2$), so, at the focal point, where 2PA and the production of free radicals take place, it is possible to achieve high resolution using a tightly focused laser due to a nonlinear absorption cross section [6].

When the photolysis occurs, free radicals $R^*$ or $K^+$ /$A^-$ interact with monomers and form monomeric radicals ($RM^*$) or macro-cations ($KM^+X^-$) / macro-anions ($AM^-X^+$) initiating the polymerization reaction. This procedure is called initiation and accounts as the most important step in the whole polymerization reaction. It is expressed with the equation

$$R^* + M \rightarrow RM^*$$

Monomeric radicals and macrocations/ macroanions can further interact with monomers to create macromolecular chains through a process named propagation and is shown below

$$RM^* \xrightarrow{+M} RMM^* \rightarrow \dots \rightarrow RM_n^*$$

Polymerization terminates in different ways depending on whether it is radical or ionic. For radical polymerization, there are two mechanisms of termination, recombination, and

disproportionation. In recombination two active polymer chains merge together by joining their radicals whereas in disproportionation one proton is transferred from the hydrogen donor radical to the acceptor radical. Practically, the one radical cancels the other without the need of joining together. In some cases, a third way of termination can be observed, occlusion, where free radicals become "trapped" within a solidified polymer. If this happens, reaction sites remain available but cannot react with other monomers or polymers as a result of the limited mobility into the polymer network. Eventually, they tend to react with oxygen or other reactive species that diffuses into the occluded region. However, this may cause further problems like aging or changes in mechanical properties of cured parts. For ionic polymerization, termination occurs with ionic rearrangement or chain transfer mechanisms. The first mechanism refers to the transfer of a proton ($H^+$) to the counterion from the macrocation/macroanion. As for chain transfer, a monomer receives a proton with a counterion and forms a polymer with low molecular weight. In comparison with radical polymerization, cationic presents four basic features [10],[11]

• low curing speed

• lower viscosity

• small shrinkage after polymerization

• severe post-irradiation dark polymerization

Plus, sometimes it is required extra thermal process for high efficiency in monomers conversion. All of these characteristics must be considered when choosing the appropriate material. Overall, the photopolymerization steps for radical polymerization are depicted below

| | |
|---|---|
| **Photolysis** | $PI \xrightarrow{h\nu} PI^* \rightarrow R^*$ |
| **Initiation** | $R^* + M \rightarrow RM^*$ |
| **Propagation** | $RM^* \xrightarrow{+M} RMM^* \rightarrow \ldots \rightarrow RM_n^*$ |
| **Termination** | $RM_n^* + RM_m^* \rightarrow RM_{n+m}R$ (Recombination) |
| | $RM_n^* + RM_m^* \rightarrow RM_n + RM_m$ (Disproportionation) |

## 1.5 Writing Resolution-Diffraction Limit

Theory states that the focusing of a laser beam is limited within the Abbe's diffraction limit (DL). Thus, the highest resolution obtained by a focused laser beam is given by

$$DL = \frac{0.5\lambda}{NA}$$

where λ is the laser wavelength and N.A. is the Numerical Aperture of the focusing objective. This has fueled the race for ever decreasing wavelengths [8].

To exceed the diffraction limit and produce even smaller photopolymerized voxels in comparison with those defined by the diffraction limit, materials with a well-defined photopolymerization threshold need to be used. Typically, the production of radicals is achieved through the excitation of the photoinitiator by the laser beam and these radicals are quenched by oxygen and other quenchers in the system. Even though quenching is a competing effect to photopolymerization and is usually considered detrimental to the process, in 2PP can be used to circumvent the diffraction limit and produce structures of very high resolution. This is possible after the proper modification of the light intensity at the focal volume, so that the light-produced radicals exceed the quenchers and initiate polymerization only in a specified region where exposure energy is larger than the threshold. From this point on, the diffraction limit becomes just a measure of the focal spot size, and it cannot be used to determine the voxel size [10],[12].

Two-photon polymerization, as currently the only micro-processing approach that has intrinsic 3D fabrication capability, has been successfully employed for the production of a variety of photonic and micromechanical devices. Two-photon process prevails over single-photon absorption used in conventional rapid prototyping since it has at least two advantages

- Common polymers have negligible linear absorption in the red, near-infrared region, so the laser penetrates deeply into materials and directly induces polymerization from inside without contaminating outside of the focal volume.

- The quadratic dependence of polymerization rate on the light intensity enables 3D spatial resolution and accuracy is better than that achieved in single photon.

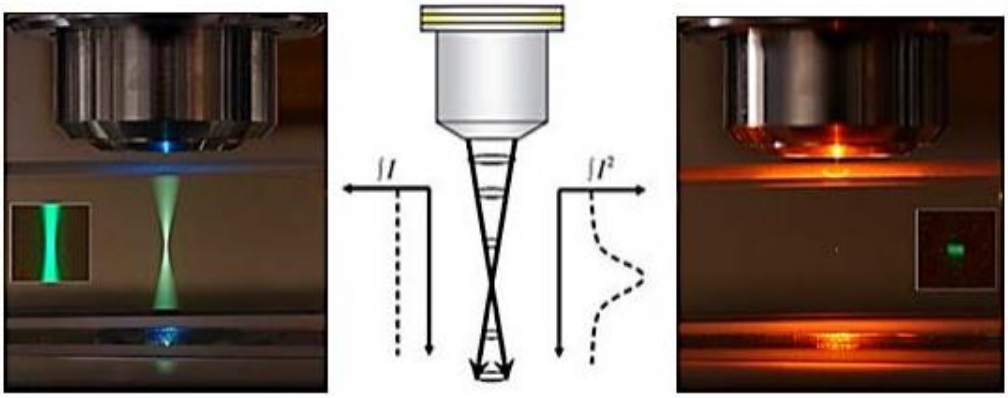


***Figure 1.5.1:*** Fluorescence Effect Of a Photopolymer Solution Caused By Single-Photon Excitation From a UV Lamp (left) And Two-Photon Excitation From a fs Laser (right) [13]

It should, also, be noted that this nonlinear effect of MPP requires the use of ultrashort laser excitation. Thus, a femtosecond laser is ideal for MPP since it carries much greater peak power

and can easily enable multiphoton absorption. Multiphoton absorption has an extremely small cross-section, and it is confined to occur only in a small 3D volume around the close vicinity of the laser focus, less than the cubic wavelength ($\lambda^3$). So, a quite high 3D spatial resolution can be achieved in the pinpoint exposure. An additional advantage of using femtosecond laser pulses is that the photon energy is deposited much faster than electrons could transfer it to the lattice or molecule/atom oscillations through phonon emission, meaning that the excitation is a heat insulation process. This provides ideal optical excitation means for many photochemical or photophysical reactions where thermal effects, which make the process difficult to localize, are not desired. In addition, for many dielectric materials, there is a transparent window in the red-NIR spectral region, which is covered neither by electronic band-band absorption nor by atomic/molecular oscillation absorption. It happens that the fundamental wavelength of general femtosecond lasers is located in this regime, for example, 680–1000 nm for Ti: Sapphire laser. Therefore, a femtosecond laser can penetrate into and tailor desired structures from inside transparent materials, giving an intrinsic 3D processing capability [10].

## 1.6 Material Synthesis (SZ2080)

Each structure of this thesis was fabricated using the hybrid organic–inorganic photoresist SZ2080. Its main components are Methacryloxy-Propyltrimethoxysilane (MAPTMS), Methacrylic Acid (MAA) which serves as the source of organic monomers, Zirconium Propoxide (ZPO) for the formation of inorganic network, 4,4'- Bis(diethylamino) Benzophenone (BIS) as photoinitiator. All these chemicals were purchased from Sigma-Aldrich.

The preparation of the composite started by hydrolyzing MAPTMS using HCl solution (0.1 M) at a ratio of 1:0.1. Then, the ZPO was stabilized by the MAA monomers at a molar ratio of 1:1 and after 5 minutes, the Zirconium complex was slowly added to the hydrolyzed MAPTMS at a 2:8 molar ratio. Afterwards, the PI was added to the mixture at a 1% mass ratio to the monomers. Finally, after stirring for 15 more minutes, the composite was filtered using a 0.22 μm syringe filter. The final samples were prepared by drop-casting onto 100 micron-thick silanized glass substrates, and the resultant films were dried at 55 °C for 60 minutes before the photopolymerization.

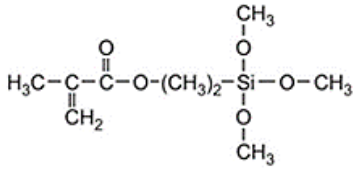

**Methacryloxy-Propyltrimethoxysilane (MAPTMS)**

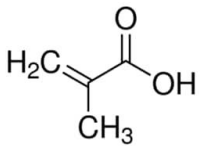

**Methacrylic Acid (MAA)**

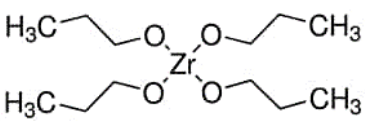

**Zirconium Propoxide**

**(ZPO)**

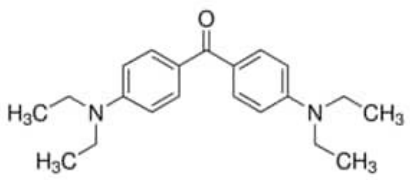

**4,4'- Bis(diethylamino) Benzophenone (BIS)**

# 2.Laser Beam Shaping

## 2.1 Beam Shaping

Beam shaping refers to the process of redistributing the irradiance and the phase of an optical beam. Generally, the irradiance profile is defined by the shape of the laser beam while the propagation characteristics are affected by its phase. So, there is an increasing interest related to beam shaping techniques due to the fact that the at will-alteration of the beam's profile is a key aspect for its propagation properties and the irradiance profile (*fig. 2.1.1*). This process of controlling optical beams is an enabling technology, used in several sectors of scientific, engineering, and industrial research and development, such as materials processing, medical applications, and lithography, that can, also, be applied in both coherent or incoherent beams.

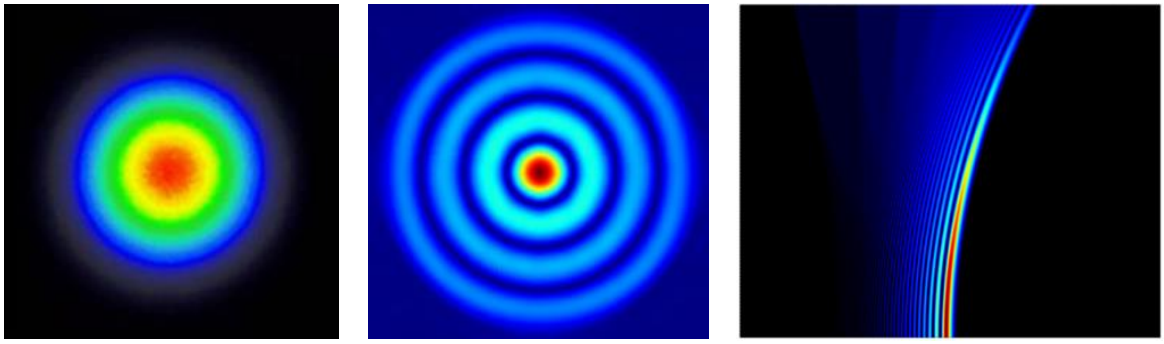

***Figure 2.1.1:*** Simulated Laser Beam Intensity Profiles For a) Gaussian b) Bessel c) Airy Beams [14],[15],[16]

In the general beam shaping problem (*fig.2.1.2*), a beam, incident upon an optical system with one or more elements, must be transformed by this system into the desired output. If the desired output only demands a certain irradiance distribution but allows phase variations, then this problem refers to incoherent beams. On the other hand, in coherent beams there is not, always, the need to constrain the phase of the beam at the output plane[17],[18].

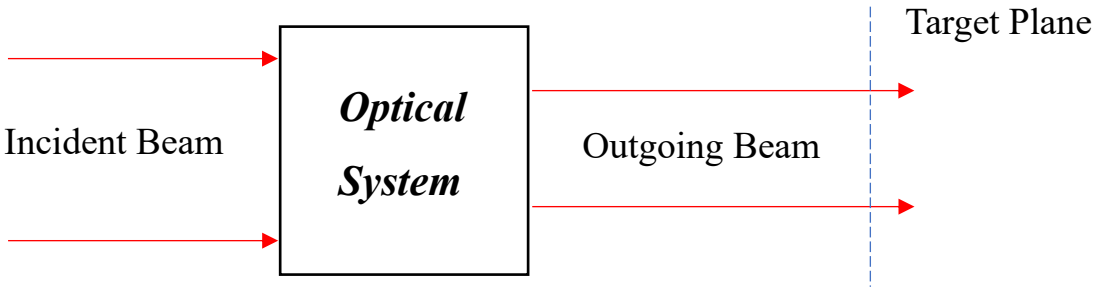


***Figure 2.1.2:*** General Beam Shaping Problem

The first step to understand beam shaping is taken by focusing in phase modulation. So, let us use as an example the Harmonic plane wave equation:

$$U(\mathbf{r},t) = u_0 e^{i(\mathbf{kr}-\omega t)}, \quad \mathbf{k} \equiv n\frac{2\pi}{\lambda_0}\hat{\mathbf{k}}$$

where k is the wave vector normal to the wavefront, n is the refractive index, $u_0$ is the wave's amplitude and the term $(\boldsymbol{kr} - \omega t)$ describes the phase of the wave.
If we assume that the wave propagates along z axis:

$$\left.\begin{array}{r} \hat{\mathbf{k}} \equiv \hat{\mathbf{z}} \\ \mathbf{k} \equiv \mathbf{n}\dfrac{\mathbf{2\pi}}{\boldsymbol{\lambda_0}}\hat{\mathbf{k}} \end{array}\right\} \mathbf{k} \equiv \mathbf{n}\frac{\mathbf{2\pi}}{\boldsymbol{\lambda_0}}\hat{\mathbf{z}} \Rightarrow \mathbf{kr} \equiv \frac{\mathbf{2\pi}}{\boldsymbol{\lambda_0}}\mathbf{nz}$$

the previous equation corresponds to the optical path, meaning the path that light follows when travelling through an optical system. Now, the harmonic wave equation becomes:

$$U(r,t) = u_0 e^{i(\frac{2\pi}{\lambda_0}nz-\omega t)}$$

By observing these equations, it is realized that the modulated phase of a plane wave can be derived by measuring the optical path length that a beam follows when interacts with an optical system. Thus, we can safely conclude that the phase is equivalent to the optical path. This is a highly important result since it facilitates the problem of phase determination for beam shaping. More precisely, the shaping of a wavefront now becomes a matter of spatially controlling the optical path length (OPL) of each point in the wavefront. The OPL is defined by the product of the refractive index n of a specific medium, with the physical length d of the medium

$$OPL=nd$$

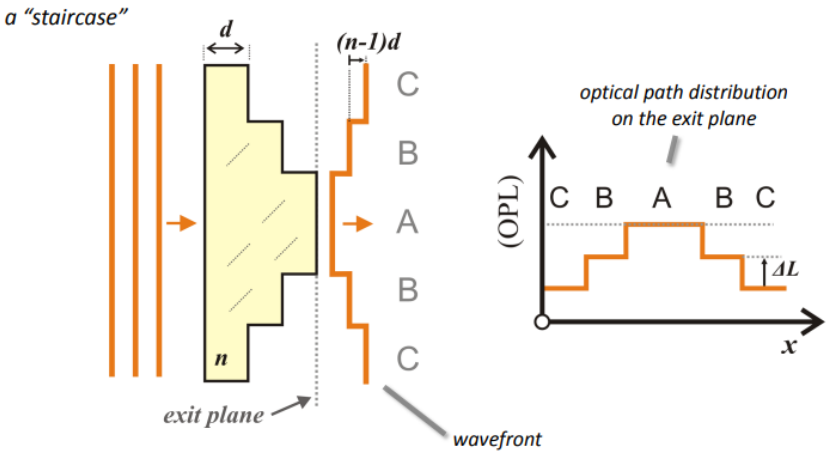


***Figure 2.1.3:*** Wavefront Shaping Example [19]

In figure (2.1.3), the so-called “staircase” wavefront shaping example of a beam is illustrated. Plane waves, incident upon an optical element with refractive index n, can be seen behind the exit plane. The outgoing wavefront modulation occurs due to the different optical path lengths that the light follows point by point into the optical element. The next logical leap is to calculate the optical path difference which is equal with the phase shift that occurs when the wave passed through the material with n appearing to travel a greater distance than an identical wave in air. By analyzing the different optical paths, we obtain

$$\left.\begin{array}{c}(OPL)_A = 3nd \\ (OPL)_B = 2nd + d \\ (OPL)_C = 2nd + 2d\end{array}\right\} \Delta L = (OPL)_A - (OPL)_B = (OPL)_B - (OPL)_C = (n-1)d$$

where, ΔL is the optical path difference. ΔL indicates that we can determine the phase difference and the phase modulation that will appear to the beam by controlling the optical path difference, or, in other words we can achieve beam shaping by spatially controlling the optical path delay of each point in the wavefront. The simplest and most common example of wavefront reshaping is the action of simple converging or diverging lenses (*fig. 2.1.4*). These lenses reshape a plane wavefront in a way so that it is converted to a spherical one since each plane wavefront travels a different optical path distance [19],[20].

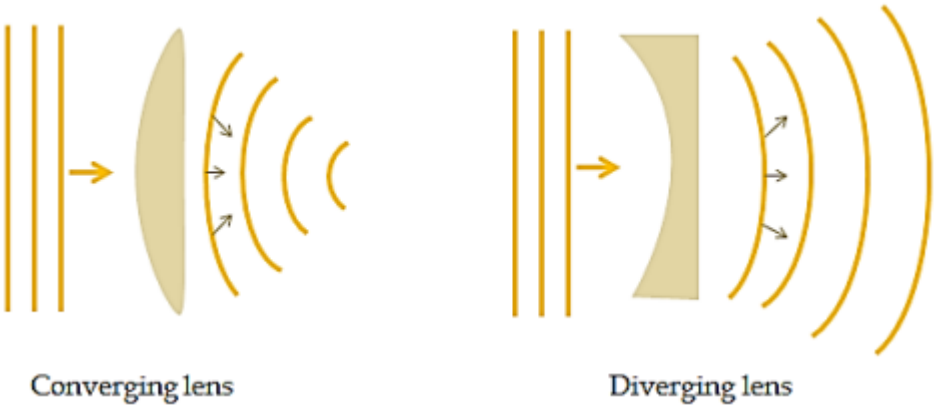


***Figure 2.1.4:*** Converging/Diverging Lenses Wavefront Shaping Action: plane waves reshaped into spherical [19]

## 2.2 Holographic Beam Shaping

Holography and specifically the use of Computer-Generated Holograms is one more method for laser beam reshaping, which was employed in this MSc research as a technique for advanced laser material structuring. As described before, the need of an alternative writing technique rises from the fact that conventional Direct Laser Writing fabrication is connected

with important issues such as long fabrication time, lack of parallel processing and low scale structuring. A hologram can be a tool for shaping the amplitude and the phase of a light wave. Along this direction holographic lithography in accordance with focal beam engineering for advanced, multiscale, and tunable fabrication can be employed for optimized materials engineering applications.

## 2.3 4f Optical System

4f optical or canonical optical system (*fig. 2.3.1*) is an important imaging system able to perform Fourier transform. It consists of two lenses and a phase mask that is placed one focal length behind the first lens or one focal length in front of the second one. In between the two lenses, we have the Fourier plane. There is the point where we have the Fourier transformation of the object placed at the output plane. At the Fourier plane, we can place masks of different shapes and opacities that can filter-out unwanted components from our original image. The Fourier transformation of an image is very similar to a diffraction pattern, where low frequency components are located close to the optical axis and higher frequency ones are placed further away from the origin. The shape of the mask varies depending on the application that we need to employ.

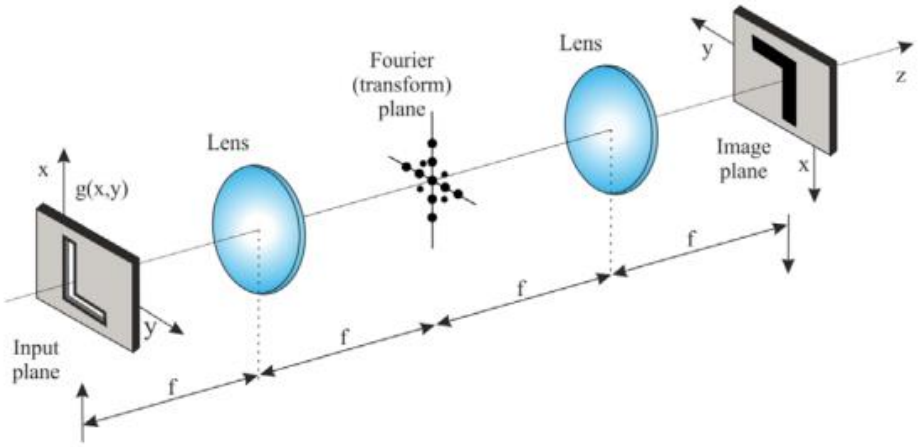


***Figure 2.3.1:*** Typical 4f Optical System Setup [21]

Analytically, in figure (2.3.1), we assume that a plane wave travels from left to right meeting a transparency at the input plane. The transparency is located one focal length in front of the first lens (input plane) and contains a function, g (x, y) that leads the plane wave to experience phase and amplitude modulation as a response to the Fourier transform of the function, g(x, y). The transformed field t(x, y) then forms an initial 'image' at the distance of one focal length behind the first lens (transform plane) where the Fourier transform of g(x,y) is g′(kx, ky). Masking filters can be placed at the transform plane as they allow to make frequency filtering and remove some lines, shapes, or contours from origin image in order to obtain a new modified image. The phase mask that is placed at the transform plane is built so that it contains the product of Fourier transform, t′ (kx, ky), for the transformed field. After the transform

plane, the field can be expressed by the relation g′(kx, ky) × t′(kx, ky) and the Fourier transform of this field is reconstructed at the back focal plane of the second lens (image plane). It is worth noting that for 4f system the transfer function that was mentioned in a previous part is in fact the function t′(kx, ky) of the phase mask. Overall, the process can be described as two Fourier transforming procedures and a correlation between g(x, y) and t(x, y) that lead to an inverted image of the initial object, i.e., the transparency [21],[22].

## 2.4 Spatial Light Modulator

Spatial Light Modulators (SLMs) can be described as devices able to alter the properties of the incident light including phase, amplitude, and polarization. They are usually computer controlled and after the appropriate programming operations they can replace most of the conventional optical elements, such as lenses or mirrors. As a beam converter, SLM is usually placed at the back focal plane of a Fourier transforming lens [23],[24].

The input information of the SLM can be represented both by electrical signal and optical image. In the former case, electrical signals directly drive the device in such a way to control its spatial distribution of absorption or phase shift. In the latter case, the information may be input to the SLM in the form of an optical image at the start rather than in electrical form. Often, a SLM device may have two different forms, one suitable for electrical and one suitable for optical addressing.

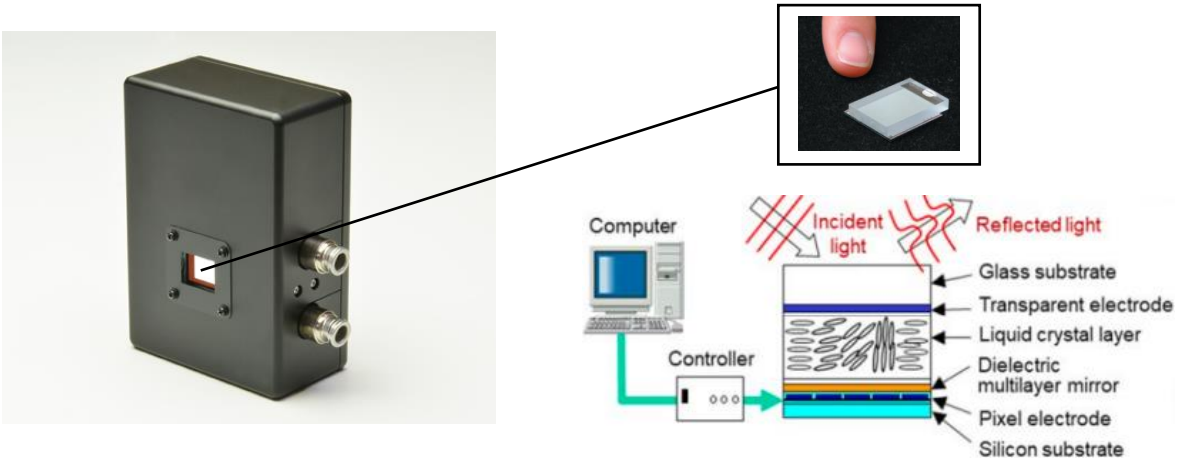


***Figure 2.4.1:*** Basic components and operation of Liquid Crystal on Silicon-Spatial Light Modulator (LCoS-SLM) [25]

Liquid Crystals (LC) are the main component of SLMs and their ability to convert light is a result of LC properties. Liquid Crystals are found in an intermediate state between solid and liquid phases, and they consist of rod-like organic molecules with properties from both liquids and solids. When appropriate conditions are applied LCs align to a preferred direction, but a certain degree of motion is allowed. In addition, their elliptical shape allows them to form dipoles resulting in easy control under external stimuli. So, SLM is a pixelated display that consists of cells filled with LC that are externally controlled.

One widely used type of SLM (*fig. 2.4.1*), which is also employed in this master thesis, is the Liquid Crystal on Silicon phase only reflecting SLM (LcoS-SLM). In a LcoS-SLM, liquid crystals are covered in one side by a transparent alignment film, following a transparent electrode layer and a flat glass substrate. On the other side, there is, also, a transparent alignment film and a mirror. The mirror is then covered by pixelated metal electrodes powered by an active-matrix circuit that gives them the ability to control LCs at each pixel. Below the pixelated metal electrodes lies a silicon substrate.

The basic mechanism of action of a SLM device involves the phase modulation of the incident beam according to the alignment of the LCs. A laser beam incident to the LCOS-SLM is phase-modulated and then reflected to freely control the wavefront of (reflected) light as needed. This ability to accurately control the light wavefront makes the LCOS-SLM ideal for applications such as optical beam pattern forming. During the modulation, Liquid Crystals are externally controlled via a computer that sends signals to pixelated electrodes. This direct conversion of the signals into a spatial distribution of optical information is used to encode the phase of the incident beam. In other words, when voltage is applied in electrodes, LC dipoles change polarization leading to phase modulation. For a given applied voltage, LC molecules tend to rotate by a predefined angle, forming a birefringent-like material for a particular orientation of incoming polarized light. That means that they develop different refractive indices according to polarization.

The voltage, and hence the phase shift, are calibrated using grayscale images (usually 8-bit encoding, allowing 256 colors), i.e., phase masks. In this way, each gray level is directly associated with a discrete increment of the phase from 0 (black) to $2\pi$ (white), and a linear relation for the intermediate values. Therefore, $2\pi/256$ phase increments can be encoded at each pixel on the LC display by displaying an 8-bit (256) pixelated image, which can easily be generated using computer software. So, all these characteristics explain how SLMs can easily modify the properties of an incident bean and why a great interest around their technological developments has been awaken [23],[26].

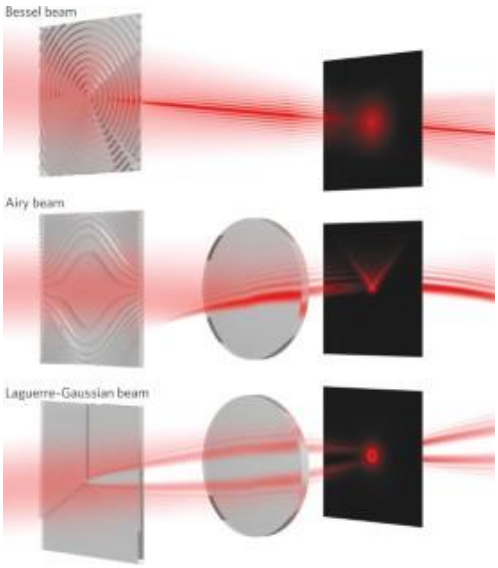


***Figure 2.4.2:*** Examples of shaped light beams using Spatial Light Modulator (SLM) [26]

## 2.5 Designing Of The Phase Masks

The grayscale images or phase masks can be described as images or holograms that, nowadays, are produced after the writing and the execution of an appropriate code (Computer Generated Holograms - CGHs) which is built based on the desired beam profile (*fig. 2.5.1*). Typical phase masks consist of n by m pixels, which means there are m rows pixels, and each row has n pixels. CGHs have the advantage that the patterns that must be displayed do not have to exist in the real world [23],[27].

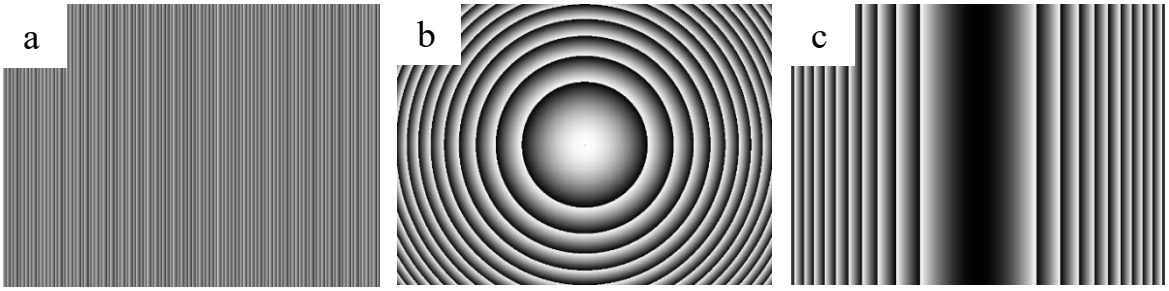


***Figure 2.5.1:*** Examples of Computer-Generated Holograms (CGHs) encoded for a) tilted phase b) spherical and c) cylindrical wavefront shaping

When a beam passes through the mask, phase and amplitude modulation occurs resulting in a different geometry of the laser beam profile. Most modern devices, such as Spatial Light Modulators (SLMs), use phase-only masks, but there are techniques to convert from a phase-only device response to a full amplitude-phase response (complex amplitude modulation). The basic step of complex amplitude modulation is to trace the equation that best describes the optical field of the beam before and after modulation and then trace the transfer function of the optical element that will execute the change between the two optical fields. For example, considering a typical optical field $u=u_0\, e^{i\varphi}$ that must be transformed into a second one $u'=u_0'e^{i\varphi'}$, the transfer function of the phase mask will be given by

$$t = \frac{u'}{u} = \frac{u_0'}{u_0} e^{i(\varphi'-\varphi)}$$

where $u_0$, $u_0'$ the amplitudes and $\varphi$, $\varphi'$ the phases of optical fields. If the coded mask gains the desired phase, then it will, also, gain the transfer function's expected properties.

In most complex modulation approaches, a high spatial frequency is added to the field in order to produce the desired amplitude and phase. The undesired light can be filtered, and it is found in the higher diffraction orders as a result of the fact that the spatial frequency is high. To provide a better description, let us consider the complex plane diagrams below (*fig. 2.5.2*). It is possible to realize any position on the unit circle in the complex plane because these are phase-only values and therefore "allowed" by the SLM. The effect of beating between two such values at positions A and B is to produce a new amplitude and phase that is not on the unit circle, i.e., a non-unit amplitude with any desired phase.

$A=e^{i\varphi+ia}$ , $B=e^{i\varphi-ia}$

with t=cos(a).

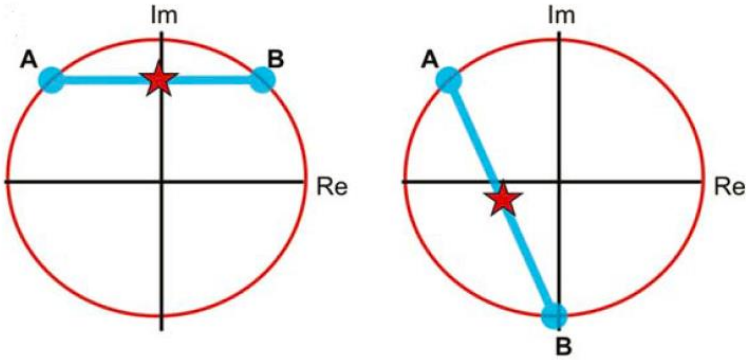


***Figure 2.5.2:*** A pure phase modulation is equivalent to tracing a unit circle in the complex plane. To introduce amplitude modulation, the radius of the circle must be allowed to take on values of <1. This is equivalent to moving off the unit circle to any point inside the unit circle. One example would be to modulate between two points on the circle (A and B). The result of which would be a point inside the circle (star) [23]

Since the hologram is a complex function, the main idea is to devise a binary pattern to approximate the complex hologram. The construction of the mask starts by dividing the area of the hologram into an array of unit cells (pixels) with the size of each cell being w×w (*fig. 2.5.3 (a)*). If we suppose that phase and amplitude within any cell vary slowly, cells can be replaced by an array of point sources (*fig. 2.5.3 (b)*) [23].

For phase-only masks amplitude can be ignored. So, only phase must be extracted and then produce a gray-tone pattern, whose gray-level is proportional to the phase. The final pattern will have a checkerboard-like form of phases A-B, B-A, and so on. Then, the pattern can be displayed on a phase-only spatial light modulator in order to produce the desired beam [28].

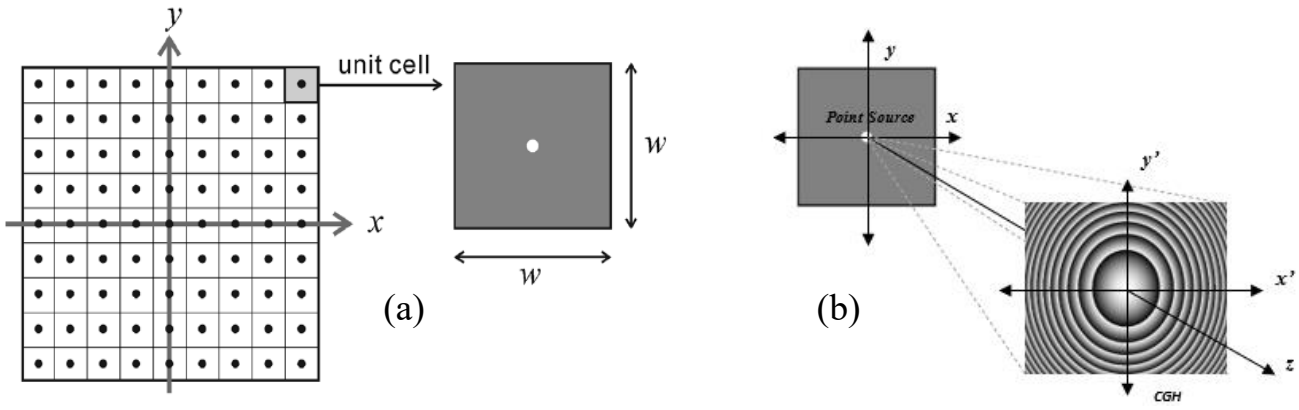


***Fig. 2.5.3:*** a) Complex phase mask (hologram) divided into unit cells b) Point source created by Computer Generated Hologram (CGH) [27]

As mentioned in part (2.1), the phase is equal with the length of the optical path that a beam follows during its interaction with an optical medium. Thus, during the designing of the masks, it is easy to control the shape of the wavefront by spatially controlling the optical path delay of each point in the wavefront. In a phase mask that is translated into pixel-by-pixel control of the optical path delay.

# 3. Multi-Foci Laser Writing

## 3.1 Multi-Foci Photopolymerization

Since the conventional Direct Laser Writing technique provides high spatial resolution but with long processing time due to the voxel-by-voxel polymerization, alternative techniques must be employed for the fabrication speed to be improved. Following this thought, an interesting alternative technique is the Multi-Foci Laser Writing method for the fabrication of high-resolution periodic structures.

The main idea behind the Multi-Foci Laser Writing is to multiply the number of simultaneous features fabricated on the same sample. This is able by using a SLM device where a specifically created Hologram increases the number of polymerizing spots focused inside the photoresist. There are, also, more straightforward ways for producing multiple focusing spots, such as beam splitters and micro-lens arrays, but they lack the capability of quickly reconfiguring the spots pattern. So, a SLM device has an additional advantage due to the easy reconfigurability that allows for on-the-fly change of the foci pattern during the fabrication process with a frame rate typical of computer screens [29],[30].

For the phase masks (Holograms), we use the following computer-generated holographic approach: light emitted by a set of N point sources interferes with a reference plane wave that propagates along the z axis. This interference, assuming linearly polarized light, can be described at the plane of the SLM as

$$\boldsymbol{E_s(r,s) = E_0 e^{i(kz-\omega t)}\hat{x} + \sum_{i=1}^{N} E_i\,(r_i - r_0, t)}$$

where $r_0$ is the position of the SLM screen, $r_i$ is the position of each point source, $\boldsymbol{E_i\,(r,t)} = \boldsymbol{E_i e^{\,i(k|r|-\omega t+\varphi_i)}}$, **x** is a spherical wave of amplitude $E_i$ emitted from point source with index i, k is the wavenumber, and $\varphi_i$ is a constant bias phase for every point source. Through a special designed code, we are able to modify the number of the beams, the distance between them, the phase of the beams and the point of the hologram reproduction after the initial beam pass through the SLM device, which gathers the selected information, too. Each designed phase mask must be an 8-bit grayscale image. In this way, each gray level is directly associated with a discrete increment of the phase, from 0 (black) to 2π (white), and a linear relation for the intermediate values. Therefore, 2π/256 phase increments can be encoded at each pixel on the LC display by displaying an 8-bit (256) pixelated image, which can easily be generated using a computer software. In our case, this is the same software that we write the code for the phase masks (i.e., Image J software) [29],[30].

## 3.2 Processing Time Acceleration

Tailoring of Multi-Foci distributions using a SLM device can significantly improve the fabrication time of laser lithography procedures since it secures parallel materials processing. Each focal spot can act similar to the way that a laser beam acts at Direct Laser Writing. So, in theory, if we assume that the number of these multiple focal points is N, then the patterning speed is expected to be increased at least N times (*fig. 3.2.1*). Of course, that means that N times of laser power is needed for the patterning. The resolution of the Multi-Foci method is also confined by the optical diffraction limit.

This approach offers an additional advantage related to the fabrication speed acceleration. The advantage lies in the fact that, by using multiple focal points, we do not only employ just another method for rapid fabrication among other possible proposed methods, but that are, also, mainly used in a lab-related environment and where most of the produced structures are connected with low scale experiments. Instead, this technique combines the need for rapid fabrication of arbitrary high-resolution periodic structures in both experimental and real-life environments. Thus, it can be used for many practical applications, i.e., photonic and metamaterial surfaces, liquids filtering, photocatalysts or scaffolds for tissue engineering, where long-scale (or macroscopic) dimensional structuring in short processing times is required. Moreover, the periodic characteristics of each structure are dynamically modified in real time by simply altering the distance between the different focal points or, in other words, by simply alternate the phase mask in the SLM.

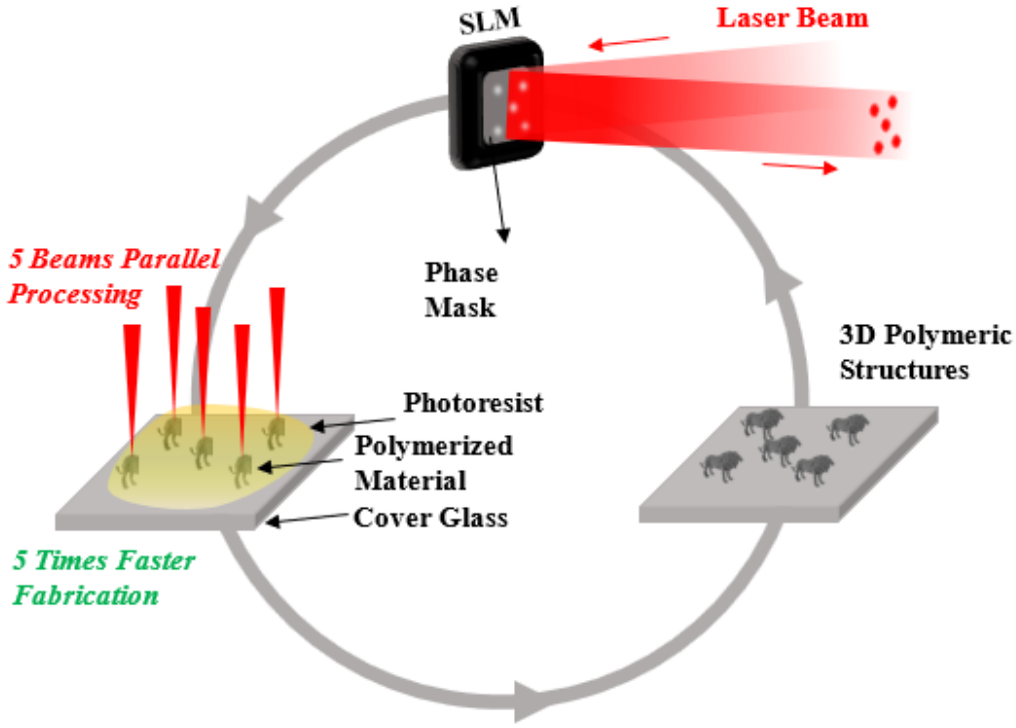


***Figure 3.2.1:*** Typical Polymerization Process Using Multi-Foci Method

# 4. Pulsed Laser Deposition

## 4.1 Pulsed Laser Deposition (PLD)

Pulsed Laser Deposition (PLD) is a physical vapor deposition technique for growing thin films up to several thousand angstroms (A˚) thick. It has a relatively simple setup where a pulsed laser beam is used for vaporizing the target material that needs to be deposited as thin films on a substrate. The PLD system is composed of a vacuum chamber with at least one window possessing transparency to the incoming laser wavelength. Within the vacuum chamber, two main components must be present: the target and the substrate holder (*fig. 4.1.1*). These two components are separated by an easily controlled predefined gap. Short laser pulses have the advantage of congruent evaporation that allows PLD to preserve stoichiometry during mass transfer from the target to the thin film. So, the high-powered pulsed laser beam leads to a rapid removal of material from a solid target with the desired composition. This process can occur in ultra-high vacuum or in the presence of a background gas, such as oxygen when depositing films of oxides [31], [32], [33], [34].

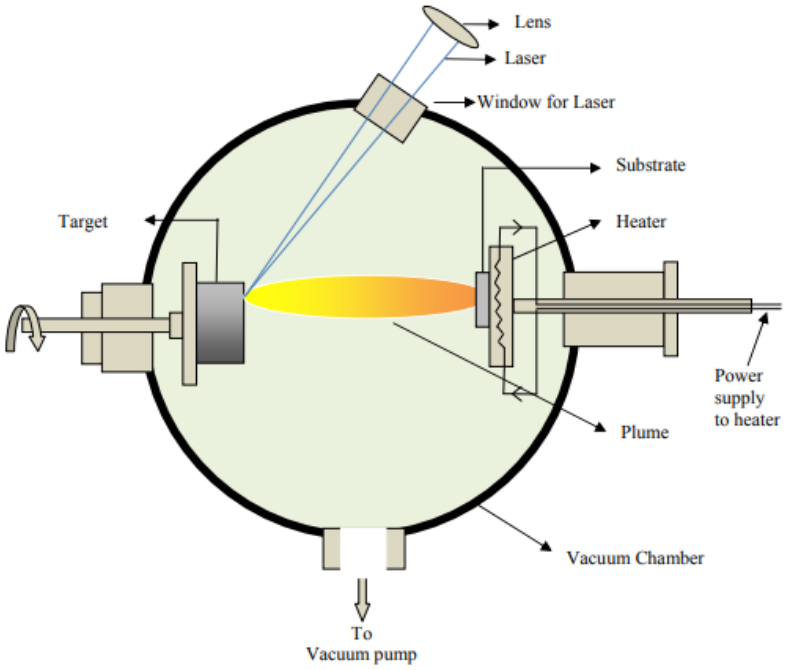


***Figure 4.1.1:*** Schematic Illustration Of A Typical Pulsed Laser Deposition Technique And Its Mechanism [35]

During the irradiation of the target, light is absorbed by the material, and the outcome is governed by the value of incident laser power density in relation to an ablation threshold. The laser pulse would just heat the target if the laser fluence (laser power density) was less than the ablation threshold i.e., a threshold determined by the target material, its absorption coefficient, the wavelength, and duration of the laser pulse. Only when the laser fluence is high

enough to exceed the ablation threshold does the target material vaporize. Then, a finite volume of solid target material is converted into vapor phase elements such as ions and neutrals, forming a high temperature "plasma plume", which then condenses onto a substrate. In order to achieve the deposition, the substrate must be placed inside the chamber of the PLD setup in a way so that it faces the target. Thus, the ablation plume that expands adiabatically can move vapors from the target material to the substrate (*fig. 4.1.2*). In contrast to the simplicity of the technique, the mechanisms in PLD—including ablation, plasma formation, and plume propagation, as well as nucleation and growth—are rather complex [32],[33],[34].

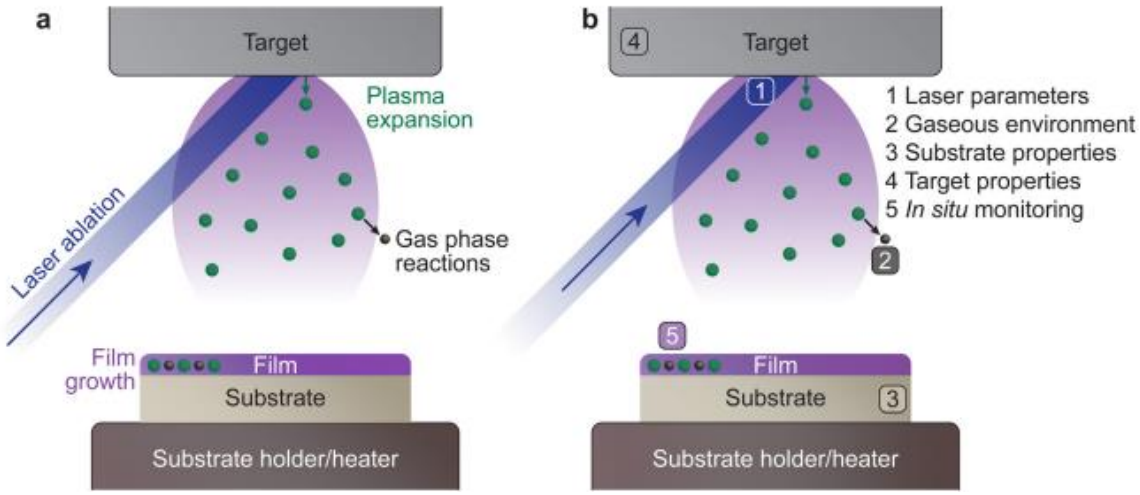


***Figure 4.1.2:*** Schematic Illustration Of a) The Main Processes Involved In Pulsed Laser Deposition b) The Main Parameters Tailored During The Pulsed Laser Deposition Process [32]

## 4.1.1 Lasers

The most common lasers used for PLD are gas (excimers, or excited dimers; electrically pumped) or solid-state lasers (optically pumped), for example the higher harmonics of an yttrium aluminum garnet (YAG) laser due to their high output power. The pulse length affects the laser ablation process and determines how much thermal effects dominate. Most PLD systems employ nanosecond lasers possessing a laser pulse length between 10 ns and 25 ns, which has proven over time to be the optimal window with respect to plasma properties and oxide thin film growth. The pulse shape and repetition rate can also affect film growth [32].

## 4.1.2 Vacuum Chamber

The vacuum in the chamber is achieved by a series of turbo molecular and rough pumps. The base pressure in vacuum chambers used for PLD is generally between $10^{-6}$ mbar and $10^{-9}$ mbar. Without considering other sources of contamination in the chamber, the vacuum level determines how fast a single surface layer of contaminants and impurities can form on the

surface of the substrate. Under low vacuum conditions (i.e., 0.1 mbar), a layer of contaminants forms in a few microseconds. However, reducing the pressure provides a more stable environment whereby fewer contaminants are present in the chamber, thus drastically increasing the timeframe for the formation of a contaminant layer. How far a molecule travels before it collides with another molecule is defined as the mean free path. The level of vacuum affects the mean free path, λ, of the species present in the chamber and thus the entire plasma dynamics [32].

### 4.1.3 Target and substrate holder

There are several different target shapes, which are used for ablation. All of them offer certain benefits, but also hold drawbacks dependent on the goals of the experiment. The two common types of targets are either rod-shaped or thin plates in the form of a disk. Common to all targets, the location of the laser beam on the target must be moved to avoid material removal induced cratering of the surface. As the optical path of the laser is usually fixed, the target is moved throughout the deposition.

The rod-shaped target holder is typically mounted to a spindle, which enables the rotation of the target and an automated height modulation between two limit switches. These movements are necessary to ensure homogeneous ablation of the entire target surface area. The primary advantage of this geometry is its mechanical simplicity. With this geometry, multilayered heterostructures can be fabricated by stacking rods of different materials on top of each other. Conversely this type of target holder is sensitive to the positioning of the target. The rotational motion can induce lateral shifts if the target is not centered properly or if the side walls are corrugated, which affects the position of the laser spot and subsequently can alter the direction of the plume with respect to the substrate position. Considering the laser spot typically possesses a rectangular shape at the target surface, alignment of the long axis of the laser spot with the long axis of the target can result in a higher degree of thickness homogeneity, with large area coatings on substrates up to 20 cm x 20 cm demonstrated in literature.

The main drawback of the rod-shaped target is that the poor sintering properties of many materials make the fabrication of sufficiently long rods very challenging and sometimes impossible, whereas disk or plate shaped targets are generally easier to prepare. In contrast to the movement of the rod target, the disk target is either rastered or rotated. The rastering path can be customized to any combination of x–y axis movements. A combined rotation/rastering motion is also possible.

A high substrate temperature is one of the requirements for the growth of crystalline materials. Hence, the substrate holder is part of a heating system, allowing film growth at temperatures of up to 1000 °C. These are mostly resistive heaters. Recently, laser-based heating set-ups have become more common, offering an increase in flexibility for heating ramps and deposition temperatures up to 1500 °C. The geometry of these components impacts the film growth, contributing to many disparities between PLD systems and thus inconsistencies in material growth between differing chambers. For example, the geometry of the heater determines the

size of the heated zone, and therefore the heated volume in the chamber, including the temperature at the target surface. Changes in heated volume in front of the substrate can affect the local density of the incoming plasma and consequently modify the growth process. It is common to observe a color change of an oxide target material during ablation when using a small-area heater, which occurs due to the removal of oxygen. Conversely, depositions utilizing a large area heater in an oxygen atmosphere allow sufficient heat transfer to re-oxidize the target during ablation.

The size and shape of the heater, as well as how the thermal contact between heater and substrate is ensured, are among the main reasons for the relatively wide range of deposition parameters reported in literature for the same material [32].

### 4.1.4 PLD Advantages

Laser ablation for thin film growth has many advantages against classical thermal growth techniques like chemical vapor deposition (CVD), metalorganic chemical vapor deposition (MOCVD) or ion-beam growth techniques like molecular beam epitaxy (MBE). Examples of the advantages that laser ablation are [36]:

- the energy source is outside the vacuum chamber which, in contrast to vacuum-installed devices, provides a much greater degree of flexibility in materials use and geometrical arrangements.

- almost any condensed matter material can be ablated.

- the pulsed nature of PLD means that film growth rates may be controlled to any desired amount.

- the amount of evaporated source material is localized only to that area defined by the laser focus.

- under optimal conditions, the ratios of the elemental components of the bulk and film are the same, even for chemically complex systems.

- the kinetic energies of the ablated species lie mainly in a range that promotes surface mobility while avoiding bulk displacements.

- the ability to produce species with electronic states far from chemical equilibrium opens the potential to produce novel or metastable materials that would be unattainable under thermal conditions.

## 4.2 PLD Ablation Mechanism

The ablation of the target material by laser irradiation, the development of a plasma plume with high energetic ions, electrons, and neutrals, and the crystalline growth of the film itself on the heated substrate are all very complex mechanisms. So, it would be easier to understand these mechanisms by analyzing each one of them separately. Thus, the stages that follow a typical PLD method are analyzed below.

### 4.2.1 Laser Absorption

As a general principle, the target material must be able to absorb the applied wavelength in order to be physically removed. However, this principle is not fully applied in ultra-short laser pulses for material removal. In this case, laser ablation proceeds via thermal and nonthermal processes, and is often a combination of both (*fig. 4.2.1 (a)*). Even though these processes take place on different time scales, the combination of both contributes to the formation of a plasma plume.

Non-thermal interactions dominate the first stage of the laser ablation, whereby incident photons provide enough energy to induce band transitions as the target material absorbs the light. The main non-thermal absorption mechanism takes place via the excitation of an electron by an incoming photon. The electron undergoes an intraband transition from the ground state to an excited state and the excited electron relaxes through electron–phonon coupling. It is also possible to have an excitation of one molecule by two incoming photons.

When this process occurs within at the picosecond timescale or shorter, the energy of the two photons is combined to promote the molecule into an excited state. This is called multiphoton excitation and can be either coherent or sequential. The properties of the material can affect this absorption process as, for instance, the presence of defects can modulate the light absorption properties (i.e., the band gap). The extent to which the photons propagate through the material can be calculated by the Beer–Lambert law,

$$A = \frac{I}{I_0} = \varepsilon c t$$

where A is the absorbance, I the light intensity, $I_0$ the incident light intensity, ε the molar extinction coefficient, c the molar concentration and t the thickness. The above equation can be used to calculate the penetration depth of the absorbed laser light and estimate the extent of the non-thermal processes.

The second type of interaction is thermal excitation. One of the main attributes of laser-induced thermal excitation is the rapid heating in a localized area to temperatures exceeding several thousand Kelvin. The vibrational relaxation of excited electrons (electron–phonon

coupling) transfers heat to the system on a picosecond timescale. The typical PLD pulse duration of approximately 20 ns is therefore long enough for thermal processes to dominate. As part of these processes, the surface heat will propagate into the bulk of the target, which can cause unintended side effects (e.g., mechanical stress, micro-crack formation, solidification, and remelting, among others).

Consequently, the material is ejected from the target following a combination of electronic and thermal ejection mechanisms. The exposure of a molecule to excess electrons causes instability, which results in its desorption, fragmentation, or ionization from the target surface. Hence, the thermal ejection following laser impact is the result of heat-induced bond cleavage through evaporation or bond dissociation. This process is further aided by intermolecular collisions, leading to excitations and ionization in the very dense vapor, while still interacting with the incoming laser pulse [32].

### 4.2.2 Plasma Formation And Expansion

The absorption of the laser light does not only occur to the solid target material, but in the initial vapor of the removed material, too. In the vapor region, the energy is primarily absorbed by either photoionization or inverse Bremsstrahlung. Photoionization corresponds to electron ejection from an atom following photon absorption, whereas inverse Bremsstrahlung occurs when an electron gains kinetic energy by a collisional energy transfer with other particles. These mechanisms promote the generation of free electrons, which, in turn, increase the degree of ionization of the plasma (*fig. 4.2.1 (b)*).

The frequency of collisions increases with an increasing density of the vapor, forming the so-called Knudsen layer. This layer is a key driver for the consequent expansion mechanism of the plasma plume. It is a near-surface region with the thickness corresponding to a few multiples of the mean free path, where the ejected species have a strongly forward-peaked velocity distribution away from the sample surface. Depending on the density of the layer, the plasma plume will expand first in a collisional manner, contributing to the high degree of ionization and charge separation. This is followed by an adiabatic expansion and a free flight of plume species for an ablation with a background pressure equivalent to a large mean free path. For a background pressure considerably shorter than the target-substrate distance, a shockwave is formed thereby moderating the kinetic energy of the plasma species.

At the beginning of the plasma expansion, a charge separation occurs, while chemical species are accelerated based on their mass. Electrons and light elements lead the plasma plume expansion while heavy species remain at the back. This separation, based on the charge to mass ratio, creates an electrostatic gradient that is equivalent to an electrostatic double layer. Electrons are the lightest and fastest species, and they are splitted into two types: the energetic electrons (called the hot electrons) that are situated at the front of the plume and the cold electrons that trail at the back, well behind the fast ions. The ions inside the double layer are accelerated due to the resulting electric field gradient and the time spent in this region determines the maximum kinetic energy of the species. The presence of the double layer affects

the expansion dynamics of both heavy and light species, and subsequently the number of species reaching the substrate [32].

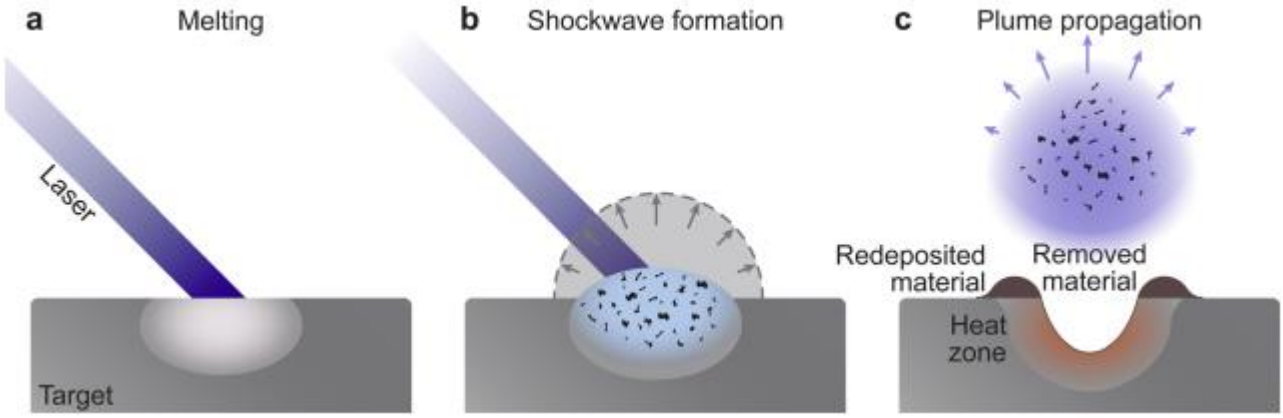


***Figure 4.2.1:*** Schematic Illustration Of The (a) Melting And Instantaneous Vaporization, (b) Shockwave Formation And (c) Plume Expansion After The Termination Of The Laser Pulse [32]

## 4.2.3 Film Nucleation And Growth

The growth of a thin film proceeds through a series of steps. Arriving species either impinge on the surface, diffuse, and begin the nucleation process, bounce, or desorb. These processes are temperature and deposition rate dependent.

Upon reaching the substrate, the species forming the plasma plume can physisorb and further chemisorb. The mode of adsorption depends on the effective coverage of the surface. At low coverage, the species follow tracer-like diffusion, whereby atoms hop between energetically favorable sites of the substrate surface. An increased coverage leads to the dominance of Coulomb interaction between neighboring atoms and to a chemical diffusion mechanism. On uniform surfaces without chemical traps, the adsorbing atoms diffuse intrinsically, while the presence of defects pushes the adatoms to adopt a mass transport diffusion behavior.

Mechanistically, the motion of adatoms occurs via hopping between favorable sites, tunnelling through energetically favorable paths, atomic exchange, or diffusion through vacancies. The formation of clusters is influenced by the surface tension of the surface. In the case of thin films, heterogeneous nucleation allows the atoms to aggregate up to a critical radius. The nuclei are stable and continue to grow if they exceed the critical size, otherwise they will dissociate [32].

# 5. Photocatalysis

## 5.1 Photocatalysis Mechanism

The term "photocatalysis" refers to a process where light and catalysts act together to support or speed up a chemical reaction. So, photocatalysis can be defined as "**catalysis driven acceleration of a light-induced reaction.**"

Every photocatalytic reaction is directly depended on the wavelength or light (photon) energy, the catalyst, and the active surface area. Semiconducting materials are used as catalysts since they perform as sensitizers for the irradiation of light stimulated redox processes. This property rises from their electronic structure, which is characterized by a filled valence band and a vacant conduction band [37].

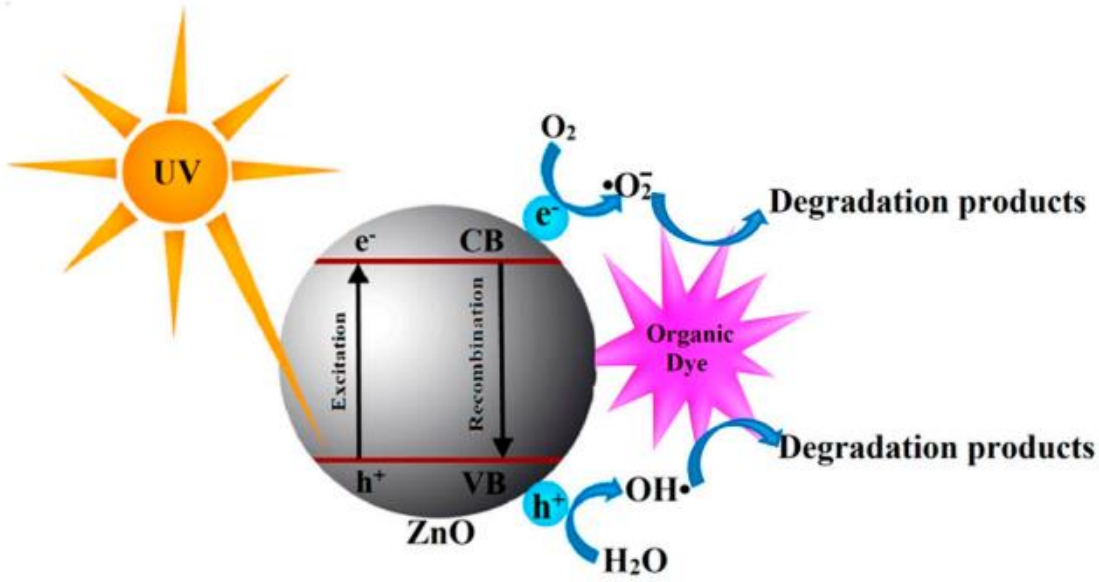


***Figure 5.1.1:*** Photocatalytic Activity Of ZnO Catalyst On Contaminants (Organic Dye) In The Presence Of UV Irradiation [38]

The photocatalytic reaction is initiated only when the light energy of the incident photons, meaning the photons that fall on the surface of a semiconductor, is equivalent or exceeds that of the bandgap energy of the semiconductor. Under this condition, the valence band electrons are agitated and move to the conduction band of the semiconductor leaving empty spots or holes in the valence band. These holes in the valence band can oxidize donor molecules and react with water molecules to generate hydroxyl radicals that have strong oxidizing power and they are responsible for the degradation of pollutants. On the other hand, conduction band electrons react with dissolved oxygen species to form superoxide ions. These electrons induce the redox reactions. The holes and electrons could undergo successive oxidation and reduction

reactions with any species, which might be adsorbed on the surface of the semiconductor to give the necessary products (*fig. 5.1.1*).

There are two general photocatalysis categories: homo- and heterogeneous photocatalysis. In homogeneous photocatalysis, both the reactants and the photocatalysts exist in the same phase while in heterogenous photocatalysis reactants are in a different phase than photocatalysts. Homogeneous photocatalytic processes are mostly related with metal complexes as catalysts (transition metals complexes like iron, copper, chromium, etc.). In this process, under the photon and thermal condition, the higher oxidation state of metal ion complexes generates hydroxyl radicals. These radicals react with organic matter leading to the destruction of the toxic pollutant. As for heterogenous photocatalytic processes, semiconducting materials ($TiO_2$, ZnO, $SnO_2$, and $CeO_2$) function as heterogeneous photocatalysts, because of their favorable combination of electronic structures, which is characterized by a filled valence band and an empty conduction band, light absorption properties, charge transport characteristics and excited states lifetime.

An excellent semiconductor photocatalyst should be:

- able to utilize visible and/or near-UV light.
- biologically and chemically inert.
- Photoactive.
- photostable (i.e., stability toward photo corrosion).
- inexpensive.
- Nontoxic.

Finally, the active surface area of the catalyst is of high importance during photocatalysis. Increasing the surface area leads to an increased number of catalytic sites available for reaction. This is equal to an increased catalyst productivity [37], [39].

### 5.1.1 Oxidation

The water that is found on the surface of the photocatalyst is mentioned as “absorbed water.” This “absorbed water” is oxidized by positive holes that are created in the valence band after the electrons shift that takes place to the conduction band and it is a result of the light irradiation. Oxidation results in the formation of hydroxyl ($OH\cdot$) radicals with strong oxidative decomposing power. Then, hydroxyl radicals are able to react with organic matter present in the dyes initiating their decomposition. If oxygen is present when this process happens, the intermediate radicals in the organic compounds along with the oxygen molecules can experience radical chain reactions and consume oxygen in some cases. In such a case, the

organic matter becomes carbon dioxide and water and ultimate decomposition is achieved. Under such circumstances, organic compounds can react straightly with the positive holes, resulting in oxidative decomposition (*fig. 5.1.2*) [37].

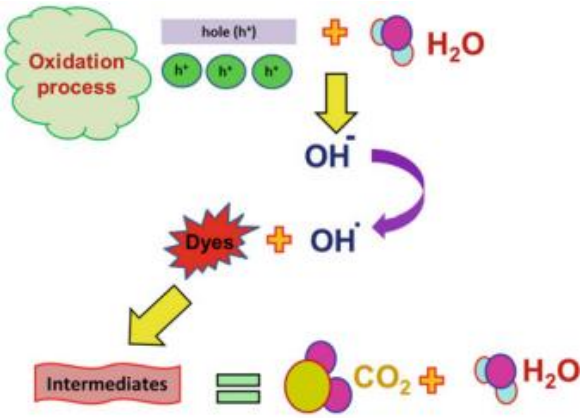


***Figure 5.1.2:*** Oxidation Mechanism [37]

## 5.1.2 Reduction

The reduction of oxygen contained in the air occurs as a pairing reaction. Oxygen reduction can be realized as an alternative mechanism to hydrogen generation due to the fact that oxygen is an easily reducible substance. The conduction band electrons react with dissolved oxygen species to form superoxide anions. These superoxide anions attach to the intermediate products in the oxidative reaction, forming peroxide or changing to hydrogen peroxide and then to water. The reduction is likely to occur more easily in organic matter than in water. Therefore, the higher concentration of organic matter tends to increase the number of positive holes. This reduces the carrier recombination and enhances the photocatalytic activity (*fig. 5.1.3*) [37].

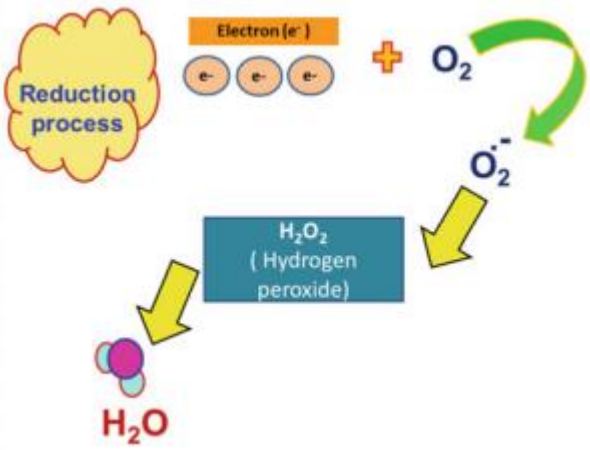


***Figure 5.1.3:*** Reduction Mechanism [37]

### 5.1.3 Advantages

Photocatalysis has several advantages, with some of them presented below [37]

- Photocatalysis offers a good replacement for the energy-intensive conventional treatment methods (adsorption on activated carbon, ultrafiltration, reverse osmosis, coagulation by chemical agents, ion exchange on synthetic adsorbent resins) with the capacity for using renewable and pollution-free solar energy.

- Photocatalysis leads to the formation of harmless products, unlike conventional treatment measures which transfer pollutants from one phase to another.

- The photocatalytic process can be used in the destruction of a variety of hazardous compounds in different wastewater streams.

- The reaction conditions for photocatalysis are mild, the reaction time is modest and a lesser chemical input is required.

- Minimal of secondary waste generation.

- It can be applied to hydrogen generation, gaseous phase, and aqueous treatments as well for solid (soil) phase treatments to some extent.

## 5.2 ZnO Catalyst

Zinc Oxide (ZnO) is one of the most analytically studied metal oxide semiconductors since it is connected with exceptional electrical, catalytic, optical, and optoelectronic properties. Because of these properties, there have been tremendous efforts on combining the physical and optical properties of ZnO with realistic applications. Following that though, it is realized over the years that ZnO is suitable for a broad range of applications such as gas sensors, piezoelectric devices, UV light detectors, energy applications (batteries, solar cells, water splitting), photocatalytic and biological purposes.

Zinc oxide is an n-type, II-VI direct gap semiconductor with a wide bandgap ($E_g$=3.37 eV) and high exciton binding energy (60 meV) at room temperature. Moreover, ZnO nanomaterials have high stability, good mechanical strength, and high electron mobility (200 $cm^2$ /Vs, in crystal form). Under these circumstances, there are, also, plenty of proposed ZnO growth geometries like nanorods, nanowires, nanobelts etc. The crystal structure of ZnO at ambient conditions is called “wurtzite” and it has a hexagonal unit cell (*fig. 5.2.1*). Specifically, the structure is composed of two interpenetrating hexagonal closed-packed sublattices, each of which consists of one type of atom (Zn or O) displaced with respect to each other along the

threefold c-axis. The ZnO structure can be described as alternating planes composed of tetrahedrally coordinated $O^{2-}$ and $Zn^{2+}$ ions, fixed alternately along the c-axis. In wurtzite structure each zinc atom is surrounded by four oxygen atoms, which are located at the corners of a nearly regular tetrahedron. Due to its structure, this material presents a strong piezoelectric effect as there is conversion from mechanical energy into electrical energy. Some of its properties, such as its crystal lattice density, melting point and lattice parameters a, c are presented in figure 5.2.1 [40], [41], [42].

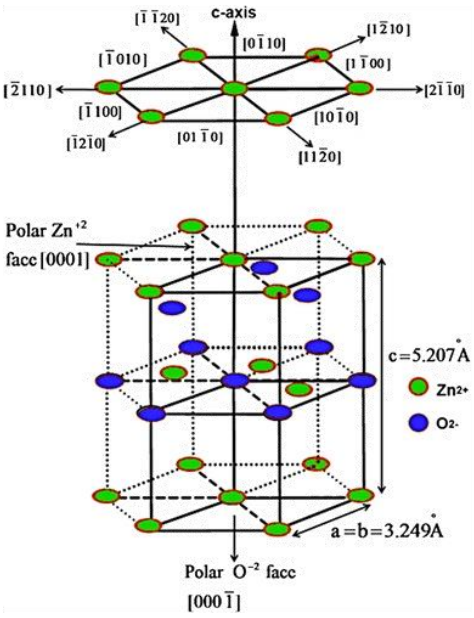


| | |
|---|---|
| *Crystal Lattice Density* | *5.67 g/cm$^3$* |
| *Melting Point* | *1975 °C* |
| *Lattice Constants a,b* | *3.249 Å* |
| *Lattice Constant c* | *5.207 Å* |

***Figure 5.2.1:*** Wurtzite Structure Of ZnO And Its Properties [42]

# 6. Metamaterials

## 6.1 Theoretical Aspects

Metamaterials are artificially structured arrangements of elements with sub-wavelength dimensions, designed to achieve advantageous and unusual electromagnetic properties. The main advantage of metamaterials comes from their designability since they extract their properties from their structure rather than the material of which they are composed. Specifically, there is a great variety of possible designs for customized dielectric properties and tunable responses. As time goes by, this new technology finds its place in more and more applications such as in telecommunication, sensing, aerospace, optics (terahertz and infrared), medical instrumentation and show great potential for application in the military and in defense. The basic unit of a metamaterial is known as a meta-atom, which is typically much smaller than the wavelength of the electromagnetic wave that the metamaterial is designed for. The unique electromagnetic properties of metamaterials are driven by the arrangement of meta-atoms in it and they can be controlled by adjusting the size, shape, orientation, and spacing of the meta-atoms, as well as the materials they are made of.

In order to characterize the electromagnetic (EM) properties of a medium, there are two fundamental parameters that need to be taken into consideration: electric permittivity (ε), and magnetic permeability (μ). Permittivity (permeability) describes how an electric or magnetic field affects, and is affected by a medium, which is determined by the ability of a material to polarize in response to this electric or magnetic field. Materials can be divided into four wide categories according to their EM properties (*fig. 6.1.1*) [43], [44], [45], [46], [47].

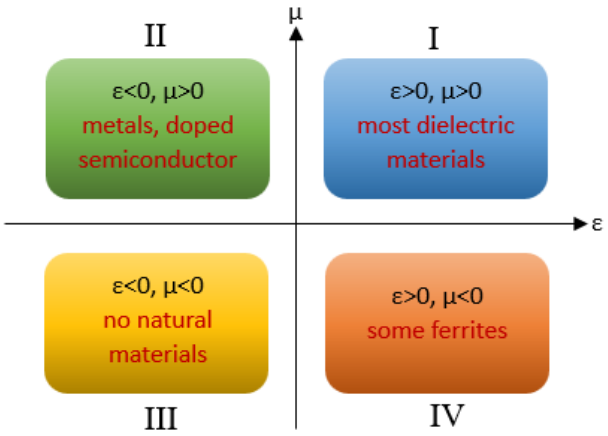


***Figure 6.1.1:*** Materials Categorized According To Their EM properties

Region I refers to materials that have simultaneously positive permittivity and permeability, which include most dielectric materials and are known as Double Positive (DPS) materials. Region II embraces metals, ferroelectric materials, and doped semiconductors that could exhibit negative permittivity at certain frequencies (below the plasma frequency) and are known as Epsilon Negative (ENG) materials. Region IV is comprised of the so-called Mu Negative (MNG) materials that include some ferrite materials with negative permeability, the magnetic responses of which, however, quickly fade away above microwave frequencies. Now, quadrant III seems to be the most interesting region in terms of EM properties since it includes Double Negative (DNG) materials. As it is shown in (fig. 6.1.1), permittivity and permeability are simultaneously negative which is a condition that cannot be found in nature. Yet, such a material possesses many remarkable properties, which were theoretically investigated in detail by physicist Victor Veselago more than forty years ago [46], [47], [49].

To gain a better understanding of this topic, let us consider a monochromatic plane wave propagating in an isotropic, homogenous medium. The electric $\vec{E}$ and magnetic $\vec{H}$ components of this plane wave will have the form

$$\vec{\mathrm{E}}\left(\boldsymbol{\omega}, \vec{\mathrm{k}}\right) = \vec{\mathrm{E}}_0 \mathrm{e}^{\mathrm{i}(\vec{\mathbf{k}}\vec{\mathbf{r}} - \omega \mathrm{t})}$$

$$\vec{\mathrm{H}}\left(\boldsymbol{\omega}, \vec{\mathrm{k}}\right) = \vec{\mathrm{H}}_0 \mathrm{e}^{\mathrm{i}(\vec{\mathbf{k}}\vec{\mathbf{r}} - \omega \mathrm{t})}$$

where ω is the angular frequency and $\vec{k}$ the wave vector. If there are no free charges (ρ) and currents ($\vec{j}$), Maxwell's equations

$$\nabla \cdot \vec{B} = 0, \nabla \times \vec{E} = -\frac{\partial \vec{B}}{\partial t}$$

$$\nabla \cdot \vec{D} = \rho, \nabla \times \vec{H} = \vec{j} + \frac{\partial \vec{D}}{\partial t}$$

and constitutive equations

$$\vec{D} = \varepsilon \vec{E} = \varepsilon_0 \varepsilon_r \vec{E}$$

$$\vec{B} = \mu \vec{H} = \mu_0 \mu_r \vec{H}$$

can be simplified into

$$k \times \vec{E} = \mu \omega \vec{H}$$

$$k \times \vec{H} = -\varepsilon \omega \vec{E}$$

Here $\vec{D}$ ($\vec{B}$) is the electric (magnetic) induction, $\varepsilon_0$ ($\mu_0$) is the permittivity (permeability) of vacuum, and $\varepsilon_r$ ($\mu_r$) is the relative permittivity (permeability) of a medium. From the simplified equations it can be seen that $\vec{k}$, $\vec{E}$ and $\vec{H}$ form a right-handed triplet of vectors, as a plane wave propagates in normal dielectric materials with $\varepsilon>0$ and $\mu>0$. In contrast, these vectors form a left-handed triplet in materials with $\varepsilon<0$ and $\mu<0$. Moreover, the Poynting vector, defined as $\vec{S} = \vec{E} \times \vec{H}$, is antiparallel to the wave vector $\vec{k}$ in such materials (*fig. 6.1.2*) [47], [48].

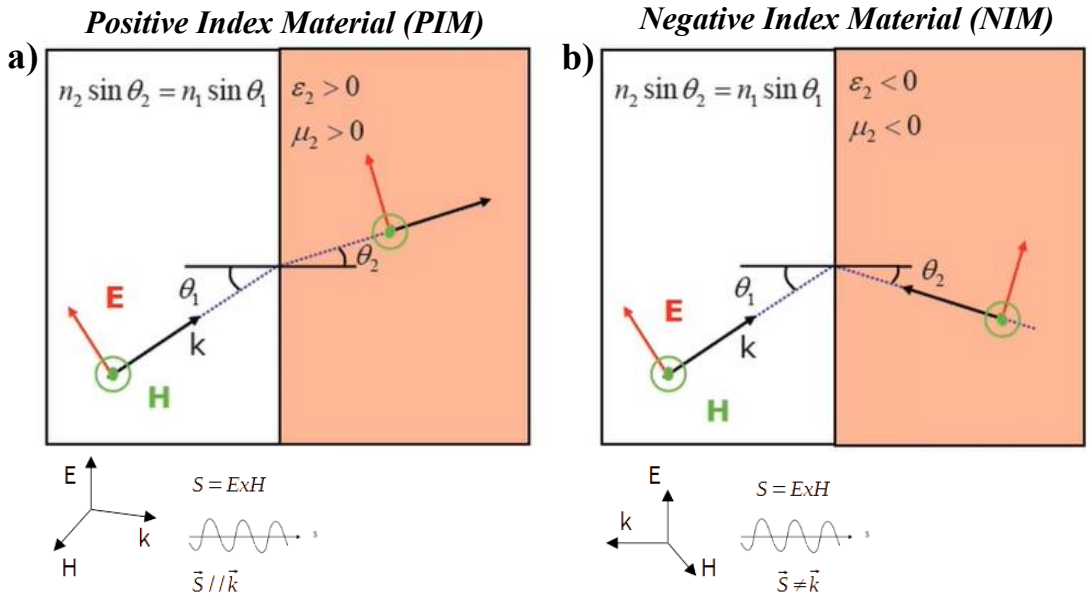


***Figure 6.1.2:*** Schematic Representation Of Refraction At a) Positive-index Material And b) Negative-index Material And The Relation Between Wave Vector ($\vec{k}$) And Poynting Vector ($\vec{S}$) In Each Case [49]

It is further proved that the phase refractive index given by

$$n = \pm\sqrt{|\varepsilon_r||\mu_r|}$$

must take a negative sign, so that the causality is still conserved. These (meta-) materials are called left-handed materials (LHMs), or negative-index materials (NIMs) due to their exotic properties. On the other hand, the materials of regions I, II, IV are known as positive-index materials (PIMs).

Negative-index materials give rise to several interesting phenomena. For example, if light is incident from a positive-index material to a negative-index one, the refracted light lies on the same side as the incident light with respect to the surface normal, because of the causality principle and conservation of tangential wave vectors. So, refracted light bends negatively at the interface (*fig. 6.1.2*). This is, also, proven by Snell's law

$$\frac{sin\theta_1}{sin\theta_2} = \frac{n_2}{n_1}$$

where it is obvious that the angle of refraction is indeed negative when the refractive indices of the two materials are opposite in signs [46], [47].

## 6.2 Designing A Metamaterial

In classical electromagnetic theory, materials properties are usually well described by the Drude–Lorentz model, which can be derived from the oscillation equation of electric charges or fictitious magnetic charges driven by an external EM wave. The frequency-dependent permittivity and permeability equations $\varepsilon_r$, $\mu_r$ follow a very similar formula due to the symmetry of EM waves

$$\varepsilon_r(\omega) = 1 - \frac{\omega_{p,e}^2}{\omega^2 - \omega_{0,e}^2 + i\gamma_e\omega}$$

$$\mu_r(\omega) = 1 - \frac{\omega_{p,m}^2}{\omega^2 - \omega_{0,m}^2 + i\gamma_m\omega}$$

The term $\omega_p$ is the plasma frequency, $\omega_0$ is the resonant frequency, and $\gamma$ is the damping factor related to material losses. The subscripts e and m represent electric and magnetic response, respectively [47], [50].

### 6.2.1 Negative Permittivity ε

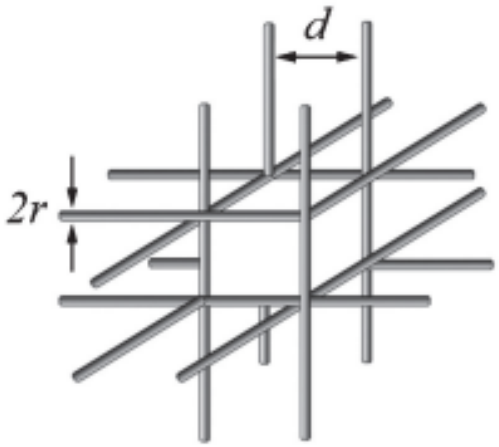


***Figure 6.2.1:*** Schematic Of Periodic Wires (with radius r) Arranged In A Simple Cubic Lattice (with lattice constant d)

By substituting proper values into the frequency-dependent permittivity and permeability equations, we have the ability to gain information about a material's properties over a wide frequency range from microwave to optical. For example, noble metals have $\omega_{p,e}$ values that are at visible or UV frequency and $\omega_{0,e}$ is taken as zero under the free electron approximation. Thus, the permittivity of metals is always negative below the plasma frequency ($\varepsilon<0$) and the first necessary requirement towards the design of metamaterials is satisfied. When operating at the plasma frequency, the effective permittivity is zero, and hence yields a zero index of refraction. This means that we can create an effective medium in order to control the permittivity ε. In 1996, Pendry et al. proposed that this effective medium could be composed of dilute metals with extremely low plasma frequency, structured into a three-dimensional (3D) lattice of very thin metallic wires (*fig. 6.2.1*). Such a structure gives rise to two effects: i) the effective electron density is apparently reduced and ii) the effective electron mass is increased because of the self-inductance of the wire structure [47], [48], [49].

### 6.2.2 Negative Permeability μ

The other necessary requirement for the design of metamaterials is the negative permeability, $\mu<0$. In optics, a bulk metal has no magnetism (uniform materials have $\mu=1$). However, in terms of magnetism, such a condition can be created by producing a current loop, like for example the orbital current in natural magnetic materials. So, instead of using a bulk metal we can shape the metal into a ring or coil. In that way, a current can be generated by a time-varying magnetic field threading through the conducting ring or coil, simply from Faraday's law. Although the induced current, and thus magnetic moment are normally weak, they can be dramatically enhanced when introducing resonances into the coil by simply cutting the ring (*fig. 6.2.2*) [47], [48].

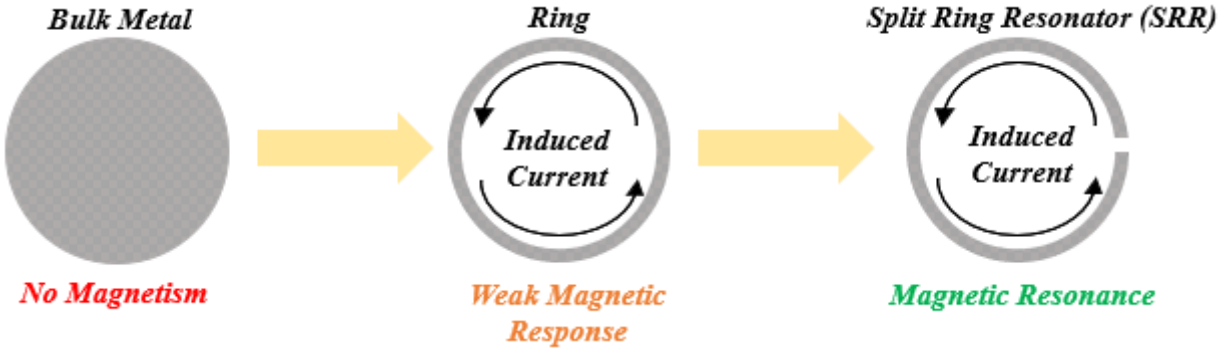


***Figure 6.2.2:*** Designing Of Materials With Magnetic Response ($\mu<0$)

Split ring resonators (SRRs) are one of the original designs for strong artificial magnetism. A typical SRR is composed of one or two ring. In the second case, the split rings are concentric with the openings at the opposite directions. The gap between inner and outer ring acts as a capacitor while the rings themselves act as an inductor. So, an SRR can be considered as an LC circuit with the natural resonant frequency given by

$$\omega_0 = \sqrt{\frac{1}{LC}}$$

with L and C denoting the geometric inductance and capacitance of the SRR structure, respectively. Within a certain frequency region centered at $\omega_0$, the magnetic flux threading through an SRR induces a strong circulating current, resulting in an effective magnetic moment. This induced magnetic moment responds in phase or out of phase with respect to the external magnetic field. If the strength of the magnetic response is sufficiently strong, effective relative magnetic permeability $\mu_{r,eff}$ with a negative value can be achieved [47], [48], [49].

### 6.2.3 Size And Shape Dependence

Another important factor that needs to be taken into consideration before the fabrication of a metamaterial is the size of the structure. According to the frequency range that the metamaterial is targeted for, a proper scaling must be done. To better understand this concept, let us take the example of a coil structure intended for metamaterial-related purposes. We know that loss in metal gives kinetic inductance. So, the total inductance, due to losses, will be given by

$$L_{tot} = L_{coil} + L_{kinetic}$$

We, also, know that

$$L_{coil} \propto size$$

$$L_{kinetic} \propto \frac{1}{size}$$

$$C_{total} \propto size$$

For the frequency at the resonance, we can calculate

$$\omega_0 \propto \sqrt{\frac{1}{L_{total}C_{total}}} = \frac{1}{\sqrt{(A \cdot size + B/size)(C \cdot size)}} \propto \frac{1}{\sqrt{size^2 + \underbrace{const.}_{Saturation}}}$$

The above equation proves that as the frequency rises, the size of the metamaterial must be reduced.

Even though the first proposed designs for strong artificial magnetism were (Double-) Split Rings, nowadays it is realized that there is a great variety of geometries that exhibit the desired EM properties of metamaterials. Hence, metamaterials can implement more sophisticated structures with some of them presented in figure 6.2.3 [49].

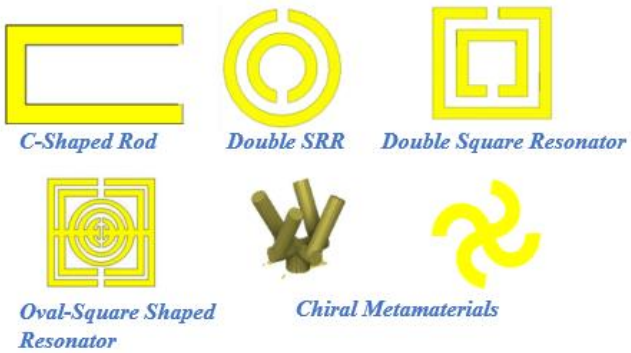


***Figure 6.2.3:*** Example Of Different Metamaterial Geometries (meta-atoms) [47], [49], [51]

# *PART II*

# *Experimental Part*

# 7. Multiple Foci Laser Writing

## 7.1 Experimental Setup

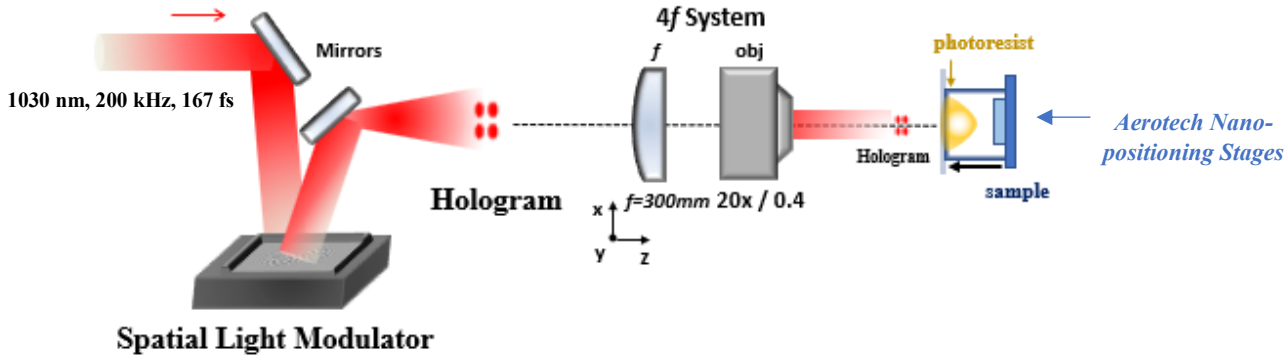


***Figure 7.1.1:*** Schematic Representation Of The Multi-Foci Laser Writing Experimental Setup

The experimental setup of the multi-foci laser writing system is depicted in figure (7.1.1). A Diode-pumped Yb:KGW PHAROS Femtosecond Laser produces a laser beam with wavelength 1030 nm, 200 kHz repetition rate and 167 fs pulse duration. Then, the fs laser beam is incident to a Hamamatsu LCOS-X10468-2 phase-only reflecting SLM, with the appropriate phase mask or hologram applied on it, and the designed distribution is generated at a specific distance. A 4f optical system composed of a f=300 mm lens and an objective lens (20×, N.A=0.4) is employed in order to further reduce in size the generated hologram in the x-y plane and target the hologram into the volume of the photoresist material (SZ2080), so that MPP is achieved. The cover glass with the drop-casted photoresist droplet is placed above the objective lens, settled in a metallic base using an Aerotech 3200, ANT95-L-Z (for z axis) and an ANT130-XY (for x-y axis) nano positioning stages system. Moreover, we have the ability to directly monitor the fabrication process using a CCD Camera.

## 7.2 Sample Preparation

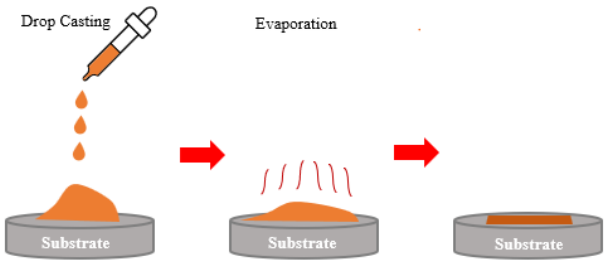


***Figure 7.2.1:*** Photoresist Preparation Process

Sample preparation starts by drop-casting photoresist droplets (SZ2080) on a cover glass, according to the surface area that needs to be covered, using a pipette. After drop-casting, the sample is placed on constant heating at a temperature of 55 °C for about an hour (~1h). In order to achieve uniform coverage, the drop-casted photoresist is spread across the substrate so that the sample is as flat as possible in its entire size. A few hours after the heating the material is ready for photopolymerization. After the photo-polymerization, the non-polymerized regions are washed out with the solvent 4-methyl-2-pentanone.

## 7.3 4-Foci Generation/3D Holographic Printing

As it is already explained in part (7.1), during the experimental part of this thesis, a LCOS phase-only reflecting Spatial Light Modulator device was employed. The main idea was to accelerate the fabrication time of complex periodic structures in photo-lithography processes by properly sculpting a laser beam. Following that scheme, we input a series of computer generated 4-foci phase masks into the SLM device. In this way, these 4-foci holograms were generated and then targeted into the volume of the photoresist material, according to process mentioned before, in order to achieve 4-foci parallel Direct Laser Writing (*fig. 7.3.1*).

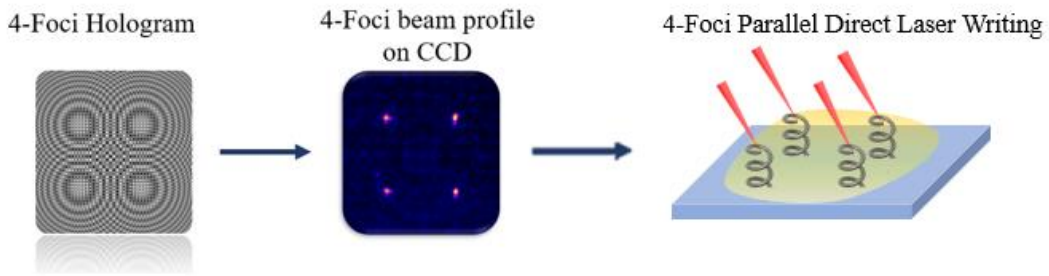


***Figure 7.3.1:*** Illustration Of The 4-Foci Parallel Direct Laser Writing (DLW)

At total, we generated eight different 4-foci holograms or phase masks. In each hologram, the distance between the 4-foci was altered. Thus, in descending order, we generated 4-foci with distances 101 μm, 56.7 μm, 39.7 μm, 34.5 μm, 28.6 μm, 22.8 μm, 17.4 μm point by point for the fabrication of 3D spiral porous periodic media (*fig. 7.3.1*) and an additional 63.5 μm 4-foci phase mask for the fabrication of 2D Periodic Split Ring Resonator (SRR) Structures, as it will be analytically explained in part (7.4.2). These measurements represent the same horizontal and vertical distance between the foci and the generated phase masks/holograms are presented below in descending order.

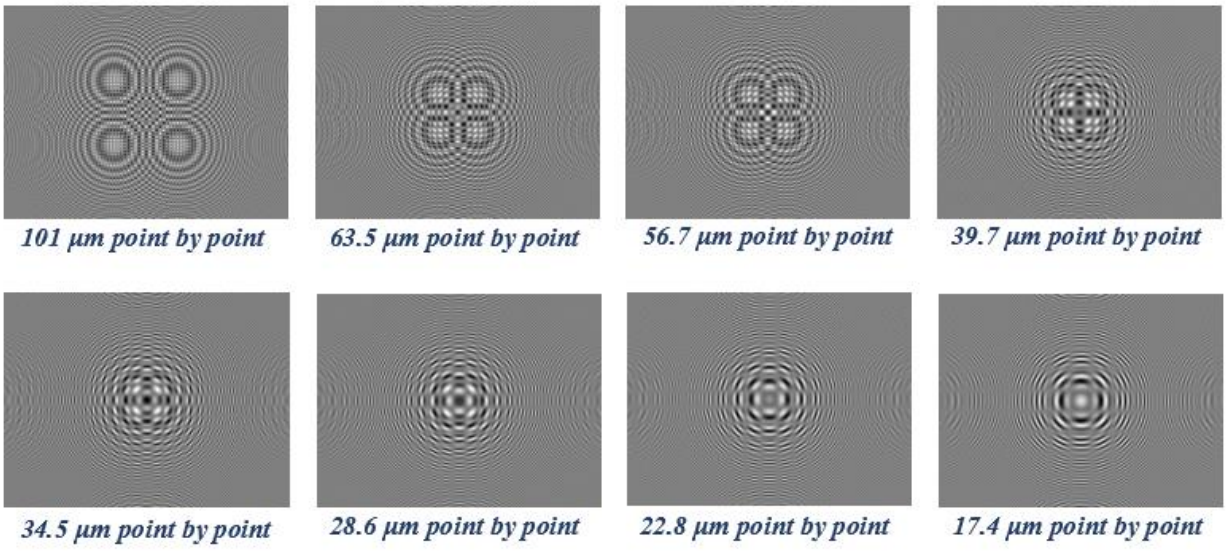


***Figure 7.3.2:*** Presentation Of The Different 4-Foci Phase Masks Used In The Fabrication Of 3D Spiral Porous Periodic Structures And 2D Periodic SRR

## 7.4 Results

After the focusing of the 4-foci hologram into the volume of the photoresist (SZ2080), we have the ability to fabricate complex periodic structures through photopolymerization. This is possible either by moving the stages, where the sample is settled, or by moving the laser beam while we keep the sample stable at a specific position. A combination of these two methods is, also, possible in order to achieve even faster fabrication. In this thesis, the movement was coordinated by a properly designed code, using a 3DPoli Fabrication Software, so that selectively polymerize each point of the material following the desired 3D model path, allowing thereby the movement on the x-y plane but along z axis, too, with parallel rotation of the sample. Moreover, in this way, there is control over the height of the structure. A depiction of the polymerization path, as shown in the 3DPoli Software, followed in the fabrication of 3D spiral porous periodic media is presented in figure (7.4.1). During fabrication, the photopolymerization path is designed so that half of the first spiral or coil overlaps with the half of the second one, half of the second spiral overlaps with the half of the third spiral, and so on. Therefore, pores are created. The height of each coil is set to be 100 μm.

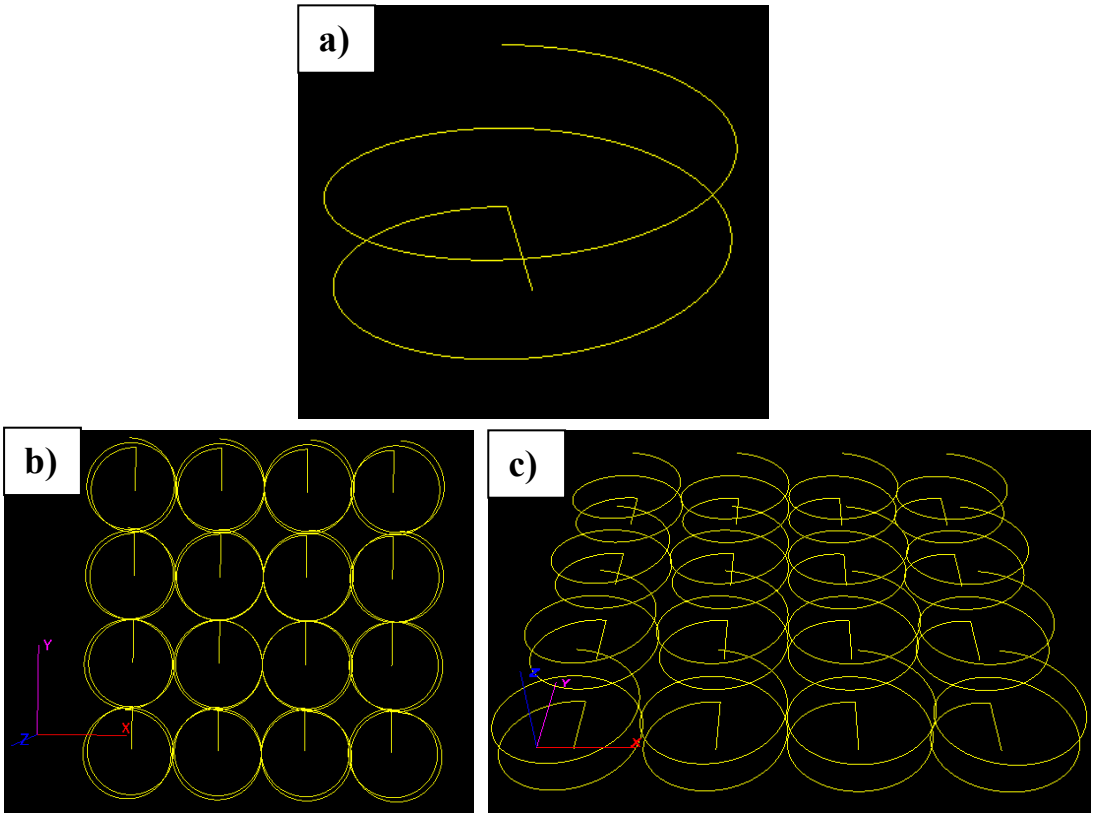


***Figure 7.4.1:*** 3D Spiral Porous Periodic Media Polymerization Path, As Shown In 3DPoli Software, For The Fabrication Of a) One Spiral Structure b, c) Multiple Spiral Structures

### 7.4.1 3D Porous Periodic Structures

By applying each one of the seven phase masks in the processing system, we managed to fabricate seven samples of 3D spiral porous periodic media with different pore sizes on the photosensitive material (SZ2080) within a few minutes, proving the efficiency of the method and its practical application. Simultaneous processing in 4 different sites into the volume of the photoresist was realized through 4-foci DLW, resulting in up to 4 times faster fabrication in comparison with conventional point by point techniques. Each focal spot (voxel) is measured to be ~2 μm wide and 14 μm long, leading to an aspect ratio of AR=1/7~0.14. All of the samples were coated with approximately 10 nm in thickness of gold (Au), using a sputter coater, in order to deposit a conductive thin film and obtain SEM images. The SEM images of these structures and their fabrication conditions are presented below.

***i) 101 μm point by point***

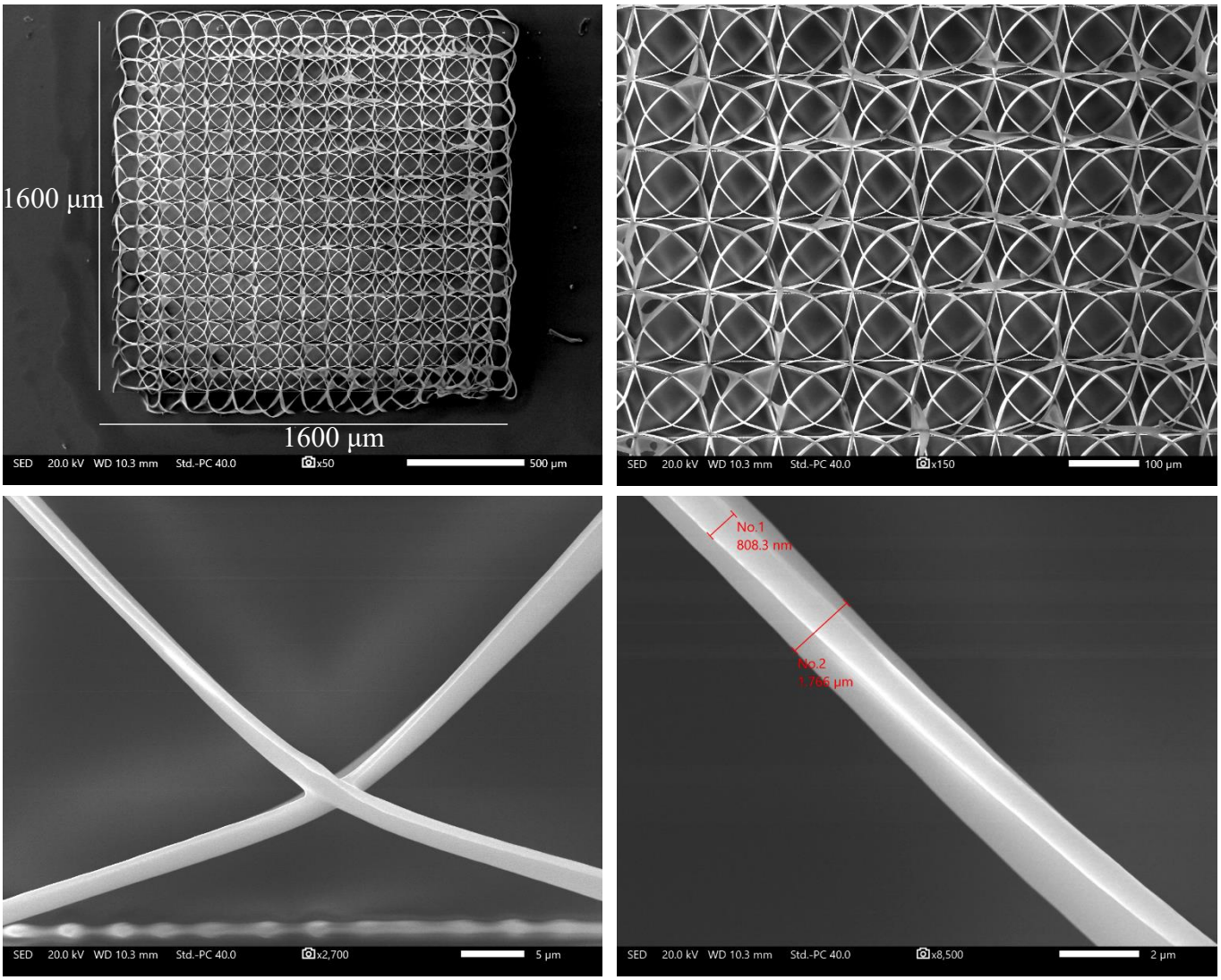


***Figure 7.4.2:*** SEM Images Of 3D Spiral Porous Periodic Structure Fabricated By 101 μm Point By Point 4-Foci Phase Mask

The 3D structure of figure (7.4.2) has an array of 16×16 spirals or coils, with a diameter of 101 µm, that overlap with each other, creating a 1600 µm × 1600 µm or 1.6 mm × 1.6 mm porous sample. The total fabrication time was 6.14 min and the total power was 110 mW or 0.550 µJ. By adjusting the fabrication velocity at 250 µm/s, we achieved a maximum writing resolution of 808.3 nm. Observing the SEM image of figure (7.4.3), it is obvious that there is a clear porosity that serves the purpose for flow in the propagation axis. The maximum pore size obtained in this structure was 70 µm while the minimum was 37 µm.

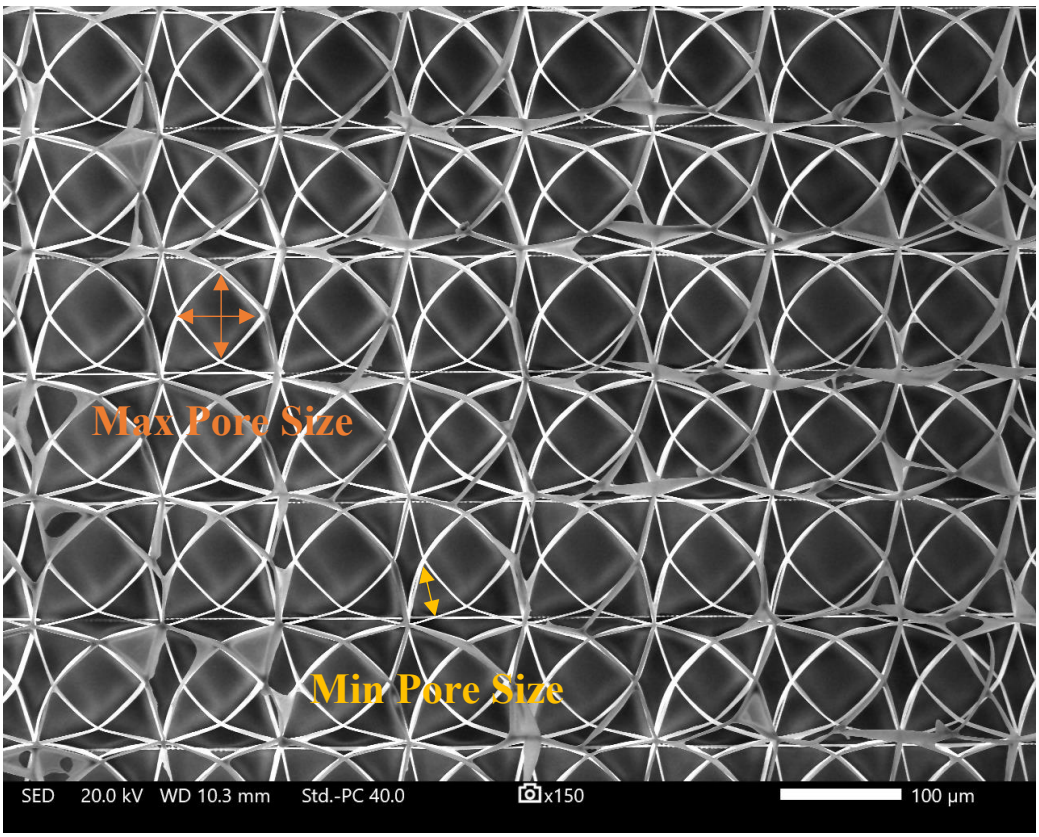


***Figure 7.4.3:*** Max And Min Pore Size Of 3D Spiral Porous Periodic Structure At 101 µm 4-Foci Phase Mask

### *ii) 56.7 µm point by point*

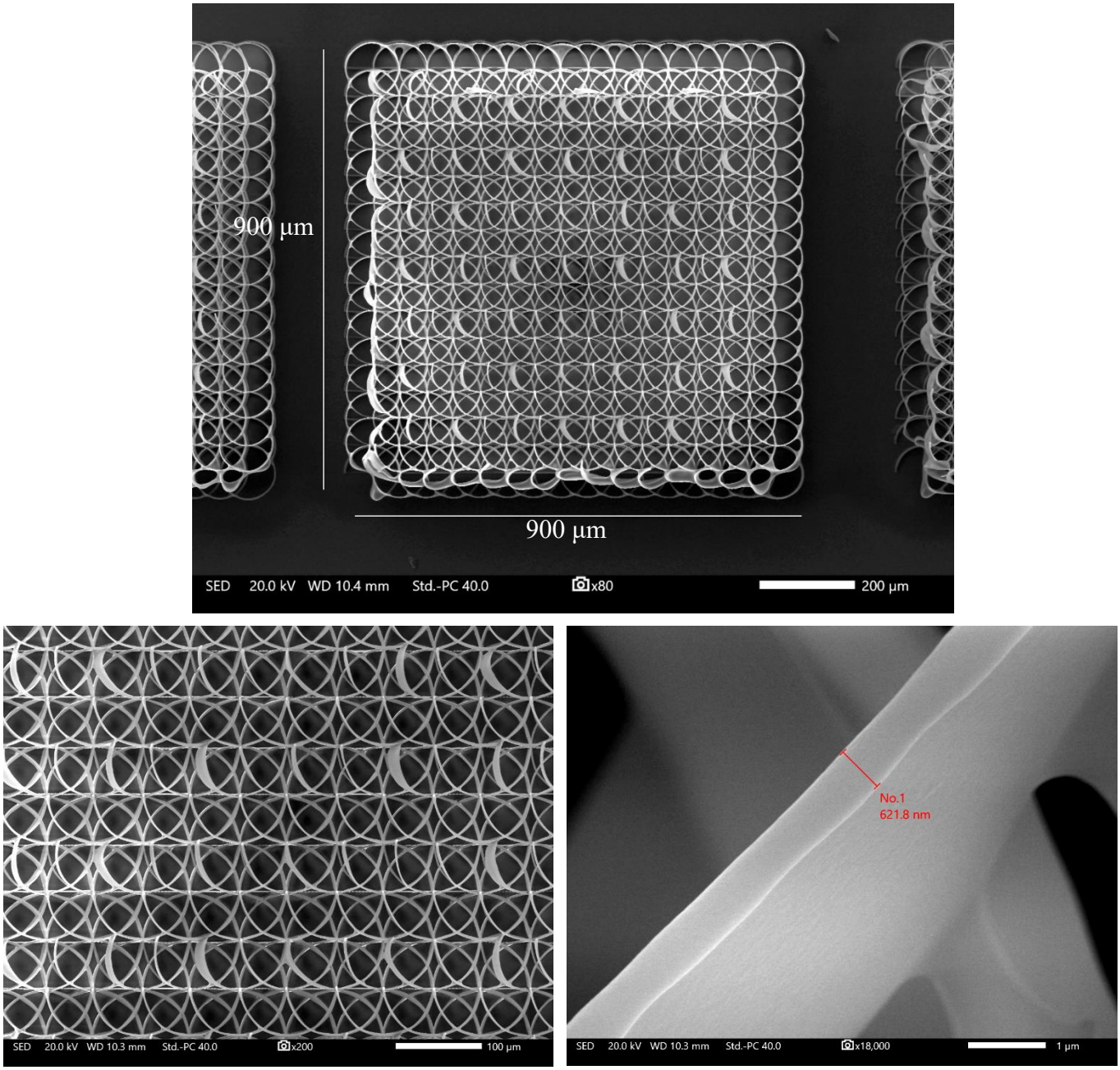


***Figure 7.4.4:*** SEM Images Of 3D Spiral Porous Periodic Structure Fabricated By 56.7 µm Point By Point 4-Foci Phase Mask

The 3D structure of figure (7.4.4) has an array of 16×16 spirals or coils, with a diameter of 56.7 µm, that overlap with each other, creating a 900 µm × 900 µm or 0.9 mm × 0.9 mm porous sample. The total fabrication time was 1.55 min and the total power was 145 mW or 0.725 µJ. By adjusting the fabrication velocity at 500 µm/s, we achieved a maximum writing resolution of 621.8 nm. Again, there is a clear porosity that serves the purpose for flow in the propagation axis. The maximum pore size obtained in this structure was 33 µm while the minimum was 20 µm (fig. 7.4.5).

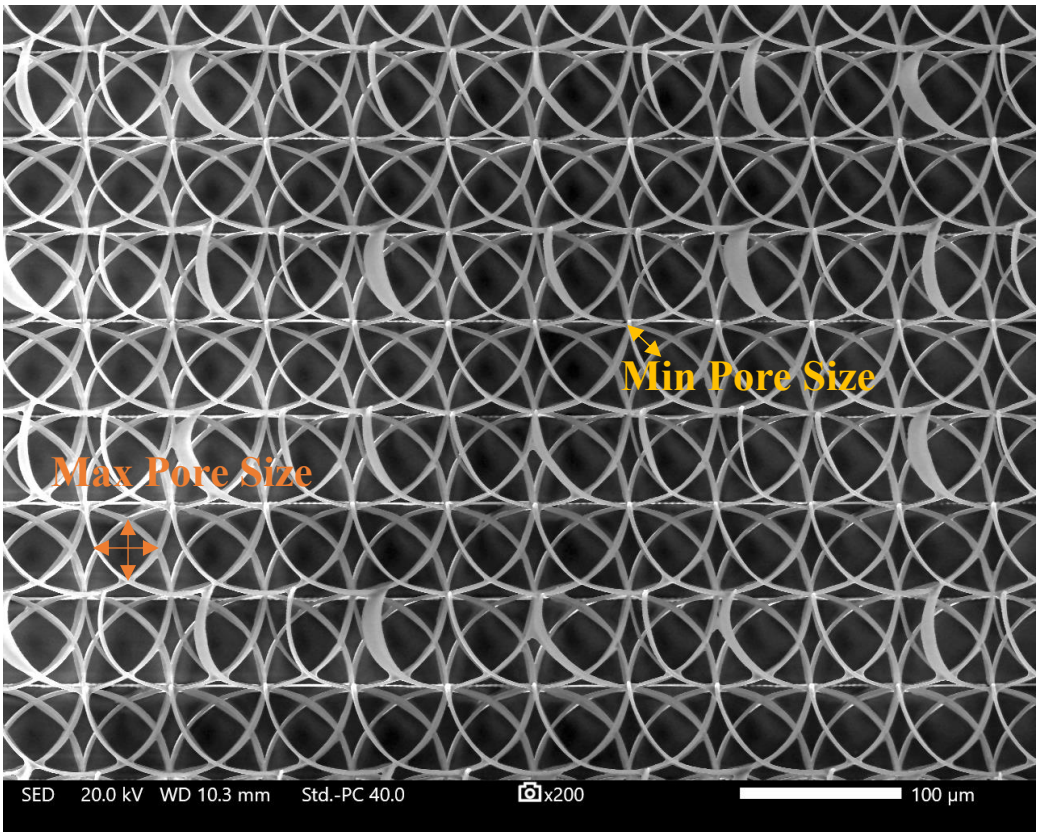


***Figure 7.4.5:*** Max And Min Pore Size Of 3D Spiral Porous Periodic Structure At 56.7 µm 4-Foci Phase Mask

### *iii) 39.7 µm point by point*

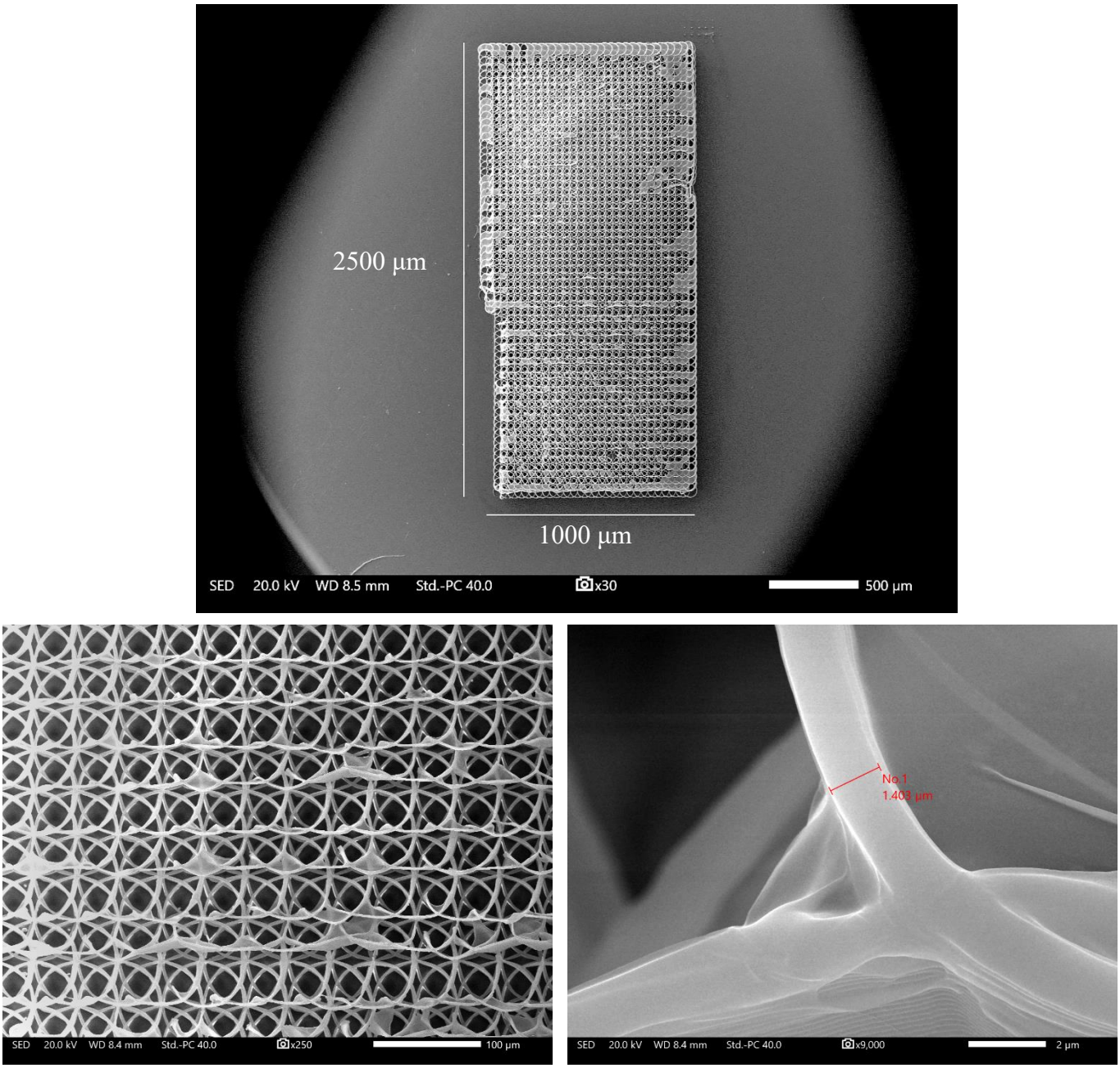


***Figure 7.4.6:*** SEM Images Of 3D Spiral Porous Periodic Structure Fabricated By 39.7 µm Point By Point 4-Foci Phase Mask

In figure (7.4.6) is depicted a 3D structure that has an array of 64×26 spirals or coils, with a diameter of 39.7 µm, that overlap with each other, creating a 2500 µm × 1000 µm or 2.5 mm × 1 mm porous sample. The total fabrication time was 15 min and the total power was 160 mW or 0.800 µJ. By adjusting the fabrication velocity at 500 µm/s, we achieved a maximum writing resolution of 1.403 µm. Once more, there is a clear porosity that assures flow in the propagation axis. The maximum pore size obtained in this structure was 22 µm while the minimum was 11 µm (fig. 7.4.7).

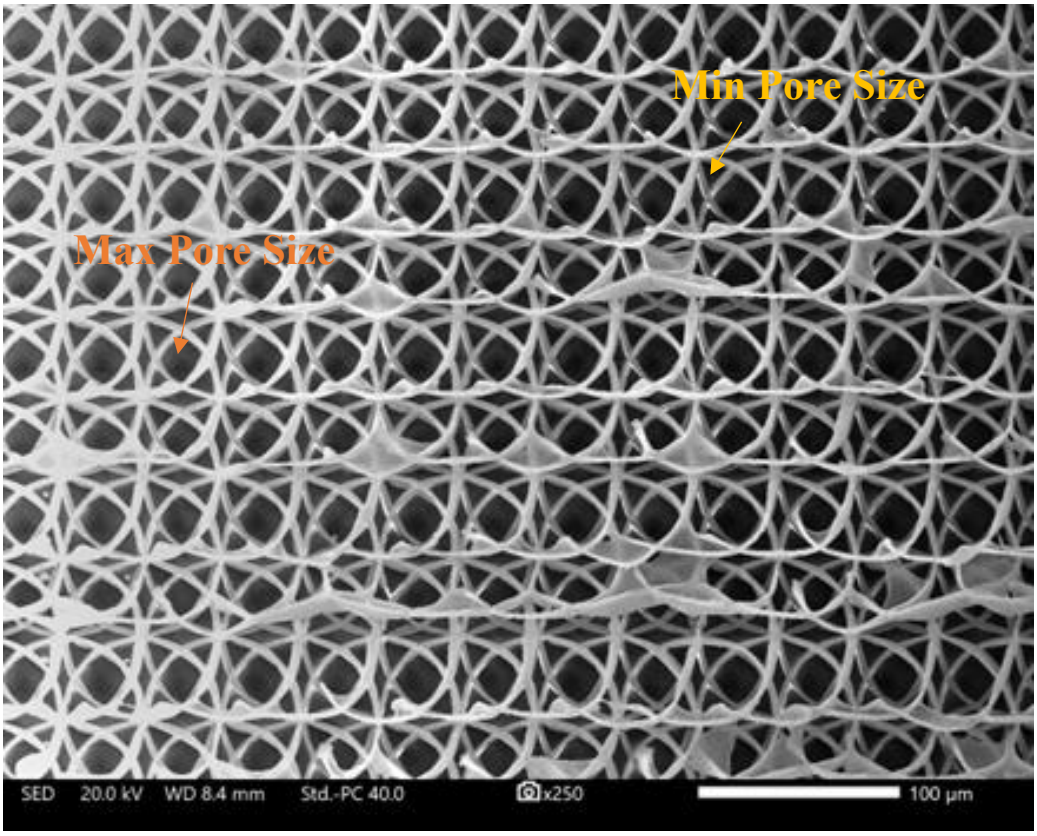


***Figure 7.4.7:*** Max And Min Pore Size Of 3D Spiral Porous Periodic Structure At 39.7 µm 4-Foci Phase Mask

### *iv) 34.5 µm point by point*

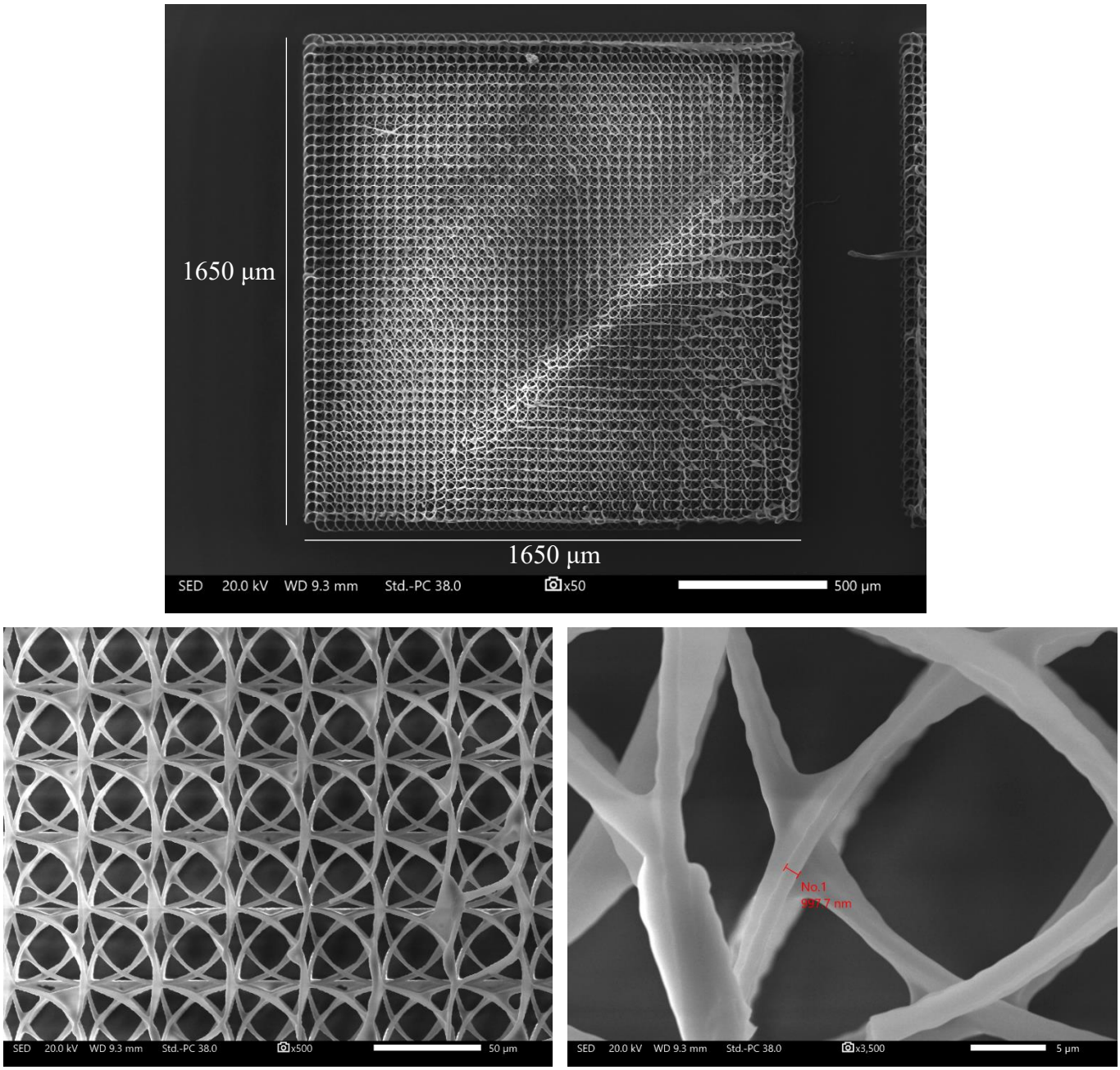


***Figure 7.4.8:*** SEM Images Of 3D Spiral Porous Periodic Structure Fabricated By 34.5 µm Point By Point 4-Foci Phase Mask

The 3D structure of figure (7.4.8) has an array of 48×48 spirals or coils, with a diameter of 34.5 µm, that overlap with each other, creating a 1650 µm × 1650 µm or 1.65 mm × 1.65 mm porous sample. The total fabrication time was 11.16 min and the total power was 129 mW or 0.645 µJ. By adjusting the fabrication velocity at 500 µm/s, we achieved a maximum writing resolution of 997.7 nm. The SEM images reveal that there is a clear porosity that assures flow in the propagation axis. The maximum pore size obtained in this structure was 19 µm while the minimum was 10 µm (fig. 7.4.9).

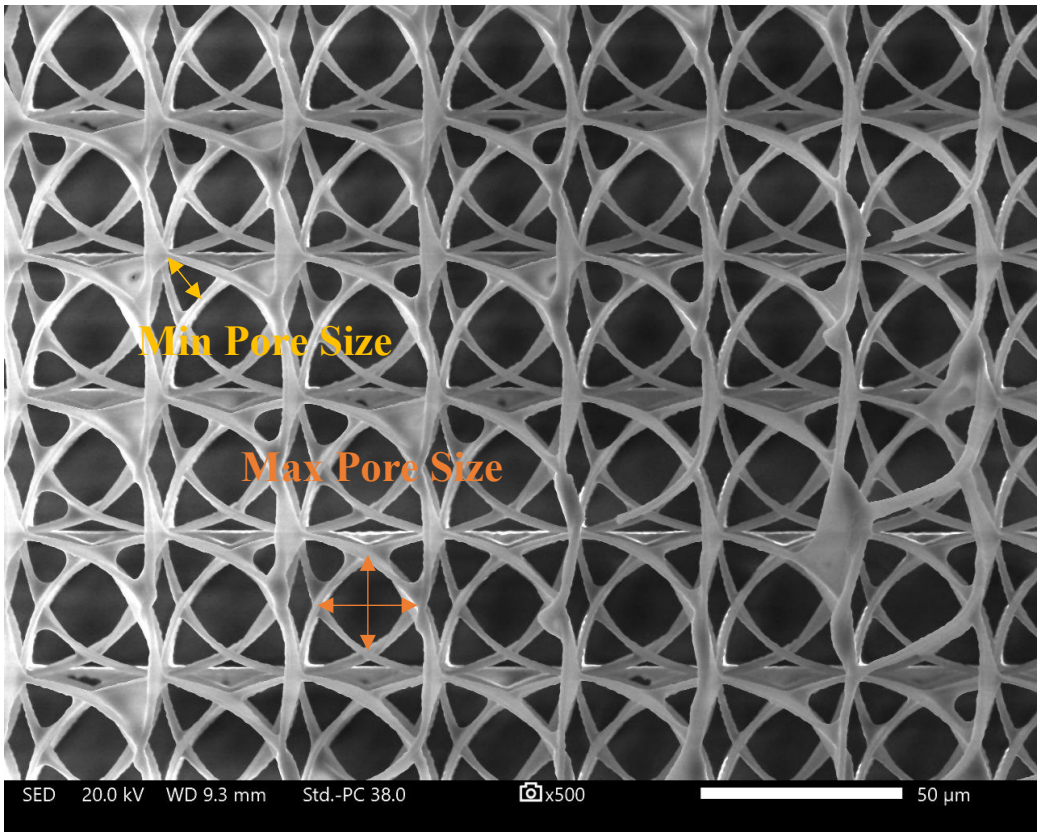


***Figure 7.4.9:*** Max And Min Pore Size Of 3D Spiral Porous Periodic Structure At 34.5 µm 4-Foci Phase Mask

### *v) 28.6 µm point by point*

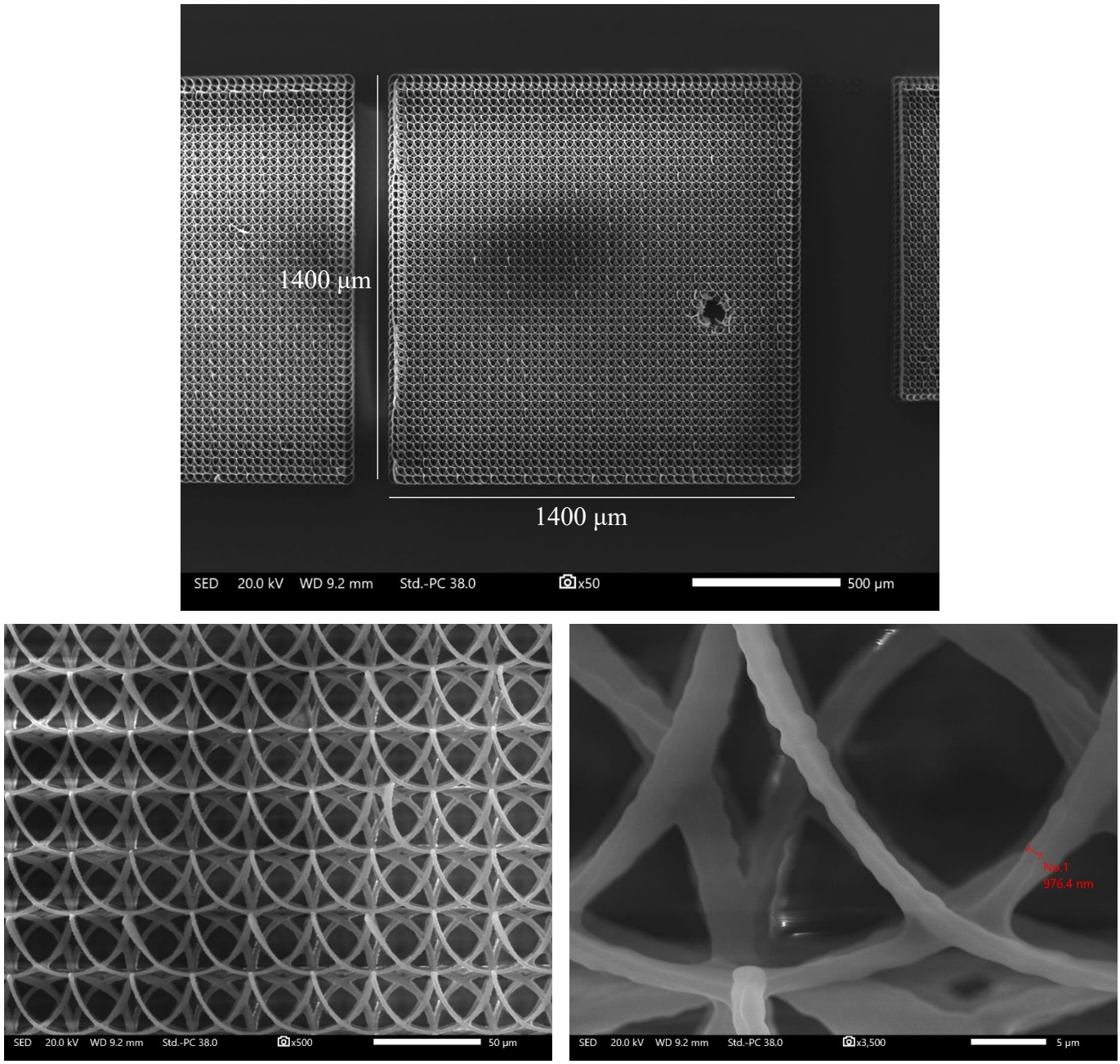


***Figure 7.4.10:*** SEM Images Of 3D Spiral Porous Periodic Structure Fabricated By 28.6 µm Point By Point 4-Foci Phase Mask

The 3D structure of figure (7.4.10) has an array of 48×48 spirals or coils, with a diameter of 28.6 µm, that overlap with each other, creating a 1400 µm × 1400 µm or 1.4 mm × 1.4 mm porous sample. The total fabrication time was 9.36 min and the total power was 135 mW or 0.675 µJ. By adjusting the fabrication velocity at 500 µm/s, we achieved a maximum writing resolution of 976.4 nm. The SEM images reveal that there is a clear porosity that serves the purpose for flow in the propagation axis. The maximum pore size obtained in this structure was 15 µm while the minimum was 7 µm (fig. 7.4.11).

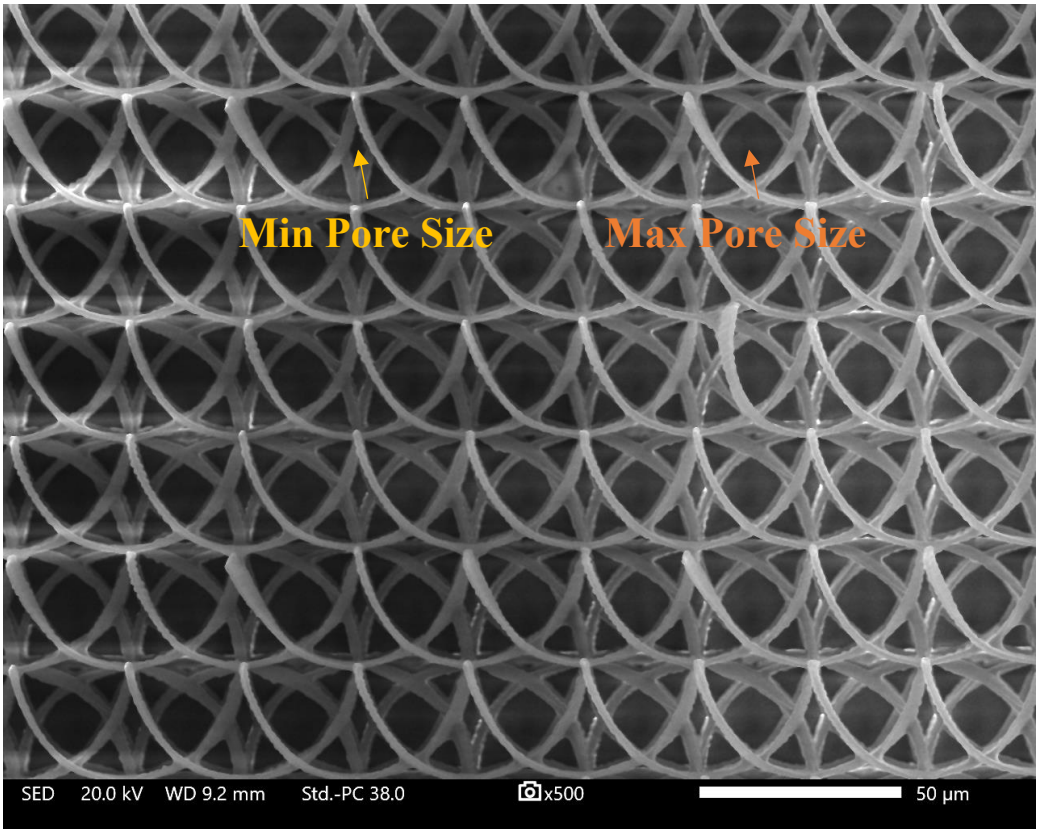


***Figure 7.4.11:*** Max And Min Pore Size Of 3D Spiral Porous Periodic Structure At 28.6 µm 4-Foci Phase Mask

***vi) 22.8 µm point by point***

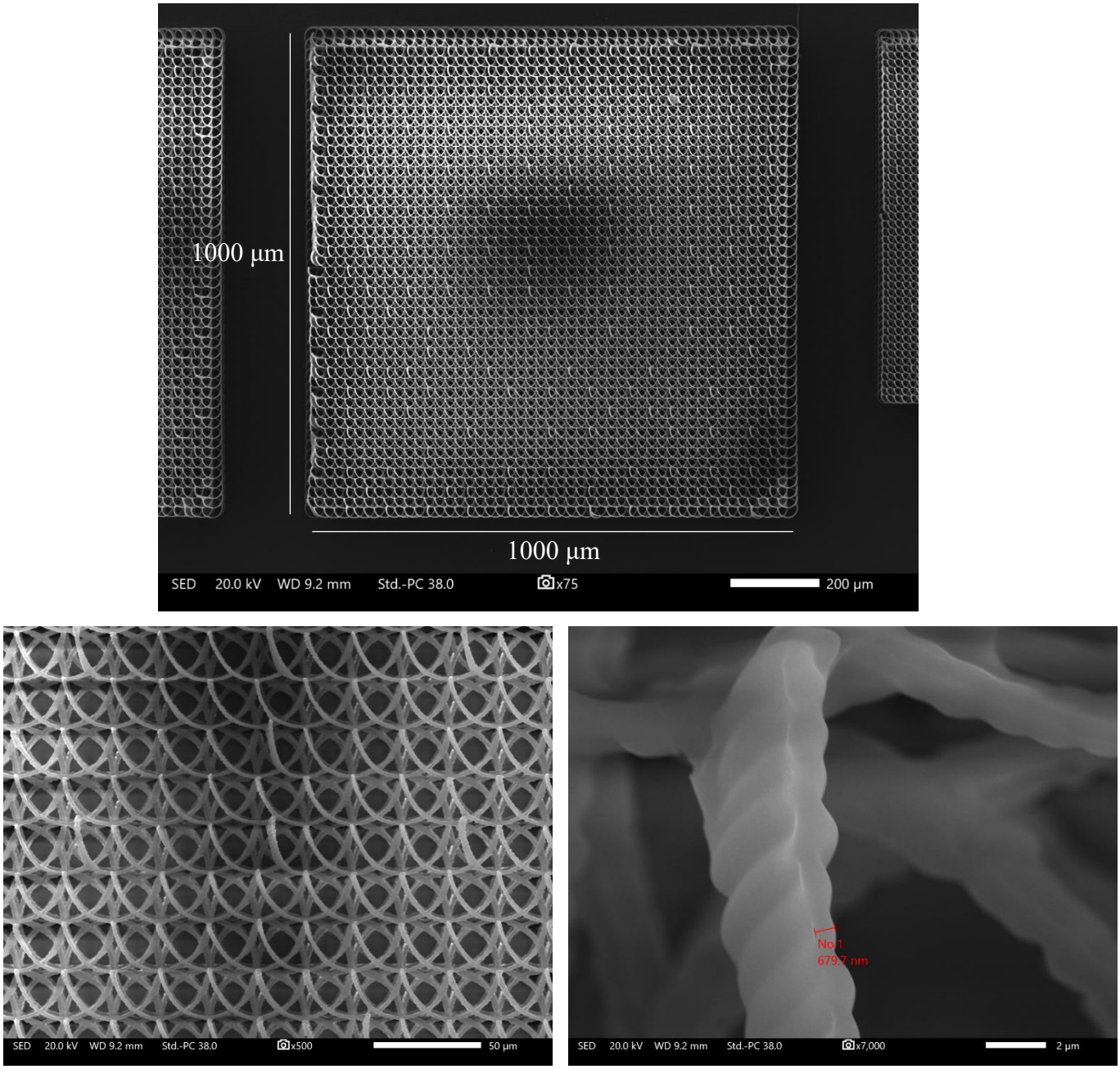


***Figure 7.4.12:*** SEM Images Of 3D Spiral Porous Periodic Structure Fabricated By 22.8 µm Point By Point 4-Foci Phase Mask

In figure (7.4.12) is depicted a 3D structure that has an array of 48×48 spirals or coils, with a diameter of 22.8 µm, that overlap with each other, creating a 1000 µm × 1000 µm or 1 mm × 1 mm porous sample. The total fabrication time was 7.59 min and the total power was 138 mW or 0.690 µJ. By adjusting the fabrication velocity at 500 µm/s, we achieved a maximum writing resolution of 679.7 nm. In this sample, there is, also, a clear porosity that assures flow in the propagation axis. The maximum pore size obtained in this structure was 11 µm while the minimum was 5 µm (fig. 7.4.13).

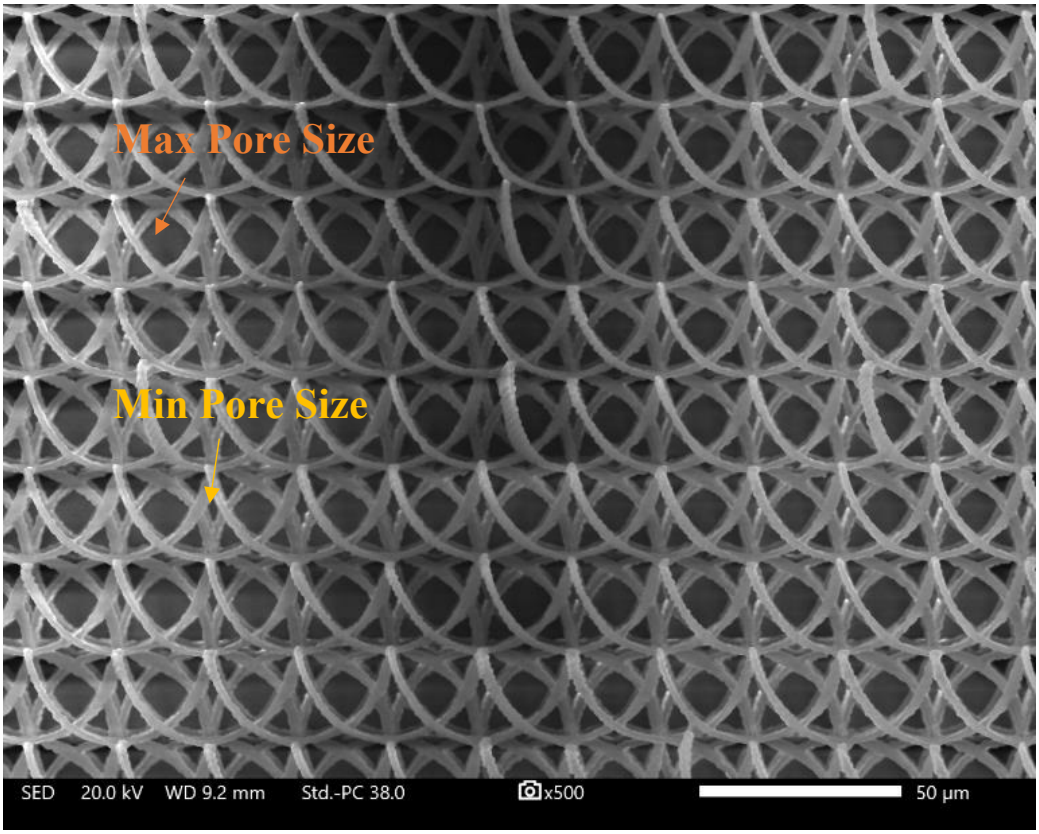


***Figure 7.4.13:*** Max And Min Pore Size Of 3D Spiral Porous Periodic Structure At 22.8 µm 4-Foci Phase Mask

***vii) 17.4 µm point by point***

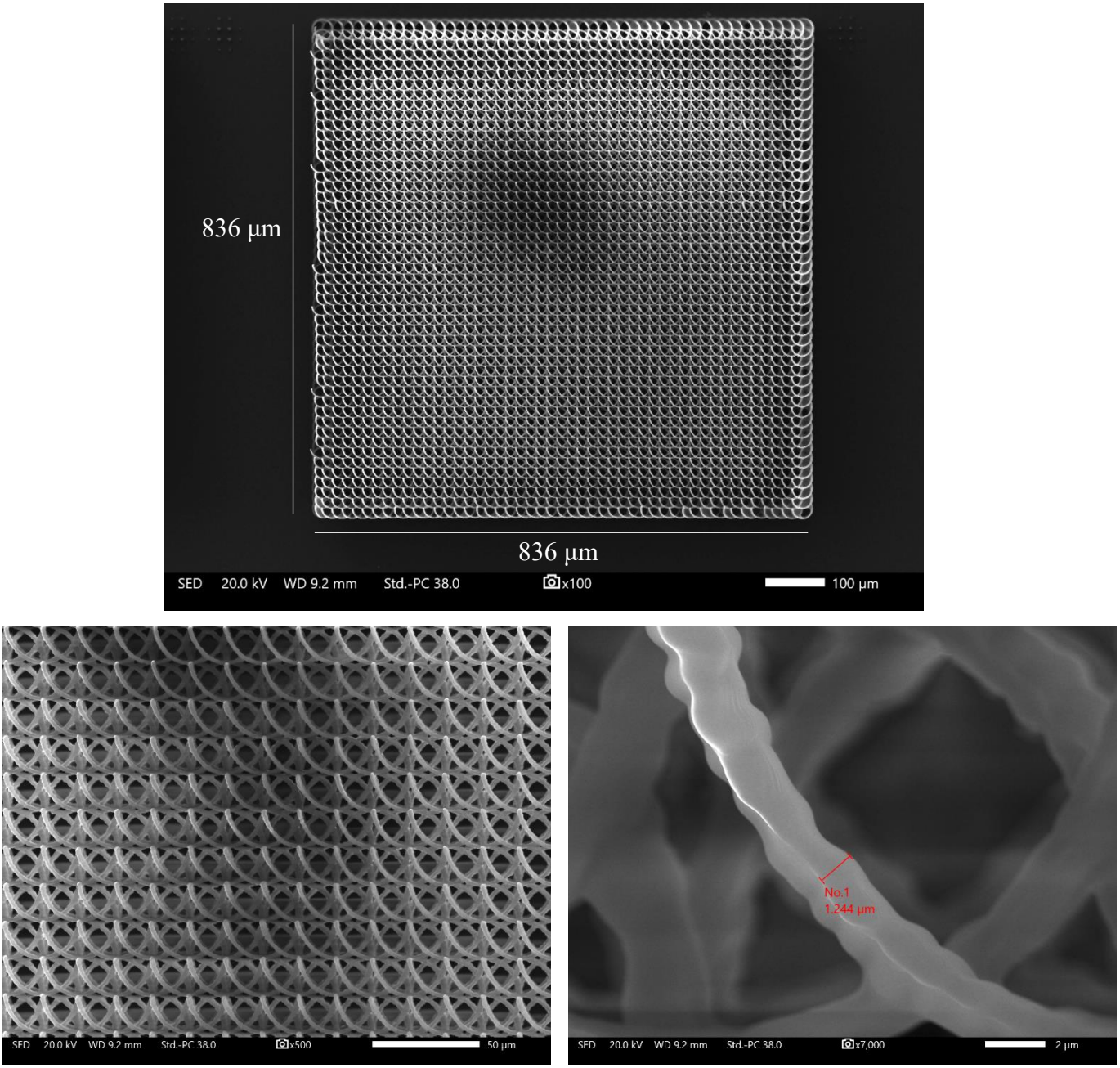


***Figure 7.4.14:*** SEM Images Of 3D Spiral Porous Periodic Structure Fabricated By 17.4 µm Point By Point 4-Foci Phase Mask

The 3D structure of figure (7.4.14) has an array of 48×48 spirals or coils, with a diameter of 17.4 µm, that overlap with each other, creating an 836 µm × 836 µm or 0.836 mm × 0.836 mm porous sample. The total fabrication time was 6.31 min and the total power was 140 mW or 0.700 µJ. By adjusting the fabrication velocity at 500 µm/s, we achieved a maximum writing resolution of 1.244 µm. The SEM images reveal that there is a clear porosity that serves the purpose for flow in the propagation axis. The maximum pore size obtained in this structure was 8 µm while the minimum was 3 µm (*fig. 7.4.15*).

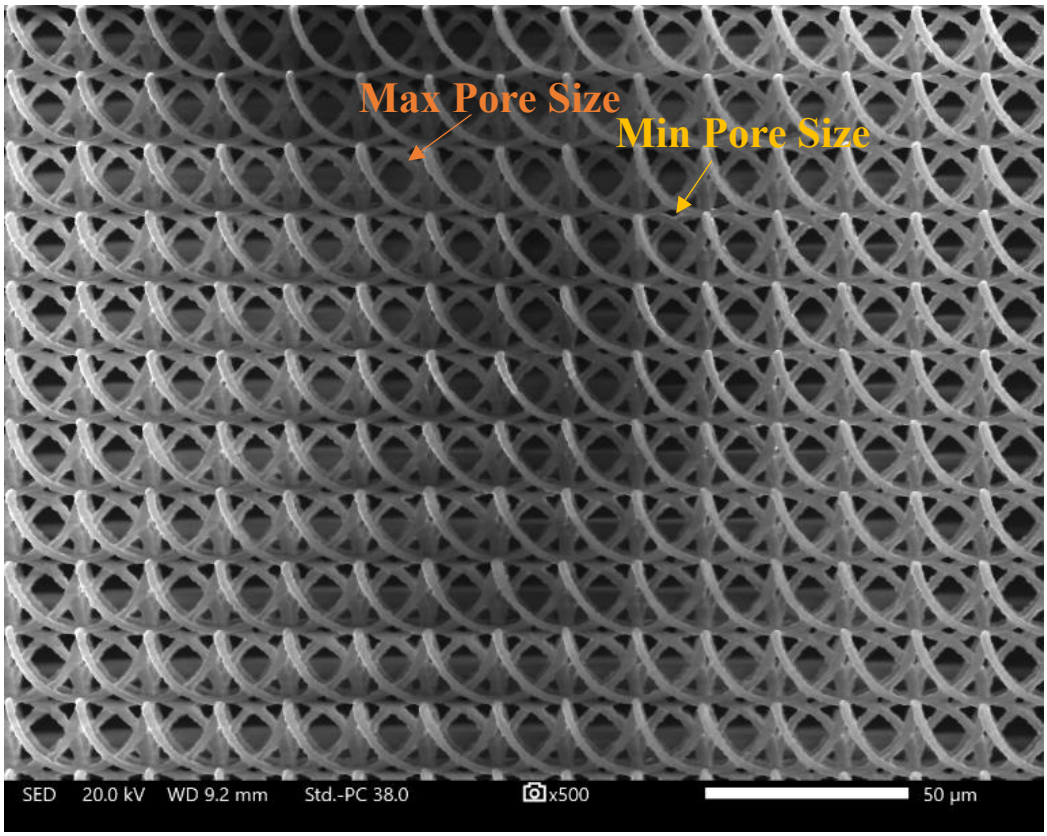


***Figure 7.4.15:*** Max And Min Pore Size Of 3D Spiral Porous Periodic Structure At 17.4 µm 4-Foci Phase Mask

The comparison of the results from the fabricated structures (i)-(vii), reveals that there is the ability to directly produce a variety of porous media in micro- and millimeter scales within a few minutes time range, using multi-foci parallel processing, by dynamically adjusting the distance between the multiple foci through the SLM. Specifically, these complex periodic media have micro-featured porosity. The pores of the fabricated media have a range that varies between approximately 70 µm (maximum value) and 3 µm (minimum value) while the maximum structure size obtained is 1600 µm × 1600 µm for the structure (i) within 6.14 min and the minimum size obtained is 836 µm × 836 µm for the structure (vii) within 6.31 min. Observations of the 3D structures through the side view (cross-section) provide more information about their characteristics. As it is presented in figure (7.4.16), the height of the porous media is approximately 100 µm, following the code-designed height specifications. In addition, it is clear that these media exhibit high resolution features due to the well-defined localization of the energy distribution and the desired geometry is indeed followed in z-axis under the designed 3D photopolymerization path. Hence, the coils overlap along z-axis creating the pores.

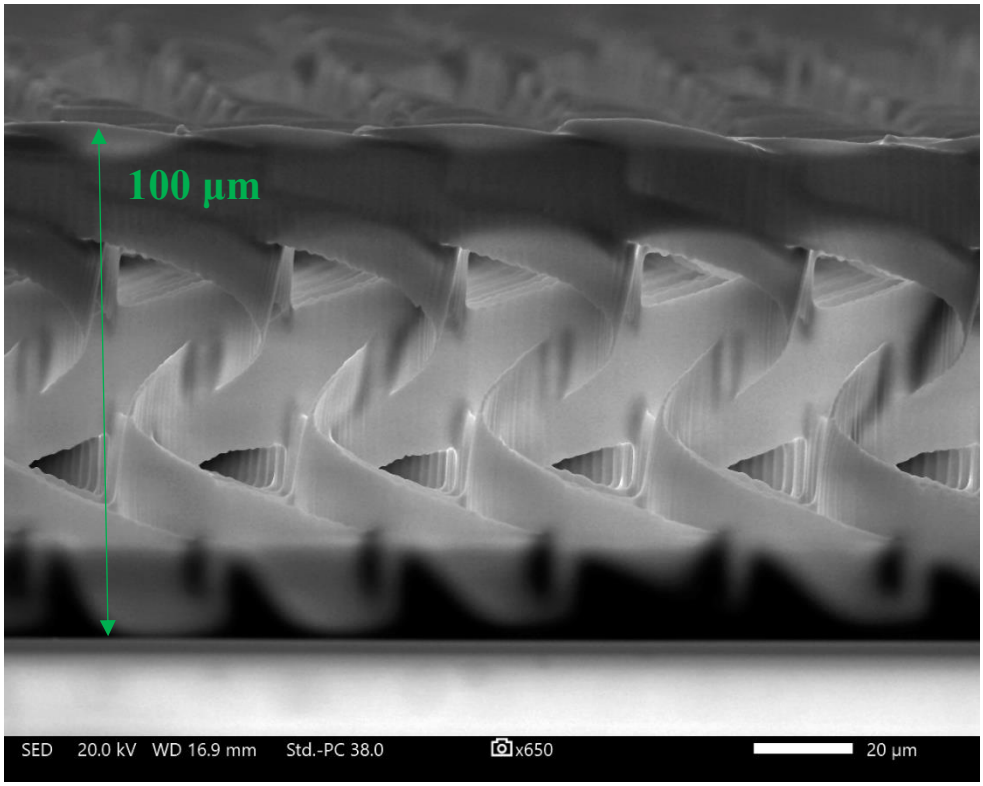


***Figure 7.4.16:*** SEM Image Of The Side View Of A Typical 4-Foci Fabricated 3D Porous Medium

A complete comparison of the maximum and minimum pore's size values, obtained through the adjustment of the point-by-point distance on the 4-foci masks, is presented in figure (7.4.17).

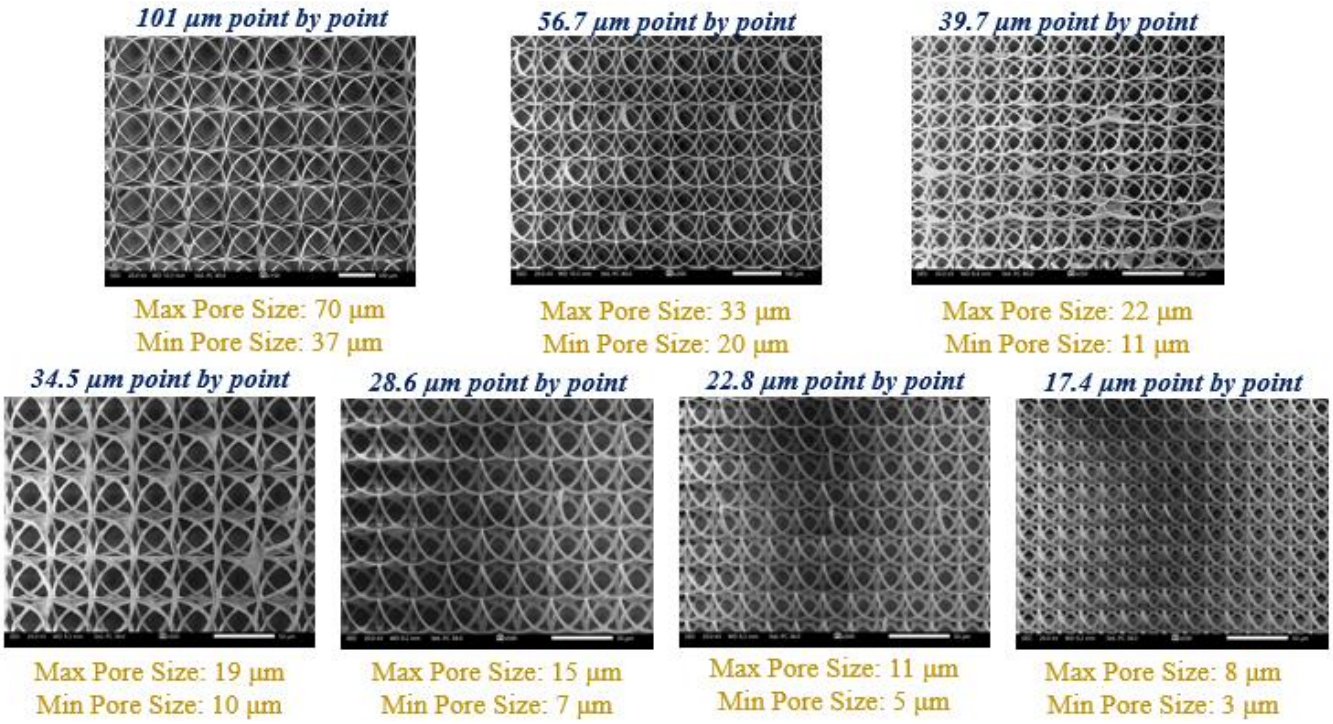


***Figure 7.4.17:*** Total Range OF Max And Min Pore Size Of 3D Spiral Porous Periodic Structure Fabricated By 4-Foci Phase Mask

## 7.4.2 Optimization Of Beam Shaping

In a previous study conducted by our laboratory, we explored the ability of Multibeam Interference lithography to be employed as a fabrication technique able to accelerate the production of complex 3D periodic structures. Multibeam interference involves the superposition of multiple ($\geq$ 2) optical waves, coexisting in the same spatial region, resulting in the generation of a periodic spatial modulation of light. By employing multiple overlapping beams, an interference pattern with an intensity periodicity akin to the desired structure can be achieved. While the outcomes of this approach exhibited promising results, the fabrication time obtained was still significantly longer than our intended target. Consequently, in the scheme of exploring alternative techniques, we turned our attention to the utilization of 3D Holographic Printing to address this challenge [52], [53].

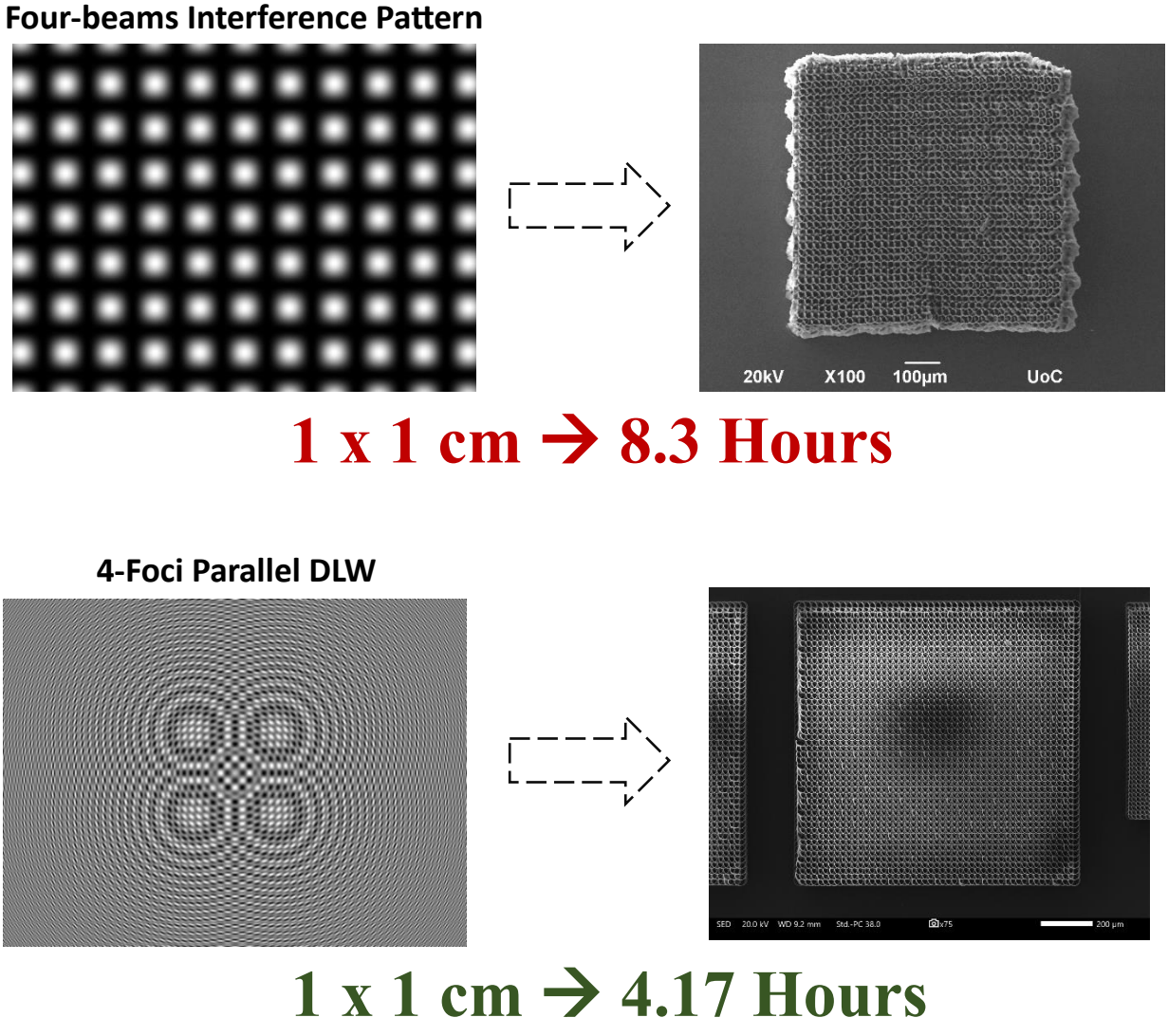


***Figure 7.4.18:*** Comparison Of The Fabrication Time Of The Same 1 mm x 1 mm Structures Scaled-Up To 1 cm x 1 cm Using Two-Different Writing Methods a) Multibeam Interference Lithography b) 4-Foci Parallel DLW

Despite the ability of multibeam interference for parallel coverage of a wide surface area in the photoresist during processing, its implementation results in significant challenges due to the energy dispersion across multiple spots (in our study, up to $10^2$ spots). Specifically, this dispersion necessitates to increase the exposure of the photoresist in each focal spot, resulting in a reduction of printing speed. Therefore, the fabrication time is extended, leading to high overall processing times. In contrast, 3D holographic printing, specifically the 4-foci DLW (Direct Laser Writing) technique employed in this thesis, ensures a precise energy distribution across the multiple spots. This enhanced control over energy distribution enables higher printing speeds, as the exposure process becomes more efficient and polymerization is accelerated. As a result, 3D holographic printing demonstrates improved performance in terms of both speed and effectiveness compared to multibeam interference lithography. This is experimentally supported by comparing the scaled-up version of the same 3D Porous Structure, in terms of fabrication time, for the two distinct methods (*fig.7.4.18*). Based on our calculations, it has been determined that the fabrication time for a scaled-up version of a 1 mm x 1 mm 3D porous structure into 1 cm x 1 cm, using multibeam interference lithography, would require approximately 8 hours and 30 minutes. However, by employing the 4-foci parallel DLW technique in 3D holographic printing, the same structure can be scaled up to 1 cm x 1 cm in only 4 hours and 17 minutes. Additionally, the resolution of the structure achieved through the 4-foci parallel DLW method is significantly improved compared to multibeam interference lithography. These findings clearly demonstrate the effective reduction in fabrication time and the enhanced resolution of structures through the utilization of 3D holographic printing.

### 7.4.3 2D Split Ring Resonators Through Parallel Ablation

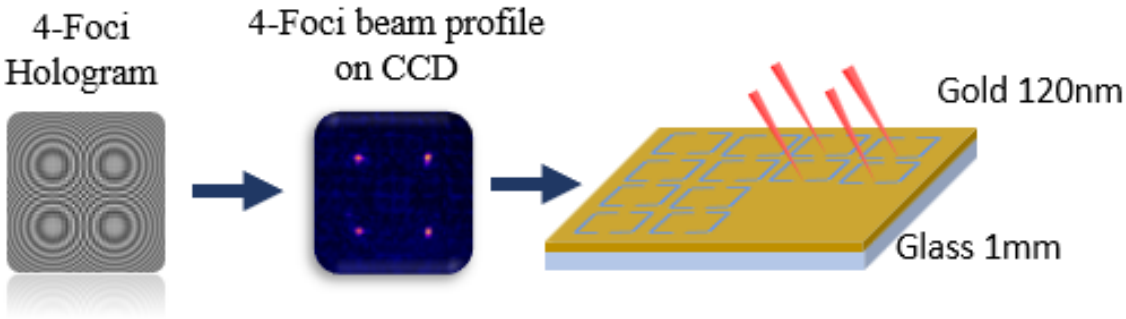


***Figure 7.4.19:*** Illustration Of The 4-Foci Parallel Ablation On Thin Gold Film

Multi-foci fabrication method is not limited only on photopolymerization processes. Instead, it can be used as an alternative method on ablation assisted fabrication. This idea was adopted for the designing of a desired Split Ring Resonators (SRR) structure on top of a gold substrate. Such SSR structures were engraved by parallel 4-foci gold ablation on top of a 1 mm thick glass covered with a 120 mm thick gold film, deposited by sputtering (*fig. 7.4.19*). These SRRs are designed so that they follow the Babinet's principle, which states that an opaque body would exhibit the same properties with an identical one, designed from a hole of the same size and shape, or explaining it in a more practical way, the shape of the structure is not built on the top of the substrate but carved out of the metal by removing the gold with laser ablation. Again, the fabrication was assisted by 3DPoli software so that the 4-foci beam follow the defined ablation path.

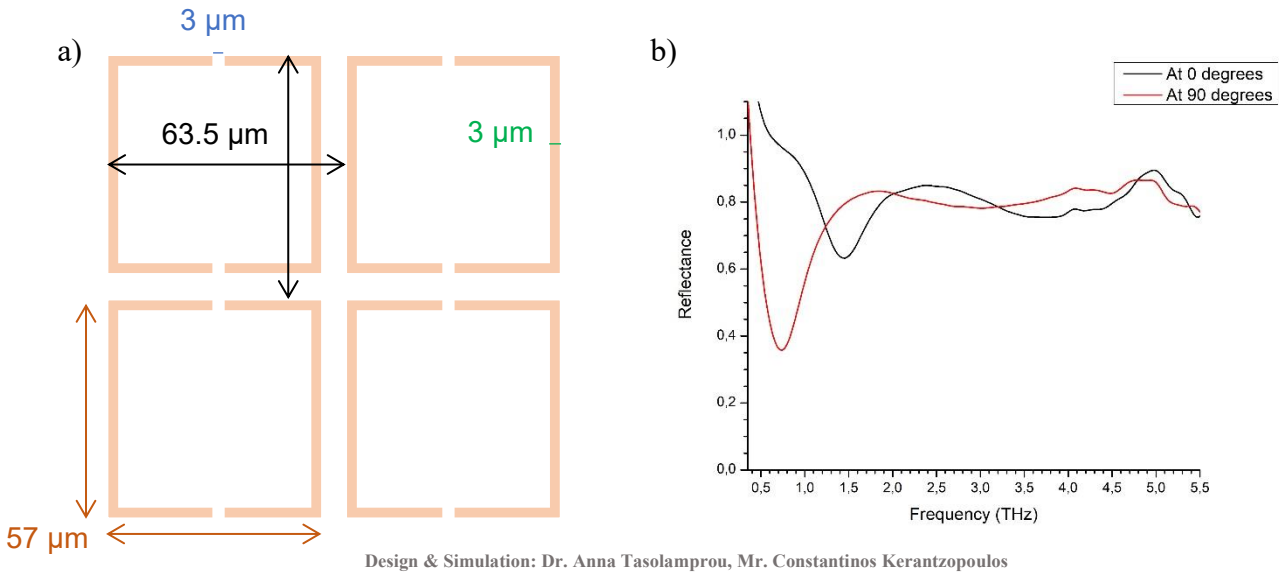


***Figure 7.4.20:*** a) Computer Simulated Periodic SRR Structure And b) Its Simulated Resonance Spectrum At Two Different Polarizations, i.e., 0 and 90 degrees

In figure 7.4.20, the computer simulated periodic SRR structure and its simulated resonance spectrum are depicted. Each SRR or meta-atom consists of four sides with length 57 μm and each side along the y-axis has a gap of 3 μm. The width of a single side is equal to 3 μm and the distance between the SRRs is designed to be 6.5 μm, creating a periodicity of 63.5 μm. Simulation for this design showed that it is expected to exhibit resonance frequency at 0.6 THz when the polarization is set at 90 degrees while the resonance frequency is expected to be 1.5 THz when the polarization is set to 0 degrees.

So, by applying a 4-foci phase mask with distance 63.5 μm point by point, we managed to fabricate a periodic structure that consists of 65×65 Split Ring Resonators (SRR) and covers a surface of ~ 4.7 mm × 4.7 mm (*fig. 7.4.21*). The total fabrication time for this structure was ~ 45 min.

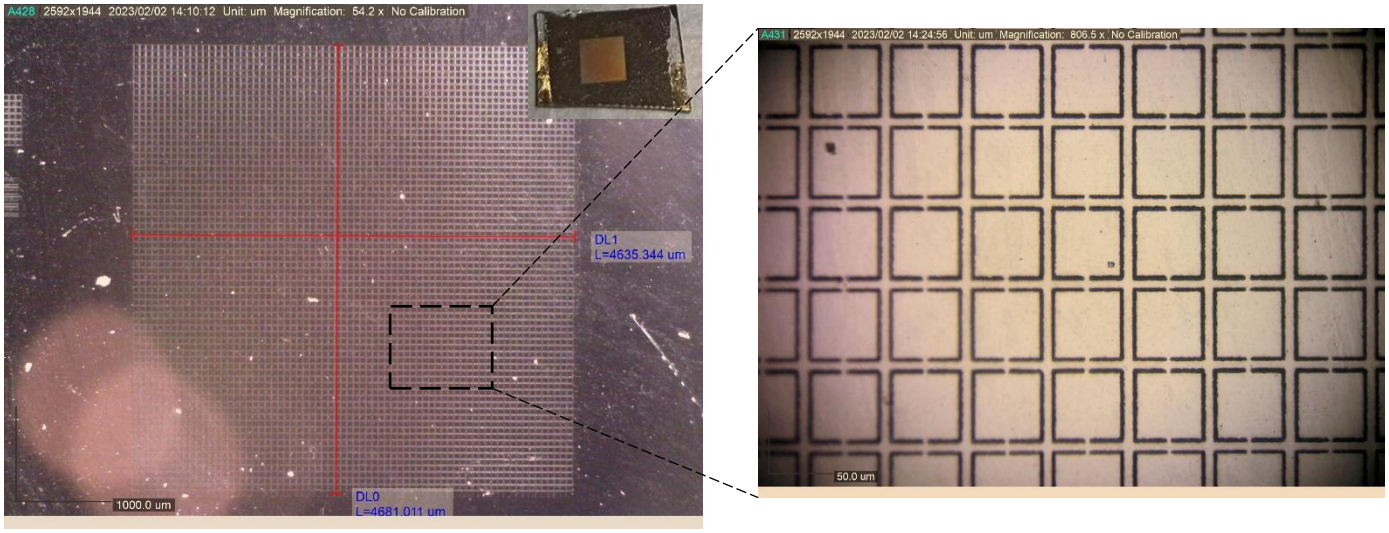


***Figure 7.4.21:*** 4-Foci Fabricated SRR Periodic Structure Through Ablation On Gold Thin Film Under Microscope

To further evaluate our results and the efficiency of the method, SEM images and EDS graphs were obtained. The results are displayed in figures (7.4.22), (7.4.23) and (7.4.24).

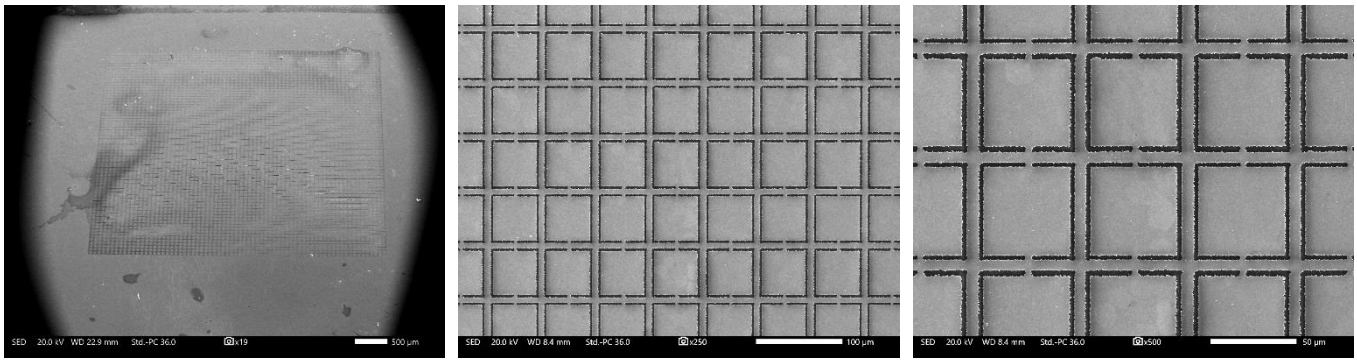

***Figure 7.4.22:*** SEM Images Of The 4-Foci Fabricated SRR Periodic Structure Through Ablation On Gold Thin Film

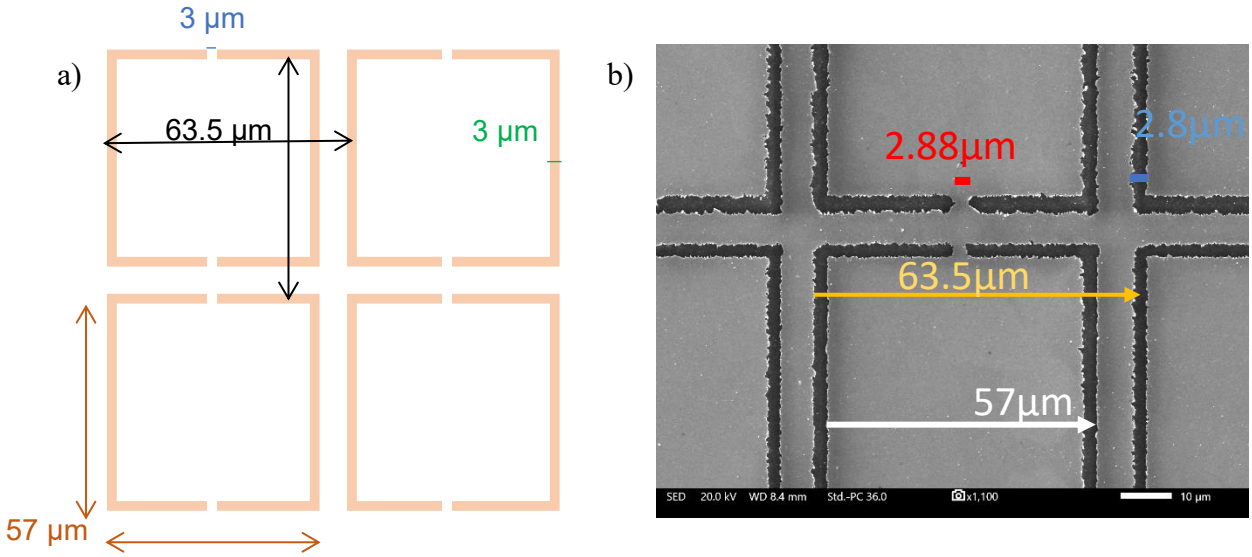


***Figure 7.4.23:*** Comparison Of a) The Computer Simulated SRR Periodic Structure Features With b) The 4-Foci Fabricated SRR Periodic Structure Features

SEM images prove that the gold thin film was truly ablated according to the designed path, creating a periodic SRR structure with features that come to a close approximation with the features of the computer simulated structure. Precisely, the length of each side in the meta-atoms and their periodicity are identical with the simulated features and correspond to 57 μm and 63.5 μm, respectively. However, the gap of the fabricated meta-atoms and the thickness of their sides is 2.88 μm and 2.8 μm (*fig. 7.4.23*). This is a completely acceptable deviation since there is not full control over the ablation sites and the energy distribution on the gold film. Moreover, the ablation features are directly depended on the objective lens that is used in the fabrication (in this case, 20×, N.A=0.4). This is, also, supported by the fact that if we take a closer look at the ablated sites of the gold film it is obvious that the ablated regions are not smoothly ablated (*fig. 7.4.24 (a)*).

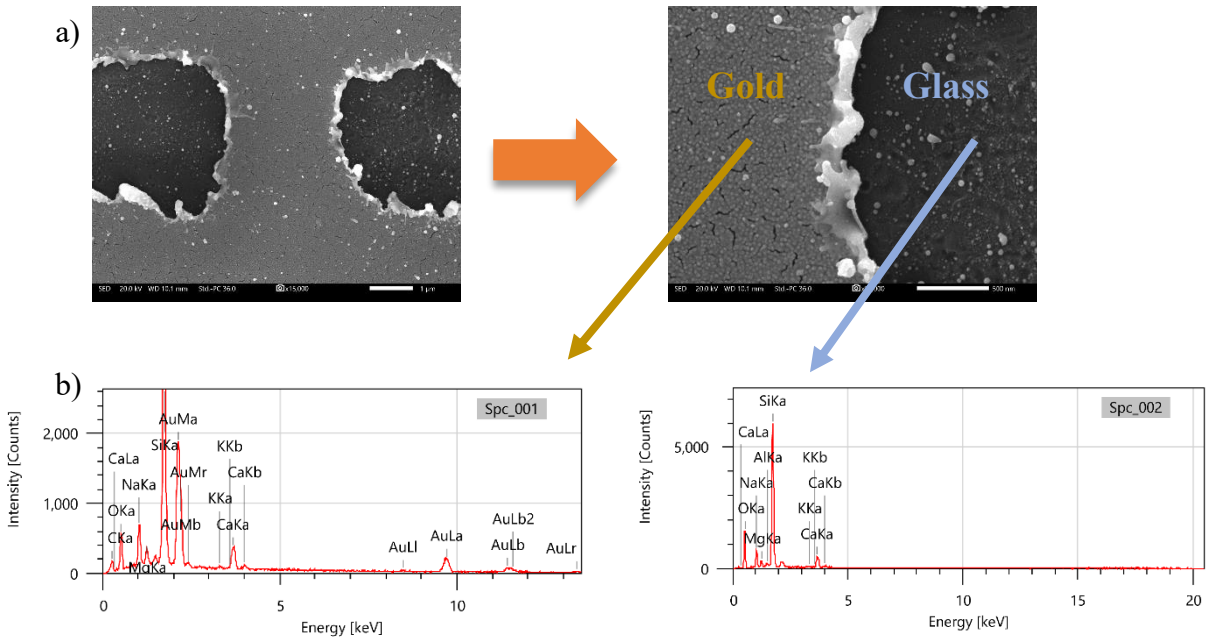


***Figure 7.4.24:*** a) SEM Images Of The Ablated Sites On The Gold Thin Film b) EDS Graphs Of Gold Thin Film And An Ablated Region

Even though the ablation is not smooth, Energy Dispersive Spectroscopy (EDS) graphs at the thin film of gold and at the ablated regions, prove that gold was completely ablated at the targeted sites (*fig. 7.4.24 (b)*). Moreover, It is calculated that the remaining gold nanoparticles do not affect the resonance frequency of the sample. The resonance frequency of the 4-foci SRR sample was theoretically calculated and compared with experimental measurements obtained for the detection of Metalaxyl-Agricultural Fungicide At A Variety Of Concentrations. The experimental results are depicted in figure (7.4.25), where one can observe the agreement between the theoretically (*fig. 7.4.20*) and experimentally calculated resonance frequency of the 4-foci SRR structure at the two different polarizations, i.e., 0 and 90 degrees. Measurements were performed by radiating the ablated meta-surface, with the fungicide on its top, using THz radiation and collecting the reflected radiation results.

Despite the fact that the sample need further optimization in order exhibit sharp resonance distributions at even lower concentrations, it is easily observed that it could potentially be used in the detection of more harmful substances, such as pesticides, in extremely small concentrations (ppb) because of the fact that these materials have electromagnetic response in the THz frequency region which is ideal for the detection of pollutants and other chemical residues.

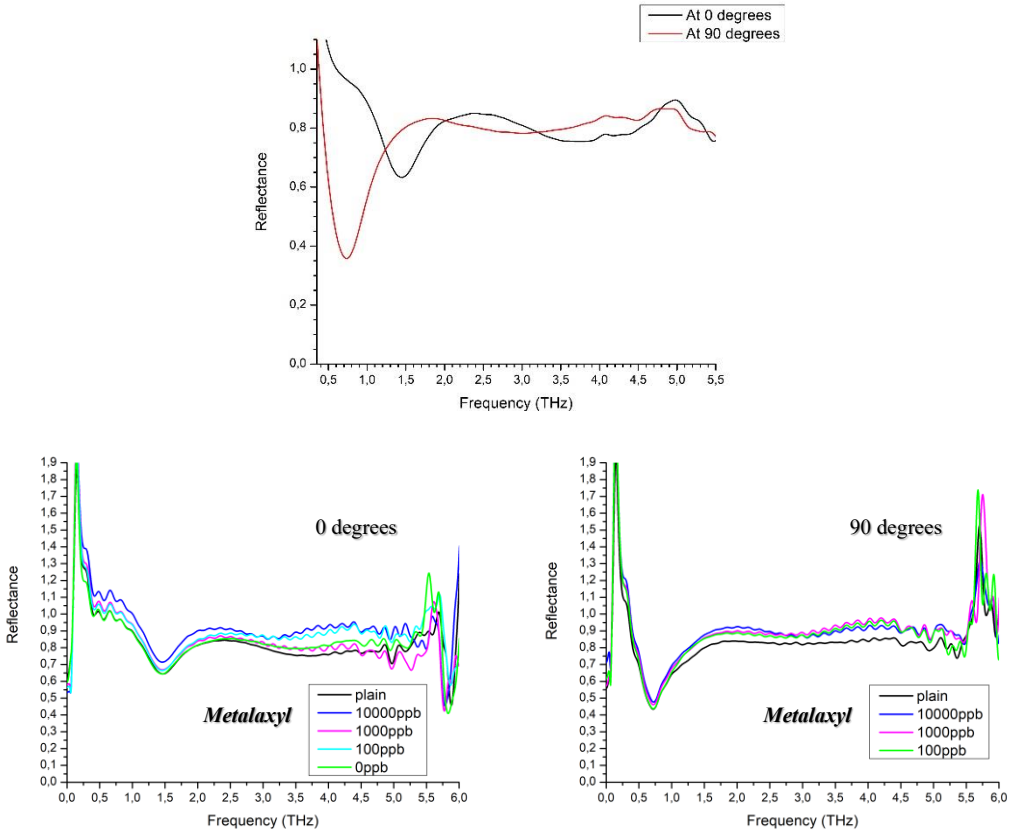


Resonance Measurements: Dr. Anastasios Koulouklidis, Ms. Christina Daskalaki, Mr. Constantinos Kerantzopoulos

***Figure 7.4.25:*** Theoretical And Experimental Results For The Resonance Spectrum Of The 4-Foci Fabricated Periodical SRR Structure At Two Different Polarizations, i.e., 0 and 90 Degrees. Experimental Results Obtained For The Detection Of Metalaxyl-Agricultural Fungicide At A Variety Of Concentrations

# 8. Pulsed Laser Deposition-ZnO Growth

## 8.1 Pulsed Laser Deposition

The porosity of the 3D spiral porous periodic structures makes them ideal candidates for photocatalytic applications. So, it was decided to test their photocatalytic efficiency in an aqueous environment by developing ZnO nanorods that will act as the needed catalyst of the process. The first step towards this direction was the deposition of a thin Zn film on the surface of the 3D porous structures by employing Pulsed Laser Deposition (PLD) method.

### 8.1.1 Experimental Process And Setup

The PLD process mechanism is based on an outside energy source (laser). For the purposes of this research, a KrF excimer laser (Lambda-Physik LPX 200), operating at 248nm with pulse duration 30 nanoseconds (ns), was used. This laser system provided the ability to adjust the repetition rate as well as the operating voltage. The laser beam was guided into the vacuum chamber by a set of properly placed mirrors. At the end of this optical path, just before the chamber, there was a spherical lens (f= +30 cm) with the aim to focus the laser beam into a 5 mm ×1 mm spot, irradiating the surface of the target material. A power meter was, also, utilized to measure the laser beam energy just before the chamber, minimizing, thereby, the error of the ablation energy measurement. The laser beam was introduced to the vacuum chamber through an optical window of quartz glass, which allows only light from the laser beam to pass.

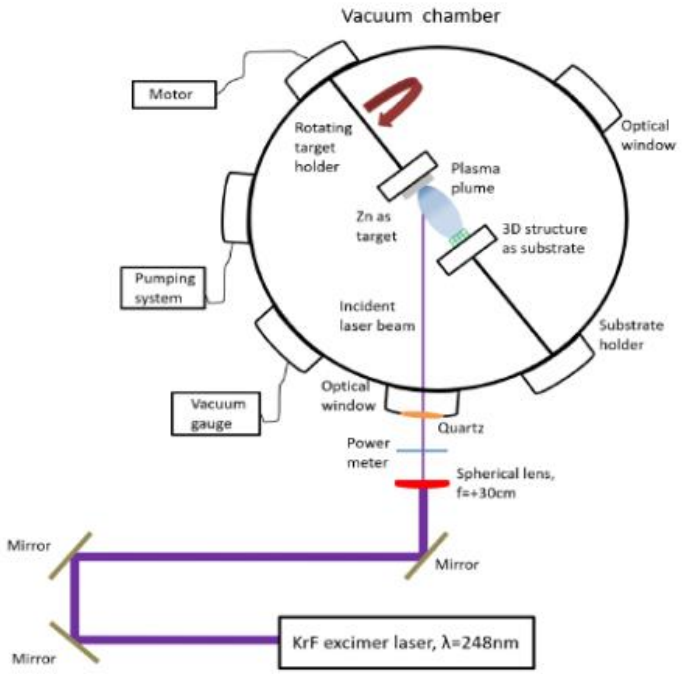


***Figure 8.1.1:*** Pulsed Laser Deposition (PLD) Experimental Setup

The chamber is directly connected with a vacuum pumping system, two vacuum gauges, a rotating target holder and a substrate holder. The pumping system consists of two pumps, a mechanical pump which was employed to create a preliminary low vacuum of $10^{-2}$ mbar and a turbomolecular pump, which was activated after the preliminary low vacuum, in order to reach a high vacuum pressure of $10^{-6}$ mbar. These vacuum conditions were essential for plume propagation and pure film growth. To monitor the vacuum conditions, a Pirani and a Penning gauge were used. The first gauge operates in a pressure range between $10^{3}$ mbar and $10^{-3}$ mbar, while the second one operates at pressure values between $10^{-3}$ and $10^{-8}$ mbar. The target material was a bulk zinc pellet (Zinc foil 99,95 percent. Goodfellow), and the substrate samples were the fabricated 3D porous microstructures. To minimize crater formation, the target was rotated during the laser ablation of the material and the irradiation spot was targeted off-centered in the pellet target material to achieve smooth ablation along its surface. Optical windows ran the length of the vacuum chamber, allowing the PLD process to be monitored in real time. The pressure of an ambient gas within the chamber, as well as the temperature of the substrate, were two critical parameters in traditional PLD studies. However, they were not investigated in this study.

The PLD process started by properly aligning the optical path of the beam so that the laser beam irradiates the target material. The alignment was completed by irradiating a photosensitive paper with one pulse. The imprint of the spot in the photosensitive paper provides information about the spot size, which must have a rectangular shape to support smooth ablation and no-crater formation. The vacuum chamber was sealed once the 3D structure was placed on the substrate holder, with a target-to-substrate distance of 4 cm and a 45° angle of the incident beam to the target surface. The desired vacuum conditions of 6.3 x $10^{-6}$ mbar were achieved using the pumping system as well as the vacuum gauge described above. A power meter was, also, used to measure the energy of the laser beam at this stage of the experiment.

Since the laser beam's spot size was measured, the laser fluence (energy/surface) could be calculated. Then, the fluence could be set to fit the desired value by adjusting the laser beam's energy. For this purpose, the repetition rate is set to 10 Hz and the motor that moves the target holder is turned on. For all the depositions in this experiment, the target's rotation speed and the target-to-substrate distance are kept constant. The laser fluence was calculated to be 2 J/cm$^2$ [54], [55], [56].

Each substrate sample was irradiated with a total number of 2000 pulses throughout the experiment. This number can be adjusted by altering the repetition rate or the total time of the deposition. In this case, the total time of the deposition was 3 minutes and 20 seconds and it is calculated below

$$t_{total}(s) = \frac{number\ of\ pulses}{repetition\ rate\ (Hz)} = \frac{2000\ pulses}{10\ Hz} = 200\ s = 3.20\ min$$

After the irradiation, both pumps were turned off, since the laser ablation and the film growth were completed. When the chamber got unsealed, one could realize that the three-dimensional structure was indeed coated by a thin film of Zn.

## 8.1.2 Deposition Of Thin Zn Film On Glass Substrate

Initially, in order to check the efficiency and the smooth operation of the PLD process we placed a microscope glass into the vacuum chamber of the PLD setup. Once the vacuum of the chamber had reached the desired value of $6.3 \times 10^{-6}$ mbar, we placed the sample in the chamber and the irradiation started. The total time of irradiation was 3 minutes and 20 seconds with a repetition rate at 10 Hz and a total number of 2000 pulses. The glass substrate was placed on the holder with a target-to-substrate distance of 4 cm and a 45° angle of the incident beam to the target surface. The laser fluence was 2 J/cm$^2$. During irradiation, the Zn target was rotating. After the irradiation was completed, we opened the chamber we noticed that the glass sample had changed color (tends to dark gray). This indicates that the PLD experiment was successful.

## 8.1.3 Deposition Of Thin Zn Film On 3D-Porous Periodic Structures

Since we made sure that the PLD procedure that was followed for the Zn deposition on the glass substrate was successful, we repeated the same PLD steps and parameters for coating with a thin film of Zn the 3D spiral porous periodic media. These media had the same features with the structures (i)-(iv), presented in part (7.4.1), but all of them had the same dimensions of 1 mm×1 mm. So, the PLD was utilized for the coating of seven 1 mm×1 mm samples of 3D porous microstructures, fabricated according to the features of (i)-(iv) samples. After the irradiation of each sample was completed, we waited for a short period of time for the mechanical forces inside the chamber to calm down and we opened the chamber. We noticed that the sample had changed color (tends to gray), a fact that indicates that the deposition was successful. In total, we did seven Zn depositions, one for each sample, following the steps and parameters that are described in the previous parts (8.1.1) and (8.1.2). The following figure (*fig. 8.1.2*) show one of these 3D dimensional porous structures before and after irradiation based on the Pulsed Laser Deposition technique.

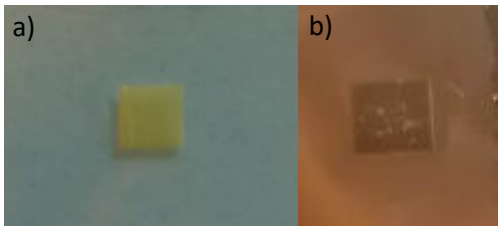


***Figure 8.1.2:*** 3D Porous Periodic Structure a) before and b) after Pulsed Laser Deposition (PLD)

## 8.2 ZnO Growth Technique

The next step, after the deposition of the Zn film in the 3D porous structures, was the development of the ZnO nanorods. This was possible by following the development steps of an Aqueous Chemical Growth (ACG) Technique. This technique is analytically presented in the next parts.

### 8.2.1 Aqueous Chemical Growth (ACG)

Aqueous chemical growth (ACG) is a fairly straightforward solution growth approach for growing nanostructures of diverse materials. As a technique, it is carried out at low temperatures, which has various advantages, including the use of low-cost equipment, the employment of inexpensive and non-toxic chemicals and the existence of non-hazardous by-products. The large size of development area combined with the fact that low temperatures are required is one of ACG's major benefits over other growth processes such as physical vapor deposition (PVD) and vapor liquid solid (VLS). In this work, ACG was followed for the growth of ZnO nanorods on the surface of the 3D microstructures and at their total volume [54], [55], [56].

### 8.2.2 Aqueous Chemical Growth (ACG) Process

Sigma-Aldrich provided all of the chemicals utilized in this master thesis: Zinc nitrate hexahydrate ($Zn(NO_3)_2 \cdot 6H_2O$, 98%) and ammonium hydroxide solution in water (28 wt% $NH_3$ in $H_2O$).

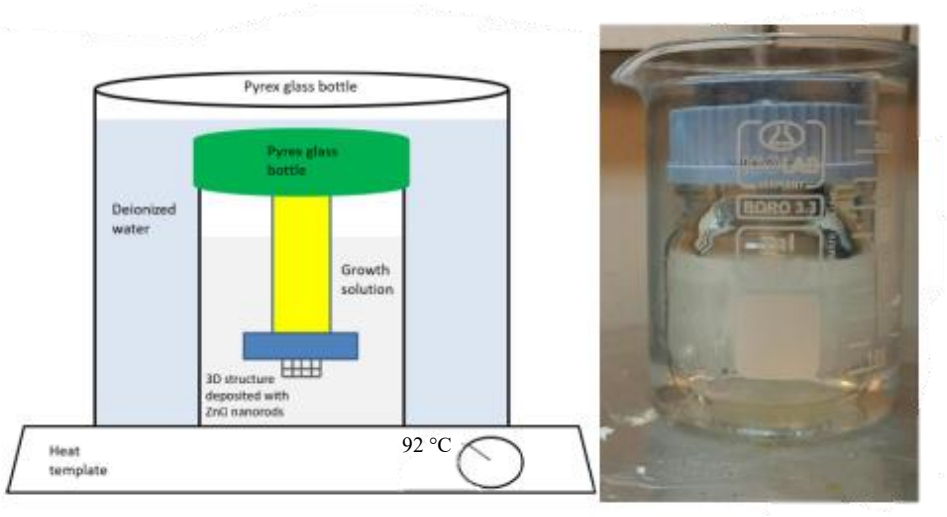


***Figure 8.2.1:*** Presentation And Real Image Of The Chemical Growth Experimental Setup. The 3D Structures Are Localized Bottom-up In Growth Solution In Order To Form ZnO Nanorods On Them Without Gravitational Effects.

To make a 0,02 M growth solution, a calculated amount of zinc nitrate hexahydrate was dissolved in 100 mL of deionized water. The pH of the growth solution was adjusted using ammonia water. The amount of ammonia water added was 3.1 ml. As previously stated, a Zn thin film was deposited on the 3D structures, which is a critical parameter for the growth of ZnO nanorods because it serves as a seed layer to promote nanorod alignment on the 3D substrates. Hydrothermally, ZnO nanorods growth was carried out by suspending the 3D structures deposited with zinc, bottom up in a glass bottle filled with the growth solution (*fig. 8.2.1*). The growth temperature was selected at 92 ℃ and growth time was 2 hours and 10 minutes, approximately. After the chemical growth, the samples were removed from the solution and were immersed for few minutes in a solution of deionized water and they were dried in air for another 15 minutes [54], [55], [56].

## 8.2.3 Aqueous Chemical Growth Of ZnO Nanorods On 3D Porous Periodic Structures And A Glass Substrate

As it was mentioned earlier, the development of ZnO nanorods, on the surface of the 1 mm × 1 mm 3D porous periodic structures, was a necessary step in order to study their photocatalytic activity. Based on the procedure of part (8.2.2), the ZnO growth started by counting 100 mL of deionized water and inserting this amount into a small Pyrex bottle, together with 3.1 ml ammonia and 0.02 M of Zinc nitrate hexahydrate ($Zn(NO_3)_2 \cdot 6H_2O$, 98%). Then, the Pyrex bottle was immersed in water, with the help of a beaker, in such a way so that the water covered the Pyrex bottle. Both the Pyrex and the beaker were placed on a heater. When the water reached 92 °C, the counting started, for about 2 hours and 10 minutes. Small magnets were inserted in the beaker so that the vibrational disturbance in the wall of the inner bottle would create a light stirring that would help the zinc inside the solution to stick on the Zn coated structure that we had placed upside down.

During the experiment, we checked randomly the amount of water inside the beaker to make sure that it will continuously cover the Pyrex bottle, as well as that the Pyrex bottle would not rest neither in thermometer that monitored the temperature of the solution nor on the walls of the beaker. After completing the experiment, dipping the sample in water and drying it in the air, SEM images were obtained, in various magnifications, in order to observe the development of the ZnO nanorods. It must be noted that, optically, an indicator of the successful ZnO growth was the fact that the dark grey film of Zn that was deposited in the samples had changed after ACG technique into a white power. The same procedure was repeated for each one of the seven 1 mm × 1 mm 3D spiral porous periodic structures and for a 1 mm × 80 mm reference surface sample (Zn film) in glass substrate. The results are presented below according to the distance of the 4-foci that were used for the fabrication of each sample.

- ***101 µm point by point***

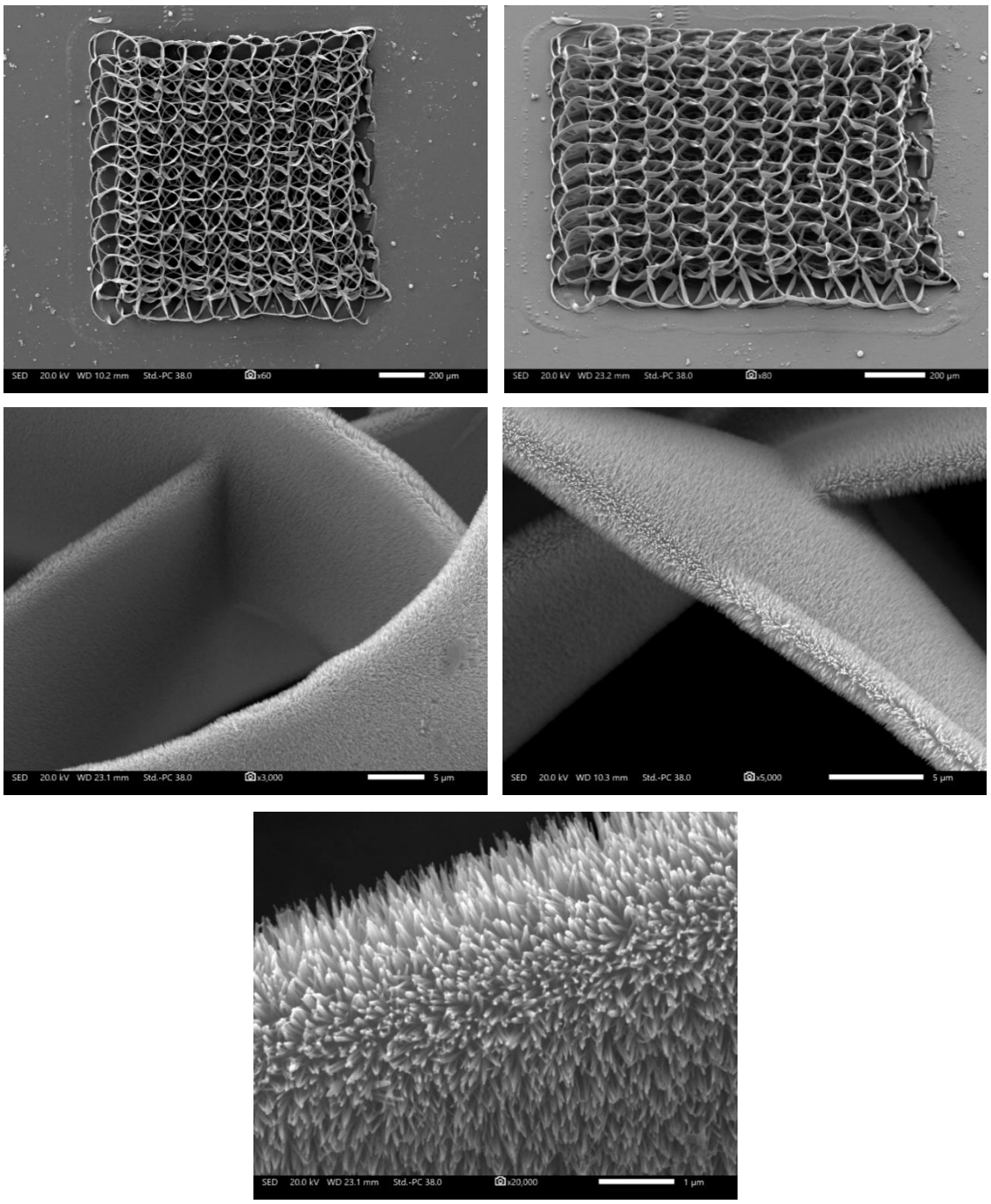


***Figure 8.2.2:*** SEM Images of 3D Spiral Porous Periodic Structure Fabricated By 101 µm Point By Point 4-Foci Phase Mask After ZnO Nanorods Growth On Its Surface

The 3D structure of figure (8.2.2) has an array of 12×12 spirals or coils, with a diameter of 101 µm, that overlap with each other, creating a 1200 µm × 1200 µm or 1.2 mm × 1.2 mm porous sample. The total fabrication time was 3.3 minutes for the laser writing part and 2 hours and 10 minutes for the ZnO nanorods growth part. The total power was 110 mW or 0.550 µJ and the maximum pore size obtained in this structure was 70 µm while the minimum was 37 µm

- ***56.7 µm point by point***

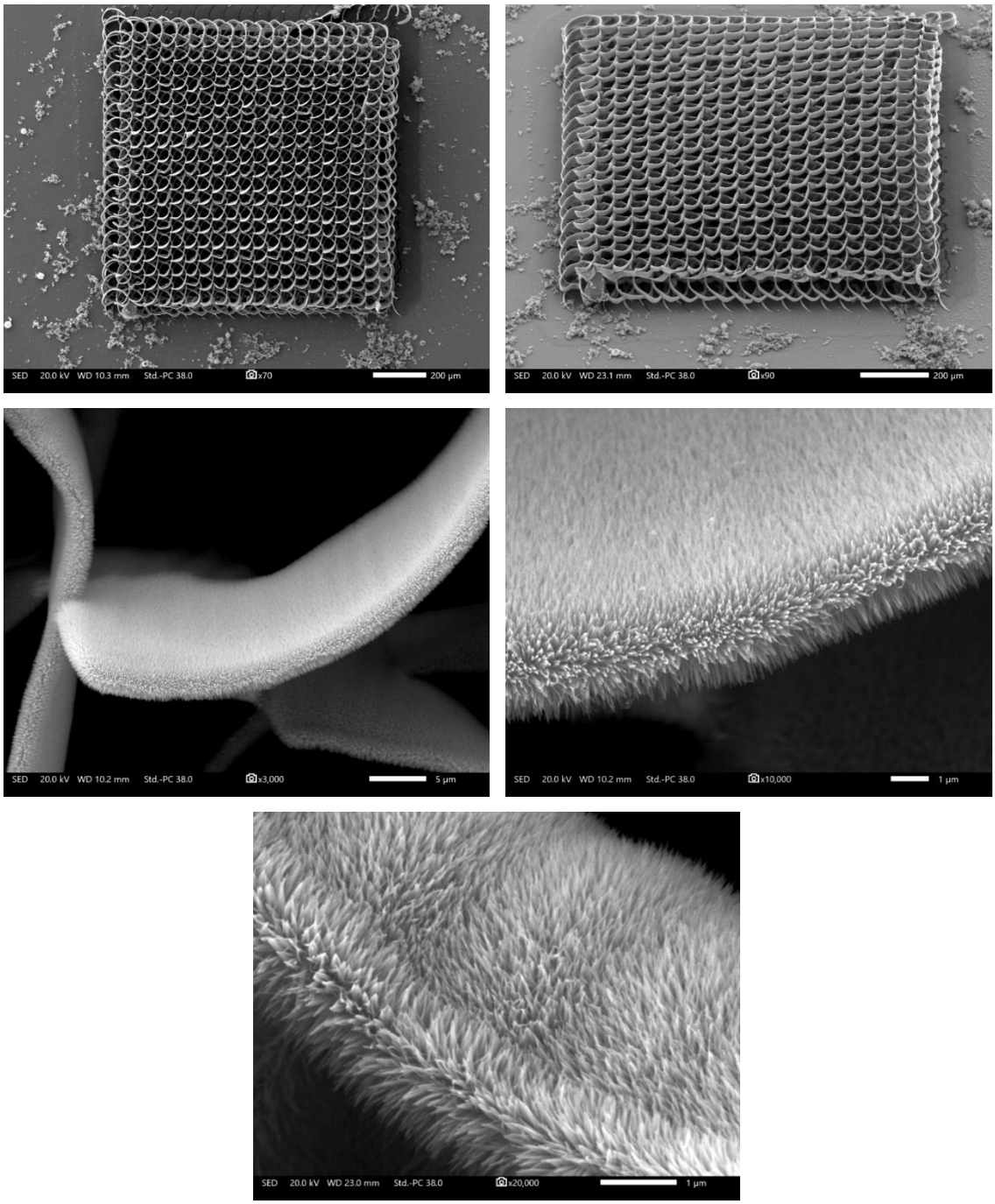


***Figure 8.2.3:*** SEM Images of 3D Spiral Porous Periodic Structure Fabricated By 56.7 µm Point By Point 4-Foci Phase Mask After ZnO Nanorods Growth On Its Surface

The 3D structure of figure (8.2.3) has an array of 20×20 spirals or coils, with a diameter of 56.7 µm, that overlap with each other, creating a 1134 µm × 1134 µm or 1.134 mm × 1.134 mm porous sample. The total fabrication time was 3.04 minutes for the laser writing part and 2 hours and 10 minutes for the ZnO nanorods growth part. The total power was 149 mW or 0.745 µJ and the maximum pore size obtained in this structure was 33 µm while the minimum was 20 µm

- ***34.5 µm point by point***

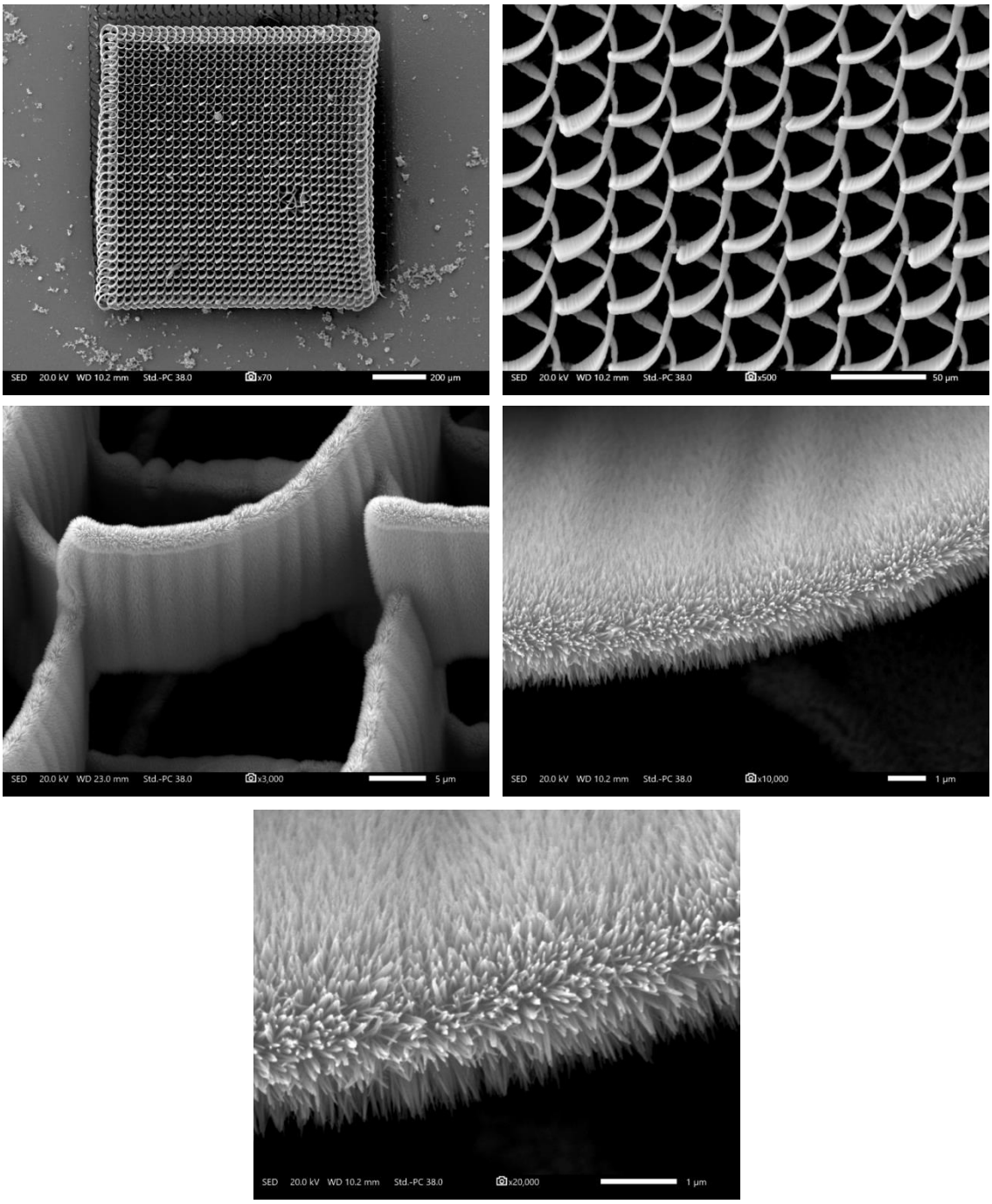


***Figure 8.2.5:*** SEM Images of 3D Spiral Porous Periodic Structure Fabricated By 34.5 µm Point By Point 4-Foci Phase Mask After ZnO Nanorods Growth On Its Surface

The 3D structure of figure (8.2.5) has an array of 32×32 spirals or coils, with a diameter of 34.5 µm, that overlap with each other, creating a 1104 µm × 1104 µm or 1.104 mm × 1.104 mm porous sample. The total fabrication time was 5.01 minutes for the laser writing part and 2 hours and 10 minutes for the ZnO nanorods growth part. The total power was 129 mW or 0.645 µJ and the maximum pore size obtained in this structure was 19 µm while the minimum was 10 µm.

- ***28.6 µm point by point***

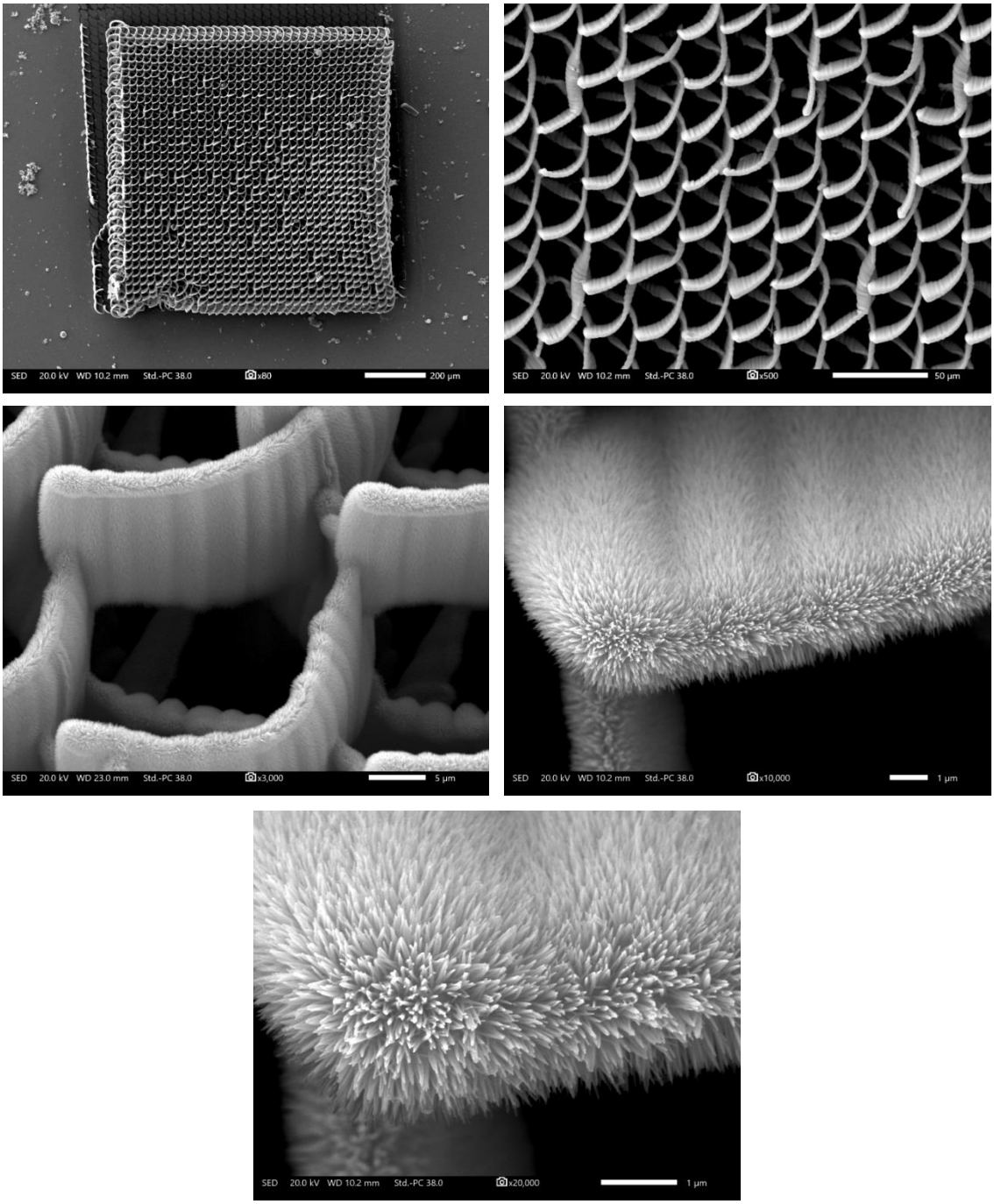


***Figure 8.2.6:*** SEM Images of 3D Spiral Porous Periodic Structure Fabricated By 28.6 µm Point By Point 4-Foci Phase Mask After ZnO Nanorods Growth On Its Surface

The 3D structure of figure (8.2.6) has an array of 36×36 spirals or coils, with a diameter of 28.6 µm, that overlap with each other, creating a 1029 µm × 1029 µm or 1.029 mm × 1.029 mm porous sample. The total fabrication time was 5.24 minutes for the laser writing part and 2 hours and 10 minutes for the ZnO nanorods growth part. The total power was 135 mW or

0.675 µJ and the maximum pore size obtained in this structure was 15 µm while the minimum was 7 µm.

- ***17.4 µm point by point***

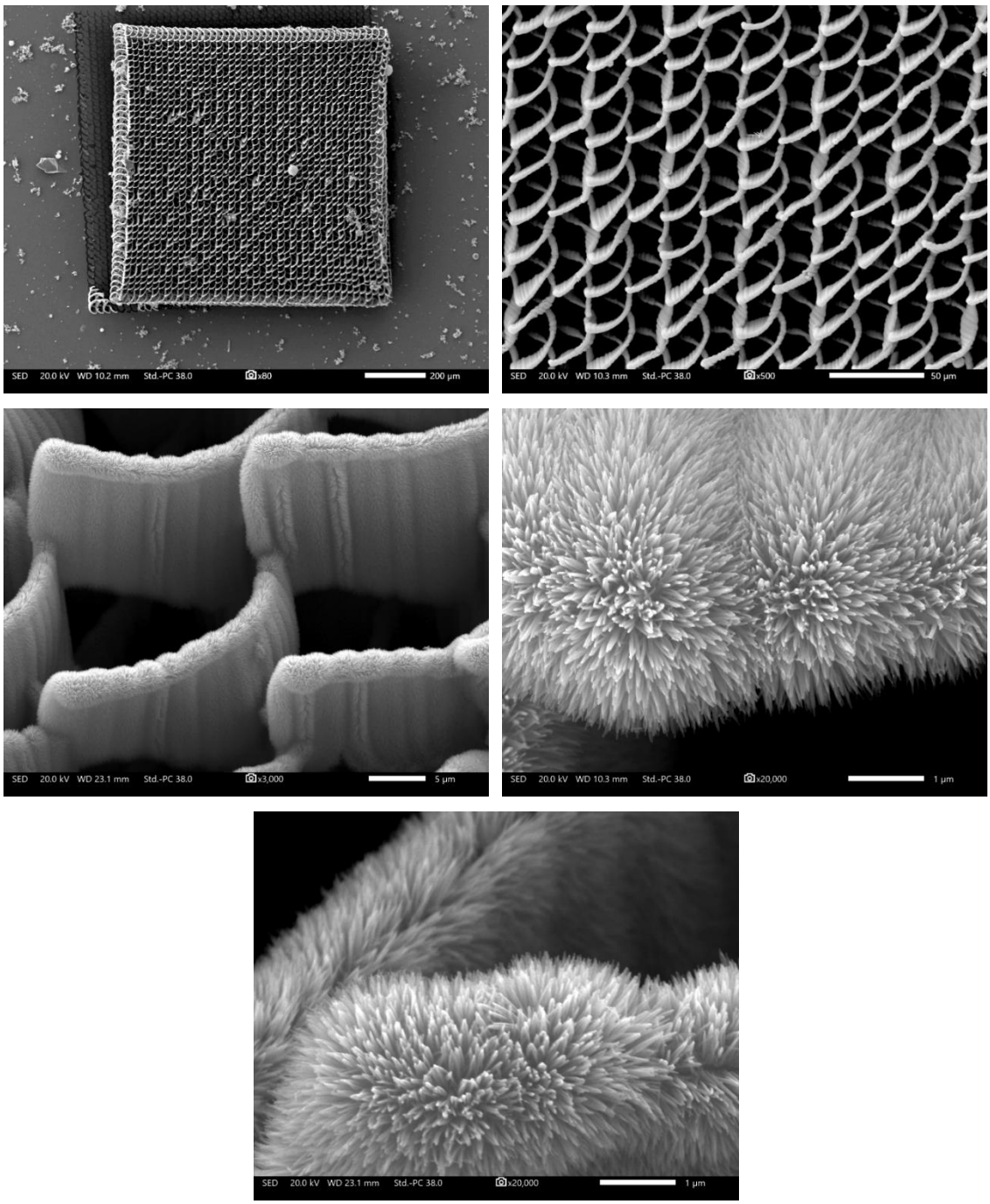


***Figure 8.2.8:*** SEM Images of 3D Spiral Porous Periodic Structure Fabricated By 17.4 µm Point By Point 4-Foci Phase Mask After ZnO Nanorods Growth On Its Surface

The 3D structure of figure (8.2.8) has an array of 60×60 spirals or coils, with a diameter of 17.4 μm, that overlap with each other, creating a 1044 μm × 1044 μm or 1.044 mm × 1.044 mm porous sample. The total fabrication time was 11 minutes for the laser writing part and 2 hours and 10 minutes for the ZnO nanorods growth part. The total power was 140 mW or 0.700 μJ and the maximum pore size obtained in this structure was 8 μm while the minimum was 3 μm.

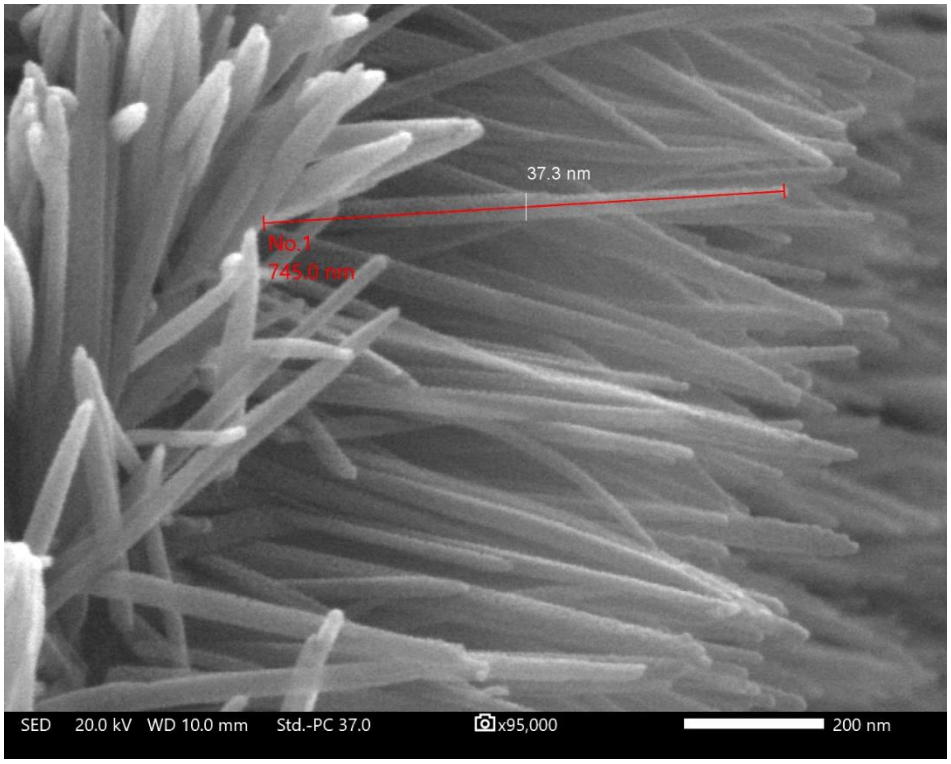


***Figure 8.2.9:*** SEM Image of ZnO Nanorods On The Sample Surface at ×95000 Magnification. The Length Of Each Nanorod Is Calculated To Be Approximately 745 nm While Its Thickness Is Equal To 37.3 nm

Comparing the results from the ZnO nanorods coated structures, we have no doubt that the ZnO nanorods growth process was successful. Specifically, we can observe that each one of the seven samples is coated with ZnO nanorods along its surface, following the designed geometry in its total volume, and the length of each nanorod is calculated to be ~745 nm while its thickness is equal to 37.3 nm (*fig. 8.2.9*). Moreover, the deposition of the Zn seed layer during the PLD process, led to a uniform growth of ZnO nanorods in the porous sample, as SEM images reveal. One can, also, notice that the growth was directed towards the development of vertically aligned nanorods. This is an important parameter because it ensures the uniform growth and it gives us the opportunity to observe the successful coating in every region of the sample. If the coating was random, ZnO nanorods or even nanoparticles could overlap leading to many hidden, un-coated sites on the surface of the samples. Hence, we can easily assume that every region of the sample will equally contributes to the photocatalytic activity.

Besides the above observations, it must be stressed out that most of the ZnO nanorods coated structures, seem to have a minor detachment from the glass substrate after the ACG method.

This is mostly obvious in the last sample but we can see that the morphology of the first sample is, also, affected. This is an expected result because temperature affects the mechanical stability of the structures, especially when they have features at few micro- or nanometers, since there is a tendency of shrinkage as temperature rises. In general, the temperature cannot be fully controlled and there are slight variations, at the order of ± (2-3) °C, from the desired temperature of 92 °C. However, this research is static, i.e., the photocatalytic activity of the samples is not tested inside a flow system, and thus the photocatalysis results are not affected by the mechanical stability. In any case, we can avoid such effects by carefully monitor the growth temperature over the duration of the experiment or by applying appropriate techniques that will provide an increased mechanical stability.

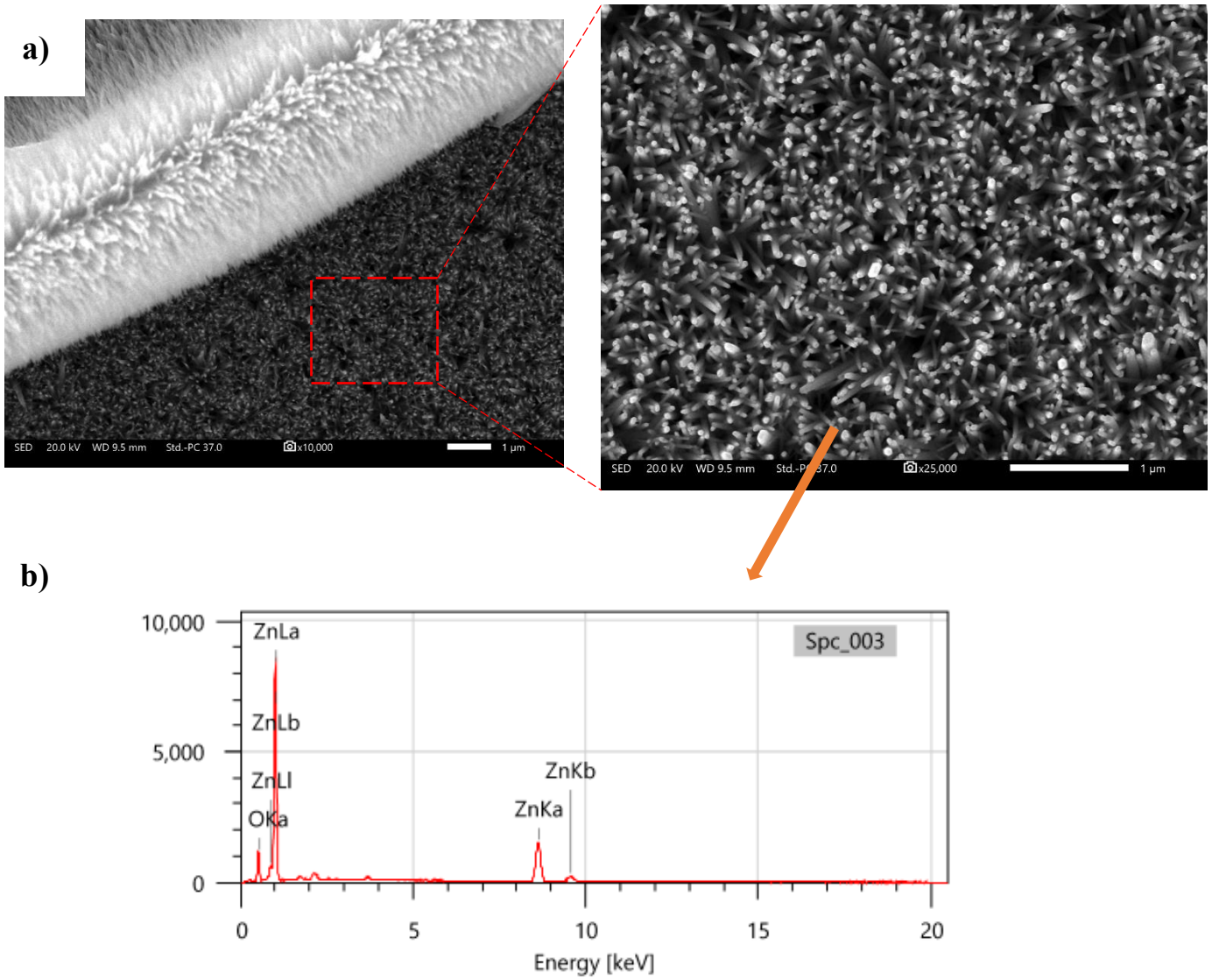


***Figure 8.2.10:*** a) SEM Images Of The Area Around The Sample. ZnO Nanorods Are Developed Both On The Sample Surface And At The Glass Substrate b) EDS Graph Of ZnO Nanorods At The Glass Substrate

Another important factor that must be considered is that the Zn seed layer deposition is not limited only on the polymer substrates, i.e., the 3D structures. Instead, a seed layer is deposited

in a specific area around the porous media. In this work, the area is equal to 80 $mm^2$ and is taken into account for the photocatalysis measurements. This is supported by SEM images taken at the boundaries between the polymer structure and the glass substrate where traces of Zn are presented. An EDS graph was, also, obtained (*fig. 8.2.10*).

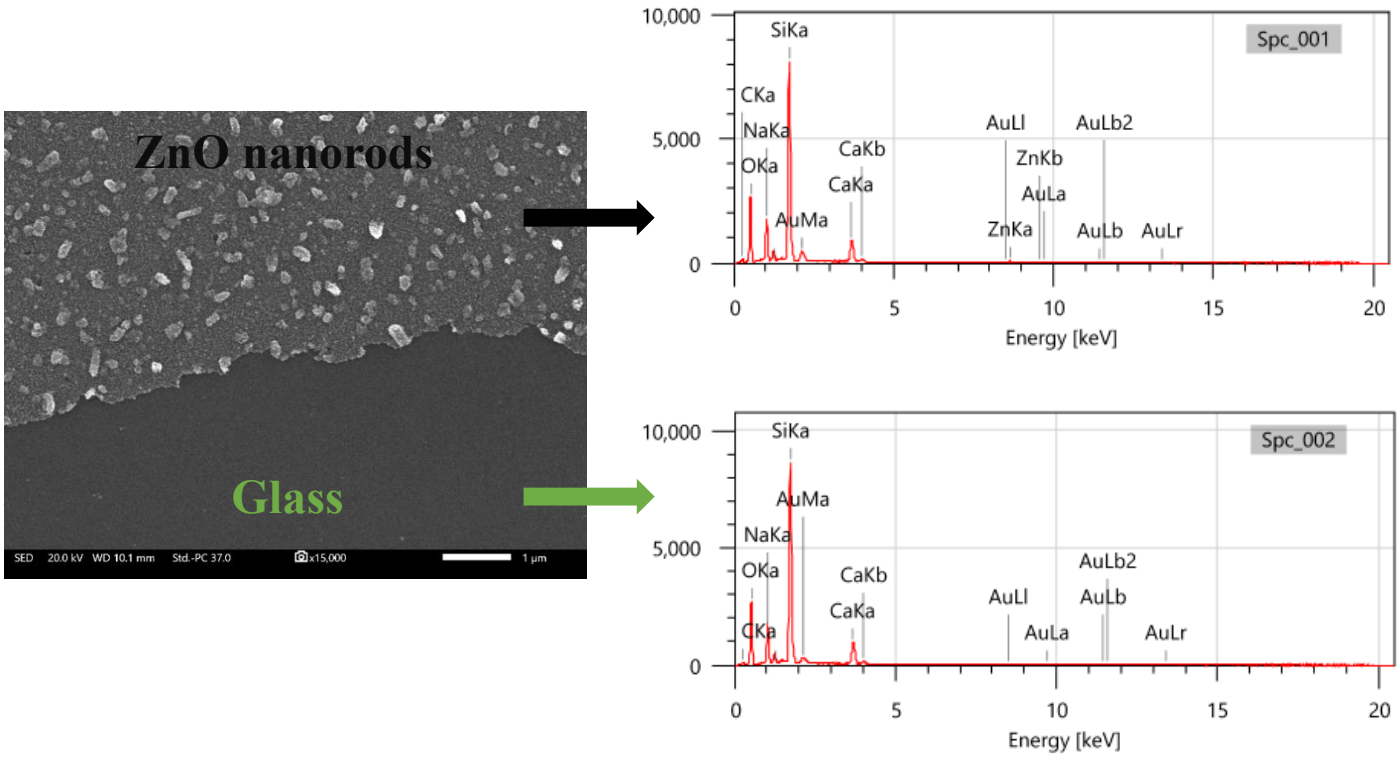


***Figure 8.2.11:*** SEM Image And EDS Graphs At The Limit Of The ZnO Coated And Non-Coated Glass Substrate

Finally, SEM images and EDS graphs were obtained at the limit of the ZnO coated with the non-coated glass substrate. This step ensures that the deposition of the Zn seed layer and the growth of ZnO nanorods on the glass substrate is within the predefined surface area (*fig. 8.2.11*).

# 9. Photocatalytic Activity Results

## 9.1 Introduction

The final step, after the successful growth of the ZnO nanorods on the surface of the 3D porous structures, was to test their photocatalytic efficiency. There is a wide variety of possible techniques able to perform such an activity. For example, photo-oxidation of organic films, such as stearic acid, methylene blue photodegradation in aqueous solutions, and contact angle changes are all popular approaches. In this master thesis, the photocatalytic activity of the 3D porous structures is tested by measuring the decolorization of methylene blue (MB) in aqueous solution. Methylene Blue (MB) is toxic, carcinogenic, and non-biodegradable and can cause a severe threat to human health and environmental safety. It is usually released in natural water sources, which becomes a health threat to human beings and living organisms [57], [58], [59].

## 9.2 Experimental Setup

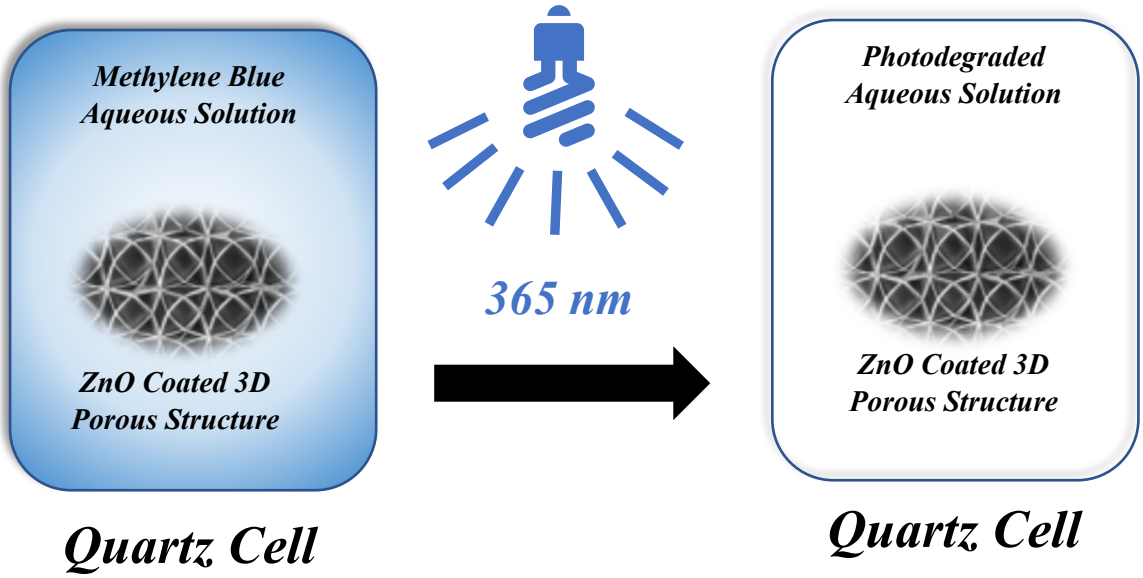


***Figure 9.2.1:*** Illustration Of The Experimental Process For Decolorization Of Methylene Blue In Aqueous Solution Under UV Illumination

During the photocatalysis measurements, every sample was placed, individually, in a custom-made quartz cell. The whole setup was illuminated for up to 60 min, using a UV lamp centered at 365 nm (Philips HPK 125 W), with a light intensity of ~10 mW/cm$^2$. With this experiment, the decolorization of methylene blue in aqueous solution was tested (*fig. 9.2.1*). In general, when ZnO is excited by UV light, the semiconductor absorbs photons whose energy is equal to or greater than their band-gap energy $E_G$ ($h\nu \geq E_G$). Then, electrons and holes are created. The degradation process consists of a series of radical oxidations, initiated by strong oxidants

such as OH· and ·$O_2$. Oxidants are directly generated by the photolysis of water molecules, adsorbed by the active sites of the ZnO semiconductor. Organic pollutants, adsorbed on the catalyst, are then degraded by successive radical reactions in non-toxic mineral species. The chemical reactions from the UV light excitation of ZnO, that lead to the photodegradation of Methylene Blue, are presented below [60]

$$ZnO + \hbar v \rightarrow h^+ + e^+ \qquad (\textit{ZnO Excitation})$$

$$H_2O + h^+ \rightarrow H^+ + \cdot OH \qquad (\cdot \textit{OH Radicals Formation})$$

$$e^- + O_2 \rightarrow O_2^- \qquad (O_2^- \textit{ Radicals Formation})$$

$$h^+ + OH^- \rightarrow OH \qquad (\textit{Hydroxyls Formation})$$

$$O_2^- + H_2O + H^+ \rightarrow H_2O_2 + O_2 \qquad (\textit{Hydrogen Peroxide And Oxygen Formation})$$

$$O_2^- + (\text{Organic Species}) \rightarrow (\text{Organic Species})\text{-}OO\cdot \qquad (\textit{Peroxides Formation})$$

$$^{-}OH + (\text{Organic Species}) \rightarrow (\text{Oxidized Product}) \qquad (\textit{Photodegradation})$$

# 9.3 Results

## 9.3.1 Methylene Blue Photodegradation

**a)**

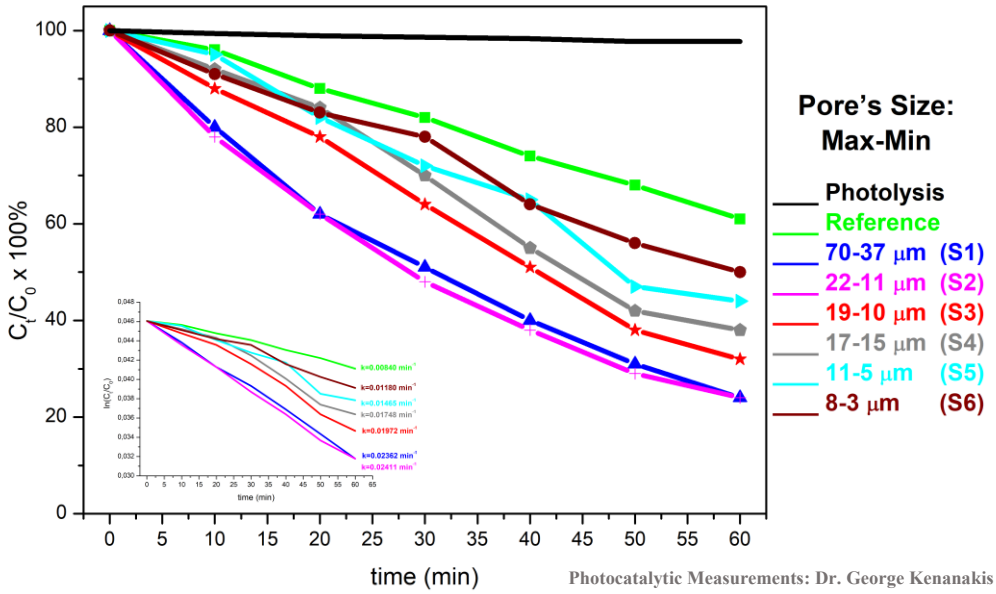


**b)**

| | Pores' Size: Max-Min (μm) | Active Surface Area ($mm^2$) | Rate Constant k ($min^{-1}$) |
|---|---|---|---|
| Photolysis | - | - | 0.00040 |
| Reference | - | 80 | 0.00840 |
| **Sample 1** | **70-37** | **80 + 0.3902** | **0.02362** |
| **Sample 2** | **22-11** | **80 + 0.8695** | **0.02411** |
| Sample 3 | 19-10 | 80 + 0.9677 | 0.01972 |
| Sample 4 | 15-7 | 80 + 1.0303 | 0.01748 |
| Sample 5 | 11-5 | 80 + 1.1953 | 0.01465 |
| Sample 6 | 8-3 | 80 + 2.0313 | 0.01180 |

***Figure 9.3.1:*** a) Photocatalysis Results For The Decrease Of Methylene Blue (MB) Concentration Over Time In A Reference Sample (ZnO Film In Glass Substrate) And Each One Of The Six 3D Porous Structures. b) Pores' Size (μm), Total Active Surface Area ($mm^2$) And Rate Constant k ($min^{-1}$) For Samples 1-6

For quantifying the ZnO induced MB concentration decrease and the photocatalytic activity of the various structures, the apparent rate constant (k) has been estimated, according to

$$ln(\frac{C_t}{C_0}) = -kt$$

where $C_0$ is the initial MB concentration, $C_t$ is the concentration after a time interval t and k is specific rate constant for the first order kinetics reaction.

In figure (*9.3.1 (a)*), the photocatalysis results are presented. The black line refers to the photolysis, where no ZnO is present during the measurements. Thus, over time, the concentration of MB (Methylene Blue) is not affected as a result of the lack of semiconductor. The green line indicates a ZnO film, where ZnO nanorods were developed directly in a glass substrate through the two-step process of PLD and ACG. All the other lines refer to the 3D Spiral Porous Periodic Structures coated with ZnO nanorods. One can easily observe that the photocatalytic activity is severely improved when a 3D porous medium is used to replace a 2D semiconductor surface (reference sample). Comparing the results, it is obvious that samples (1) and (2) seem to be the most efficient during the photodegradation of MB, degrading up to 70% and 76% of the initial MB concentration within 60 minutes. Samples (3), (4), (5), (6) are much more efficient when compared with the reference sample but still are not among the best options when it comes to the results from the photodegradation of MB. There is an additional sample with pore sizes (33-20) μm that is considered defective and further evaluation of its photocatalytic activity will be performed.

There are two additional important aspects that must be investigated in order to fully exploit the above measurements. These are the relation between the pores' size and the rate constant k and the relation between the active surface area and the rate constant k. For this purpose, the active surface area of each 1 mm × 1 mm ZnO coated 3D porous structure was calculated by adding the 2 μm × 2 μm spot size of each voxel and its 14 μm length, multiplied by 2 to include the active surface area of both sides in a voxel and then multiplied with the total number of voxels in each structure. The total data, including the 80 $mm^2$ reference sample, are presented in figure (*9.3.2 (b)*).

As it is already mentioned, theory states that increasing the surface area leads to an increased number of catalytic sites available for reaction and, hence, an increased catalyst productivity. Following this line of thought, it is realized that as the pores' size decreases the active surface area will be increased, taking for granted that all the samples have approximately the same physical dimensions of 1 mm × 1 mm. In other words, as the empty space that the pores create in a sample decreases, the active surface area gets bigger. So, one would expect that the sample (6) would have the most efficient photocatalytic activity in comparison with the other samples, since the pores' size decreases from sample (1) to sample (6). The results of figure (9.3.1) show that this is not the case. The size of the active surface area may slightly affect the photocatalytic activity but the most important parameter seems to be the size of the pores when samples with the same physical dimensions are compared.

In figure (*9.3.2*), the relation between the maximum size of the pores and the rate constant k is depicted. As the size of the pores is increased, so does the rate constant k. This increasement reaches its maximum value for sample (3) and then, a saturation regime in the rate constant k is observed. This confirms the results of figure (*9.3.1 (a)*), where the sample (3) exhibits the most efficient photocatalytic activity but, also, proves that there is a region of preferable pore sizes above 22 μm, in such media, so that they are able to maximize their activity in photocatalytic applications.

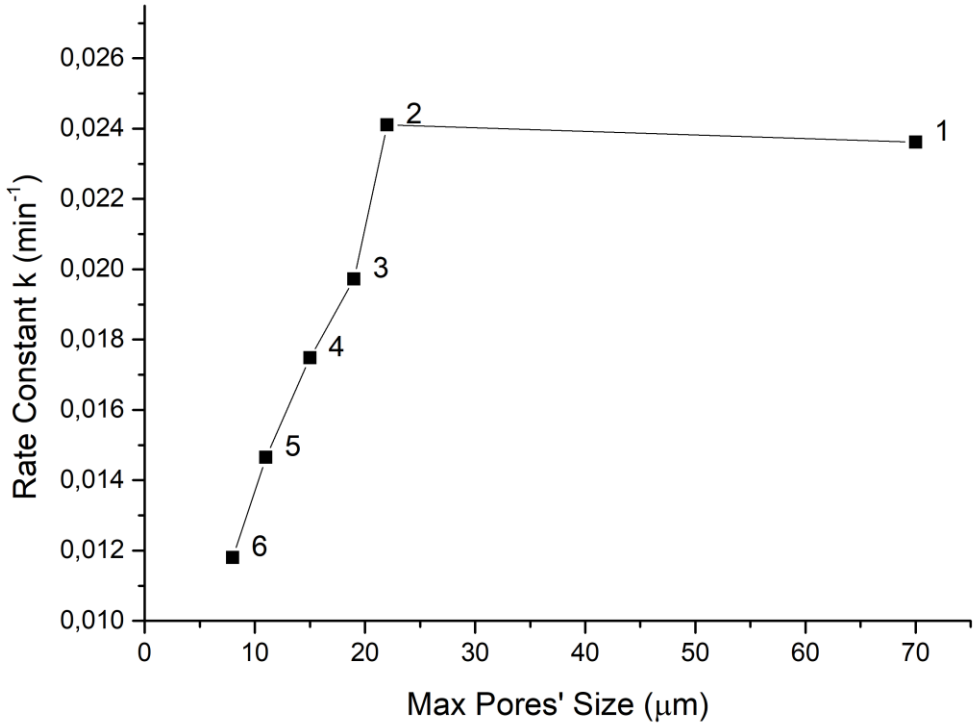


***Figure 9.3.2:*** Graph Showing The Relation Between The Maximum Pores' Size And The Rate Constant k In Samples (1)-(6)

The reason behind the inconsistency of the theory and experiment, in the topic of active surface area, may be related with the fact that there is a strong possibility that at pores' size values lower that 22 μm, air pockets are created inside the 3D structures and they are not allowing the aqueous solution of MB to flow through, in every catalytic site available. To address this issue, contact angle measurements were obtained for these samples in order to test the ability of an aqueous solution to flow through the structures will low pores' size values.

## 9.3.2 Contact Angle Measurements

By performing contact angle measurements, we were able to determine the degree of wetting or spreading of the liquid MB-solution on the solid surface of the 3D porous structures presented in the previous parts [61].

Contact angle measurement is a widely used technique in surface science and materials research that gives us the ability to characterize the wetting properties of solid surfaces. Contact angle is realized by the angle formed at the liquid-solid interface, when a droplet of liquid comes into contact with the solid surface and it provides valuable information about the wettability of the material. A high contact angle indicates poor wetting (hydrophobicity), where the liquid forms a more spherical droplet, while a low contact angle indicates good wetting (hydrophilicity), with the liquid spreading out and covering a larger area on the surface. In this case, the measurements were obtained by fabricating larger samples of 5 mm × 5 mm, placing water droplets on the surface of samples (1), (5), (6) and measuring the angle formed at the liquid-solid interface using a CCD cam of high resolution and specially designed software. The results of the contact angle measurements are presented in figure (9.3.3)

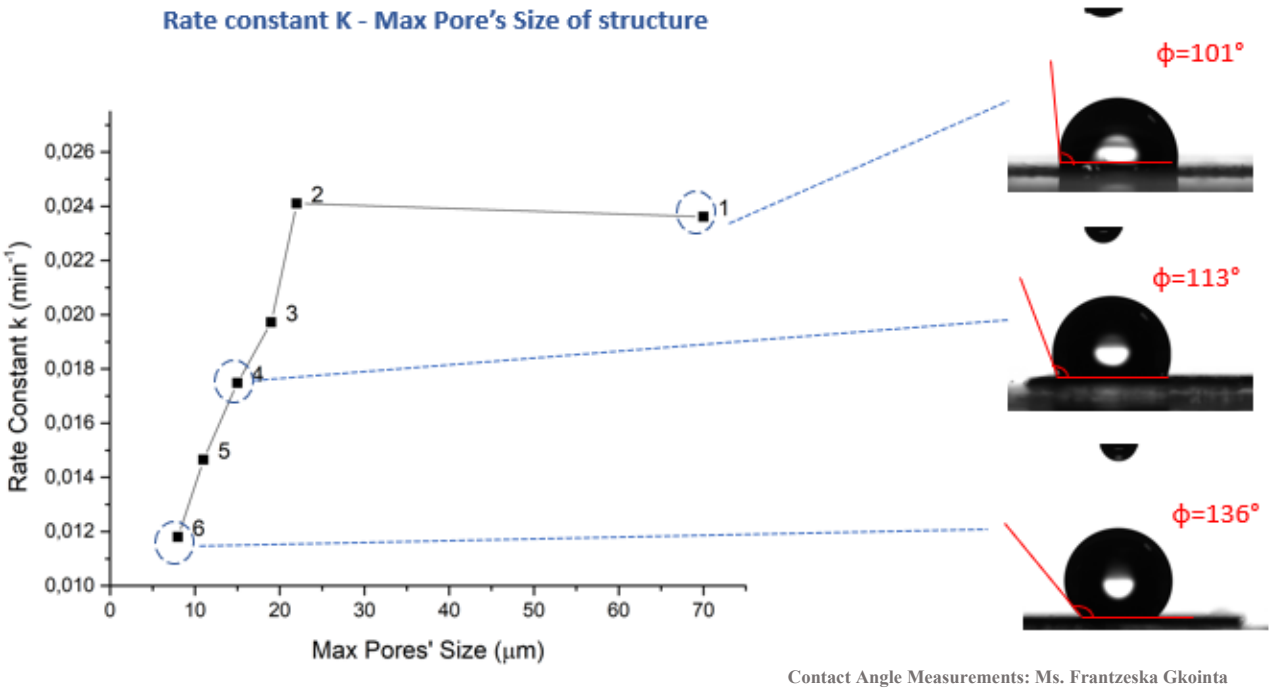


***Figure 9.3.3:*** Contact Angle Measurements Performed In Samples (1), (4), (6) To Determine the Degree Of Wetting

Contact angle values obtained for the distinct porous samples, namely 101°, 113°, and 136°, contribute to the examination of their relative hydrophobic characteristics. The contact angle of 101° (sample 1) suggests a moderately hydrophobic porous surface, with water droplets partially beading up and exhibiting limited spreading within the porous structure. The contact angle of 113° (sample 4), reveals an increase in hydrophobicity compared to the previous sample. Water droplets form more compact beads, indicating enhanced resistance to wetting

within the porous network. Finally, the contact angle of 136° (sample 6) signifies a highly hydrophobic porous surface. Water droplets assume nearly spherical shapes with minimal spreading within the porous structure, demonstrating exceptional surface repellency. The comparison of these contact angle measurements underscores the progressive increase in hydrophobicity as the pore size is reduced. In total, the porous material with a contact angle of 101° exhibits a moderate level of hydrophobicity, while the sample with a contact angle of 113° demonstrates a higher degree of hydrophobicity. The porous material with a contact angle of 136° showcases the highest level of hydrophobicity among the samples, indicating exceptional surface repellency within the porous structure. There results come to an agreement with the measurements obtained in part (9.3.1) and justify the behavior of the samples.

# 10. Future Work

To address the challenge of the hydrophobicity of the samples, a straightforward approach is adopted. We will fabricate larger versions of our three-dimensional nanodevices, which will, then, undergo testing within a properly designed flow platform. The objective is to effectively eliminate the hydrophobic effects and subsequently evaluate the photocatalytic activity of our samples. This methodology will help us overcome the challenges posed by hydrophobicity and gain insights about the performance and efficiency of our catalyst-devices in real-world applications. This approach will allow us to create an environment that encourages efficient interaction between the samples and the surrounding liquid medium, thereby enhancing their performance.

On the other hand, the acceleration of the fabrication process is directly linked with the technical characteristics of the employed setup. So, for example, a stages nano-positioning writing system offers high printing speeds, but limited within a few $10^3$ μm/s scale. However, the implementation of a galvanometric setup could dramatically accelerate the printing process of 3D structures. Hence, there are intentions for the integration of a galvanometric system into the existing setup. The galvanometric system is expected to improve the current system though a more efficient, accurate, and faster printing process. A galvanometric system will enable precise control and manipulation of the laser beam. Thus, enhanced scanning capabilities and increased printing speed is expected, too, allowing time-efficient fabrication.

# 11. Conclusion

In summary, this thesis explored the potential use of a 3D Holographic Printing method as an innovative fabrication technique. It is demonstrated that multi-foci parallel processing offers several significant advantages in comparison with conventional writing techniques, mainly related to the acceleration of the fabrication process, the high spatial resolution of the polymerized structures and the dynamic control of the printing process through laser beam shaping techniques. Moreover, this study has highlighted that the pathway towards realistic applications is now paved by 3D Holographic Printing, since the fabrication of complex structures at the macroscopic regime can be performed within short fabrication time.

This ability to create structures with controlled characteristics (i.e., porosity, specific dimensions) opens up new possibilities in a variety of scientific fields, such as photo-catalysis, meta-surfaces, etc. The experimental results of this research, also, confirm that 3D Holographic Printing is an extremely promising method for the future of fabrication technology, the improvement of sustainable environmental and energy systems and the detection of harmful substances. Finally, 3D Holographic Printing stands as a remarkable and transformative fabrication method that promises to reshape the way we design and create structures.

# References


1. Rekštytė, S., Jonavičius, T. & M. Malinauskas. Direct laser writing of microstructures on optically opaque and reflective surfaces. Optics and Lasers in Engineering, Vol. 53, 2014, pp 90-97. DOI: https://doi.org/10.1016/j.optlaseng.2013.08.017

2. Selimis, A., Mironov, V. & Farsari, M. Direct laser writing: Principles and materials for scaffold 3D printing. Microelectronic Engineering, Vol. 132, 2015, pp 83-89. DOI: https://doi.org/10.1016/j.mee.2014.10.001

3. Nonlinear Lithography Group: Farsari Lab, IESL, FORTH, 2023, Crete, Greece. Retrieved from: https://www.iesl.forth.gr/en/research/NLL_Group#tab-photogallery

4. Sinelnik, A., Samusev, K., Rybin, M. *et al.* Optical properties of 2D photonic structures fabricated by direct laser writing. *SN Appl. Sci.* 1, 1213 (2019). DOI: https://doi.org/10.1007/s42452-019-1220-y

5. Malinauskas, M., Farsari, M., Piskarskas, A. & Juodkazis, S. Ultrafast laser nanostructuring of photopolymers: A decade of advances. Physics Reports, Vol. 533, Issue 1, 2013, pp 1-31. DOI: https://doi.org/10.1016/j.physrep.2013.07.005

6. Skliutas, E., Lebedevaite, M., Kabouraki, E., Baldacchini, T., Ostrauskaite, J., Vamvakaki, M., Farsari, M., Juodkazis, S. & Malinauskas, M. Polymerization mechanisms initiated by spatio-temporally confined light. Nanophotonics, Vol. 10, Issue 4, 2021, pp. 1211-1242. DOI: https://doi.org/10.1515/nanoph-2020-0551

7. Schaffer,C. B. Interaction of Femtosecond Laser Pulses with Transparent Materials (PhD Thesis). Harvard University, Cambridge, Massachusetts, 2021. Retrieved from https://snlab.bme.cornell.edu/uploads/publication/2001SchafferC.pdf

8. Farsari, M., Vamvakaki, M. & Chichkov B.N. Multiphoton polymerization of hybrid materials. J. Opt., Vol.12, Issue 12, 2010. DOI: http://dx.doi.org/10.1088/2040-8978/12/12/124001

9. Lee, K.S., Kim, R.H., Yang, D.Y. & Park, S.H. Advances in 3D nano/microfabrication using two-photon initiated polymerization, Progress in Polymer Science, Vol. 33, Issue 6, 2008, pp 631-681. DOI: https://doi.org/10.1016/j.progpolymsci.2008.01.001

10. Sun, H.B. & Kawata, S. Two-Photon Photopolymerization and 3D Lithographic Microfabrication. In: NMR • 3D Analysis • Photopolymerization. Advances in Polymer Science, Vol 170, 2010. Springer, Berlin, Heidelberg. DOI: https://doi.org/10.1007/b94405

11. Gibson, I., Rosen, D. & Stucker, B. Photopolymerization Processes. In: Additive Manufacturing Technologies. Springer, 2010 Boston, MA. DOI: https://doi.org/10.1007/978-1-4419-1120-9_4

12. Fischer, J. and Wegener, M. Three-dimensional optical laser lithography beyond the diffraction limit. Laser & Photonics Reviews, 7: 22-44, 2013. DOI: https://doi.org/10.1002/lpor.201100046

13. University Of California. Two-Photon fluorescence microscopy. Retrieved From: http://microscopy.berkeley.edu/courses/tlm/2P/index.html.

14. Cicchetti, R., Faraone, A. & Testa, O. Near Field Synthesis Based on Multi-Port Antenna Radiation Matrix Eigenfields. IEEE Access, Vol. 7, pp. 62184-62197, 2019. DOI: 10.1109/ACCESS.2019.2912305

15. Laskin, A., Iaulys, N., Lekys, G. & Laskin, V. Beam shaping unit for micromachining. Proc SPIE, 2013. DOI: 10.1117/12.2025985

16. Christodoulides, D. & Siviloglou, G. Optical Airy bullets and beams. IEEE Photonics Society Summer Topicals 2010, Playa del Carmen, Mexico, 2010, pp. 84-85, DOI: 10.1109/PHOSST.2010.5553670

17. David, L.S. & Fred, M. D. Laser Beam Shaping. Opt. Eng. 42(11), 2003. DOI: https://doi.org/10.1117/1.1624611

18. Mitchell, K. J. Laser beam shaping: properties and applications (PhD thesis). University of Glasgow, 2020. Retrieved from: https://theses.gla.ac.uk/81263/

19. Papazoglou, D.(2013). Phase Control Tutorial.

20. Manousidaki, M. Tailored laser wave packets for advanced micro-structuring of materials (PhD Thesis). Materials Science And Technology Department, University Of Crete, 2019. Retrieved from: http://hdl.handle.net/10442/hedi/46441

21. Harasthy, T., Ovsenik, L. & Turán, J. Current Summary of the Practical Using of Optical Correlators. Acta Electrotechnica et Informatica, 2012. DOI: 12. 10.2478/v10198-012-0042-2.

22. Khare, K.(2016). Fourier Optics and Computational Imaging. John Wiley & Sons Ltd, Vol.14, pp. 193-194. DOI: 10.1002/9781118900352

23. Guzman, C.R. & Forbes, A. How to Shape Light with Spatial Light Modulators. SPIE Press, 2017, Bellingham, Washington. DOI: https://doi.org/10.1117/3.2281295

24. Huignard, J.P. Spatial Light Modulators and Their Applications. J. Optics, Vol. 18, Issue 4, pp. 181-186, 1987. DOI: 10.1088/0150-536X/18/4/003

25. Hamamatsu Photonics K. K. Spatial Light Modulator. Retrieved from https://www.hamamatsu.com/us/en.html

26. Dholakia, K., Čižmár, T. Shaping the future of manipulation. Nature Photon 5, 335–342 (2011). DOI: https://doi.org/10.1038/nphoton.2011.80

27. Poon, T.C. & Liu, J.P.(2014). Introduction To Modern Digital Holography with Matlab. Cambridge University Press, Cambridge, United Kingdom.

28. Wang, W., Ye, F., Shen, H., Moringo, N.A., Dutta, C., Robinson, J.T. & Landes, C.F. Generalized method to design phase masks for 3D super-resolution microscopy. Opt. Express, Vol.27, Issue 3, pp. 3799-3816, 2019. DOI: https://doi.org/10.1364/OE.27.003799

29. Manousidaki, M., Papazoglou, D.G., Farsari, M. & Tzortzakis, S. 3D holographic light shaping for advanced multiphoton polymerization. Opt. Lett. 45, 85-88 (2020). DOI: https://doi.org/10.1364/OL.45.000085

30. Obata, K., Koch, J., Hinze, U. & Chichkov, B.N. Multi-focus two-photon polymerization technique based on individually controlled phase modulation. Opt Express. 2010 Aug 2;18(16):17193-200. DOI: 10.1364/OE.18.017193

31. Villanueva, Y., Liu, D.R. & Cheng, P. Pulsed laser deposition of zinc oxide. Thin Solid Films. 501, 2006, 366–369. DOI: 10.1016/j.tsf.2005.07.152.

32. Shepelin, N.A., Tehrani, Z.P., Ohannessian, N., Schneider, C.W., Pergolesi, D. & Lippert, T. A practical guide to pulsed laser deposition. Chem. Soc. Rev., 2023**,52,** 2294-2321. DOI: https://doi.org/10.1039/D2CS00938B

33. Greer, James. History and current status of commercial pulsed laser deposition equipment. Journal of Physics D Applied Physics. 47, 2013. DOI: 10.1088/0022-3727/47/3/034005

34. Willmott, P. & Huber, J. Pulsed Laser Vaporization and Deposition. Reviews of Modern Physics. 72, 2000. DOI: 10.1103/RevModPhys.72.315

35. Mittra, J., Abraham, G., Kesaria, M., Bahl, S., Singh, R., Shivaprasad, S., Viswanadham, C., Kulkarni, U. & Dey, G. Role of Substrate Temperature in the Pulsed Laser Deposition of Zirconium Oxide Thin Film. Materials Science Forum. 710, 2012, 757-761. DOI: 10.4028/www.scientific.net/MSF.710.757

36. Afonso, C., Gonzalo, J., Serna, R. Solis, J. Pulsed Laser Deposition for Functional Optical Films. 2017. DOI: 10.1007/978-0-387-30453-3_13

37. Saravanan, R., Gracia, F. & Stephen, A. Basic Principles, Mechanism, and Challenges of Photocatalysis. In: Khan, M., Pradhan, D., Sohn, Y. (eds) Nanocomposites for Visible Light-induced Photocatalysis. Springer Series on Polymer and Composite Materials. Springer, Cham, 2017. DOI: https://doi.org/10.1007/978-3-319-62446-4_2

38. Kedruk, Y.Y., Baigarinova, G.A., Gritsenko, L.V., Cicero, G. & Abdullin, K.A. Facile Low-Cost Synthesis of Highly Photocatalitycally Active Zinc Oxide Powders. Front. Mater. 9:869493, 2022. doi: 10.3389/fmats.2022.869493

39. Zhu, S. & Wang, D. Photocatalysis: Basic Principles, Diverse Forms of Implementations and Emerging Scientific Opportunities. Advanced Energy Materials. 7, 2017. DOI: 10.1002/aenm.201700841

40. Nunes, D., Pimentel, A., Santos, L., Barquinha, P., Pereira, L., Fortunato, E. & Martins, R. Structural, optical, and electronic properties of metal oxide nanostructures. 2019. DOI: 10.1016/B978-0-12-811512-1.00003-5

41. Janotti, A., & Van de Walle, C.G. Fundamentals of zinc oxide as a semiconductor. Reports on Progress in Physics, 72, 2019, 126501. DOI: 10.1088/0034-4885/72/12/126501

42. Kumar, R., Umar, A., Kumar, G., Nalwa, H.S., Kumar, A., & Akhtar, M.S. Zinc oxide nanostructure-based dye-sensitized solar cells. Journal of Materials Science. 52. 4743–4795, 2017.DOI: 10.1007/s10853-016-0668-z

43. Cui, T.J., Liu, R. & Smith, D.R. Introduction to Metamaterials. In: Cui, T., Smith, D., Liu, R. (eds) Metamaterials. Springer, Boston, MA, 2010. DOI: https://doi.org/10.1007/978-1-4419-0573-4_1

44. Jiang, W.X. & Cui, T.J. Optical Transformation Theory. In: Cui, T., Smith, D., Liu, R. (eds) Metamaterials. Springer, Boston, MA, 2010. DOI: https://doi.org/10.1007/978-1-4419-0573-4_2

45. Liu, R., Cui, T.J. & Smith, D.R. General Theory on Artificial Metamaterials. In: Cui, T., Smith, D., Liu, R. (eds) Metamaterials. Springer, Boston, MA, 2010. DOI: https://doi.org/10.1007/978-1-4419-0573-4_3

46. Singh, G., Ni, R. & Marwaha, A. A Review of Metamaterials and its Applications. International Journal of Engineering Trends and Technology. 19. 305-310, 2015. DOI: 10.14445/22315381/IJETT-V19P254

47. Liu, Y. & Zhang, X. Metamaterials: a New Frontier of Science and Technology. Chemical Society reviews. 40. 2494-507, 2011. DOI: 10.1039/c0cs00184h

48. Gangwar, K., Paras & Gangwar, R. Metamaterials: Characteristics, Process and Applications. 97-106, 2014. Retrieved from: https://www.researchgate.net/publication/338656389_Metamaterials_Characteristics_Process_and_Applications

49. Tzortzakis, S. (2023). Notes On Photonic Materials: Metamaterials. Retrieved from: https://old.materials.uoc.gr/el/grad/courses/METY490/notes/2013/lecture_10.pdf

50. Chin, J.Y., Liu, R., Cui, T.J. & Smith, D.R. Rapid Design for Metamaterials. In: Cui, T., Smith, D., Liu, R. (eds) Metamaterials. Springer, Boston, MA, 2010. DOI: https://doi.org/10.1007/978-1-4419-0573-4_4

51. Katsantonis, I., Manousidaki, M., Koulouklidis, A. D., Daskalaki, C., Spanos, I., Kerantzopoulos, C., Tasolamprou, A. C., Soukoulis, C. M., Economou, E. N., Tzortzakis, S., Farsari, M. & Kafesaki, M. Strong and Broadband Pure Optical Activity in 3D Printed THz Chiral Metamaterials. Adv. Optical Mater. 2023, 2300238. DOI: https://doi.org/10.1002/adom.202300238

52. Kyriakakis, A. Accelerating laser photopolymerization through beam shaping (BSc Thesis). Materials Science And Technology Department, University Of Crete, 2021. Retrieved from: https://elocus.lib.uoc.gr/dlib/c/3/d/metadata-dlib-1642071035-52780-574.tkl

53. Konstantinos, M. High-resolution and large volume 3D porous media through beam interference nonlinear laser additive manufacturing with applications in photocatalysis (BSc Thesis). Materials Science And Technology Department, University Of Crete, 2022.

54. Giakoumaki, A.N., Kenanakis, G., Klini, A. et al. 3D micro-structured arrays of ZnO nanorods. Sci Rep 7, 2100, 2017. DOI: https://doi.org/10.1038/s41598-017-02231-z

55. Klini, A., Manousaki, A., Anglos, D. & Fotakis, C. Growth of ZnO Thin Films by Ultraviolet Pulsed-Laser Ablation: Study of Plume Dynamics. Journal of Applied Physics. 98, 123301-123301,2005. DOI: 10.1063/1.2149498

56. Konstantaki, M., Klini, A., Anglos, D. & Pissadakis, S. An ethanol vapor detection probe based on a ZnO nanorod coated optical fiber long period grating. Opt. Express 20, 8472-8484, 2012. DOI: https://doi.org/10.1364/OE.20.008472

57. Frysali, M. A., Papoutsakis, L., Kenanakis, G., & Anastasiadis, S. H. Functional Surfaces with Photocatalytic Behavior and Reversible Wettability: ZnO Coating on Silicon Spikes. The Journal of Physical Chemistry C, 119 (45), 25401–25407, 2015. DOI:10.1021/acs.jpcc.5b07736

58. Kenanakis, G., & Katsarakis, N. ZnO nanowires on glass via chemical routes: A prospective photocatalyst for indoors applications. Journal of Environmental Chemical Engineering, 2(3), 1416–1422, 2014. DOI:10.1016/j.jece.2014.06.016 10.1016/j.jece.2014.06.016

59. Khan, I., Saeed, K., Zekker, I., Zhang, B., Hendi, A.H., Ahmad, A., Ahmad, S., Zada, N., Ahmad, H., Shah, L.A., et al. Review on Methylene Blue: Its Properties, Uses, Toxicity and Photodegradation. Water. 2022; 14(2):242. DOI: https://doi.org/10.3390/w14020242

60. Sabouni, R. & Gomaa, H. Photocatalytic degradation of pharmaceutical micro-pollutants using ZnO. Environ. Sci. Pollut. Res., vol. 26, no. 6, pp. 5372–5380, 2019. DOI: 10.1007/s11356-018- 4051-2

61. Gojda, F., Loulakis, M., Papoutsakis, L., Tzortzakis, S., Chrissopoulou, K. & Anastasiadis, S. Altering the Surface Properties of Metal Alloys Utilizing Facile and Ecological Methods. Langmuir. 38, 2022. DOI: 10.1021/acs.langmuir.1c03431.